

AFWAL-TR-83-4038

HIGH STRAIN RATE CHARACTERIZATION OF MATERIALS

S. J. Bless  
A. M. Rajendran  
D. Dawicke  
D. L. Paisley

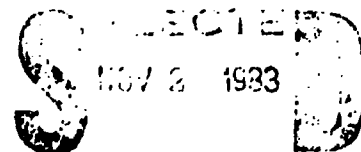
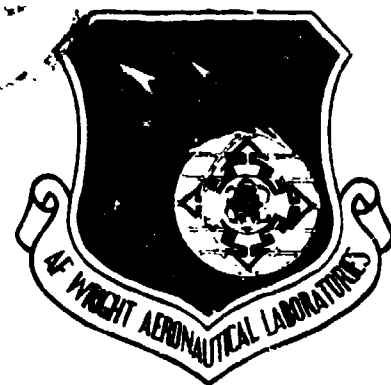
University of Dayton Research Institute  
300 College Park Avenue  
Dayton, Ohio 45469

August 1983

Final report for March 1981 - December 1982

Approved for public release; distribution unlimited.

MATERIALS LABORATORY  
AIR FORCE WRIGHT AERONAUTICAL LABORATORIES  
AIR FORCE SYSTEMS COMMAND  
WRIGHT-PATTERSON AIR FORCE BASE, OHIO 45433



D

83 11 01 009

DTIC FILE COPY

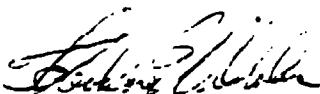
AD-A134341

## NOTICE

When Government drawings, specifications, or other data are used for any purpose other than in connection with a definitely related Government procurement operation, the United States Government thereby incurs no responsibility nor any obligation whatsoever; and the fact that the government may have formulated, furnished, or in any way supplied the said drawings, specifications, or other data, is not to be regarded by implication or otherwise as in any manner licensing the holder or any other person or corporation, or conveying any rights or permission to manufacture, use, or sell any patented invention that may in any way be related thereto.

This report has been reviewed by the Office of Public Affairs (ASD/PA) and is releasable to the National Technical Information Service (NTIS). At NTIS, it will be available to the general public, including foreign nations.

This technical report has been reviewed and is approved for publications.

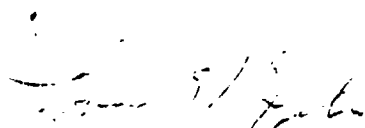


THEODORE NICHOLAS  
Project Engineer



JOHN P. HENDERSON, Chief  
Metals Behavior Branch

FOR THE COMMANDER



LAWRENCE N. HJELM, Asst Chief  
Metals and Ceramics Division

"If your address has changed, if you wish to be removed from our mailing list, or if the addressee is no longer employed by your organization please notify AFWAL/MLLN, Wright-Patterson Air Force Base, Ohio 45433 to help us maintain a current mailing list".

Copies of this report should not be returned unless return is required by security considerations, contractual obligations, or notice on a specific document.

UNCLASSIFIED

SECURITY CLASSIFICATION OF THIS PAGE (When Data Entered)

REPORT DOCUMENTATION PAGE		READ INSTRUCTIONS BEFORE COMPLETING FORM
1. REPORT NUMBER AFWAL-TR-83-4038	2. GOVT ACCESSION NO. AD-A134342	3. RECIPIENT'S CATALOG NUMBER
4. TITLE (and Subtitle) HIGH STRAIN RATE CHARACTERIZATION OF MATERIALS		5. TYPE OF REPORT & PERIOD COVERED Final March '81 - December '82
7. AUTHOR(s) S. J. Bless, A. M. Rajendran, D. Dawicke, D. L. Paisley		6. PERFORMING ORG. REPORT NUMBER UDR-TR-83-11
9. PERFORMING ORGANIZATION NAME AND ADDRESS University of Dayton Research Institute 300 College Park Ave. Dayton, Ohio 45469		8. CONTRACT OR GRANT NUMBER(s) F33615-81-K-5082
11. CONTROLLING OFFICE NAME AND ADDRESS Materials Laboratory (AFWAL/MLLN) Air Force Wright Aeronautical Laboratories Wright-Patterson AFB, OH 45433		10. PROGRAM ELEMENT, PROJECT, TASK AREA & WORK UNIT NUMBERS 2422-05-02
14. MONITORING AGENCY NAME & ADDRESS (if different from Controlling Office)		12. REPORT DATE August 1983
		13. NUMBER OF PAGES 103
		15. SECURITY CLASS. (of this report) Unclassified
		16. DECLASSIFICATION/DOWNGRADING SCHEDULE
18. DISTRIBUTION STATEMENT (of this Report)  Approved for public release; distribution unlimited.		
17. DISTRIBUTION STATEMENT (of the abstract entered in Block 20, if different from Report)		
19. SUPPLEMENTARY NOTES		
19. KEY WORDS (Continue on reverse side if necessary and identify by block number)  Impact damage, spall, strength, Hopkinson bar, copper, steel, expanding ring, Bridgeman correction		
20. ABSTRACT (Continue on reverse side if necessary and identify by block number)  New techniques have been developed to study dynamic tensile failure of ductile metals: expanding rings, and necked Hopkinson bar samples. Flat plate (spall) experiments have also been carried out. Results are presented for OFHC copper and some other metals.		

DD FORM 1 JAN 73 1473

EDITION OF 1 NOV 65 IS OBSOLETE

UNCLASSIFIED

SECURITY CLASSIFICATION OF THIS PAGE (When Data Entered)

# PREFACE

The work reported in this report was conducted under Contract No. F33615-81-K-5082 for AFWAL/MLLN. The Contract Monitor was Dr. Theodore Nicholas. His many helpful comments during the execution of the program were greatly appreciated. Dr. Stephan Bless was the Principal Investigator for the University. Dr. A. M. Rajendran assisted with the theoretical analysis of the behavior of the Hopkinson bar experiments. Mr. Dave Dawicke conducted the Hopkinson bar experiments. Mr. Dennis Paisely conducted the spall experiments. The experimental facilities were located in the Impact Physics Laboratory at the University of Dayton.

Accession For	
NTIS GRA&I	<input checked="" type="checkbox"/>
DTIC TAB	<input type="checkbox"/>
Unannounced	<input type="checkbox"/>
Justification	
By	
Distribution/	
Availability Codes	
Dist	Avail and/or Special
A/1	



## TABLE OF CONTENTS

<u>SECTION</u>	<u>PAGE</u>
I INTRODUCTION	1
II PLATE IMPACT EXPERIMENTS	2
1. EXPERIMENTAL TECHNIQUES	2
a. Compressed Gas Gun	2
b. Target Mounting	4
c. Tilt Check	4
d. Instrumentation	5
2. TEST PARAMETERS	7
3. RESULTS FOR OFHC COPPER	11
a. Description of Damage	11
b. Spall Threshold Data	14
c. Free Surface Velocities	18
4. RESULTS FOR MILD STEEL	30
5. RESULTS FOR 1100 ALUMINUM	30
6. SWAP SIMULATIONS	33
III TENSILE TESTS WITH A HOPKINSON BAR	37
1. HOPKINSON BAR APPARATUS	37
2. DIAGNOSTIC TESTS OF HOPKINSON BAR	40
a. Signal Recording	40
b. Stress Validation	45
3. NECKING	45
a. Non-uniform Tensile Specimens	48
b. Finite Element Analysis of a Necked Specimen	49
c. Experimental Investigation of Necking	59
4. TEST ON WAAM COPPER LINES	67
5. RESULTS OF HOPKINSON BAR TESTS FOR OTHER MATERIALS	78
a. 1020 Mild Steel	78
b. OFHC Copper	78
IV EXPERIMENTS WITH DYNAMICALLY EXPANDED THIN RINGS	81
1. EXPERIMENTAL TECHNIQUE	81

Table of Contents (Continued)

<u>SECTION</u>	<u>PAGE</u>
2. EXPERIMENTAL RESULTS	84
3. SUMMARY	89
REFERENCES	91
LIST OF SYMBOLS	93

# LIST OF FIGURES

<u>FIGURE</u>		<u>PAGE</u>
1	Performance of 50 mm Compressed Gas Gun.	3
2	Photograph of Target and Mount for High Temperature Impact.	3
3	VISAR Configuration Used in Spall Experiments.	6
4	(x,t) Diagram for a Spall Test.	8
5	Flyer Plate Designs	9
6	Comparison of Polishing Techniques, Shot 70541 (a) Electrolytic, (b) Mechanical.	12
7	Comparison of Polishing Techniques, Shot 7-537, (a) Electrolytic, (b) Mechanical.	13
8	Spall Data for Room Temperature OFHC Copper.	15
9	Spall Data for OFHC Copper at Elevated Temperature.	16
10	Effect of Temperature on Spall Damage in OFHC Copper (a) 20°C ( $u_o = 95$ m/s, Shot 545), (b) 425°C ( $u_o = 102$ m/s, Shot 541).	17
11	Apparent Void Size Distribution from Section in Figure 10. (a) 20°C, (b) 425°C.	18
12	General Form of Free Surface Velocity History for Spalled Target.	19
13	VISAR Data for Shot #7-536.	22
14	VISAR Data for Shot #7-537.	23
15	VISAR Data for Shot #7-538.	24
16	VISAR Data for Shot #7-540.	25
17	VISAR Data for Shot #7-542.	26
18	VISAR Data for Shot #7-543.	26
19	VISAR Data for Shot #7-545.	27
20	VISAR Data for Shot #7-552.	28

# List of Figures (Continued)

<u>FIGURE</u>		<u>PAGE</u>
21	VISAR Data for Shot #7-560.	29
22	Spall Threshold Data for 1020 Steel.	31
23	VISAR Data from Shot 555.	31
24	SWAP Elastic-plastic Calculation for Shot No. 540, (x,t) Diagram.	34
25	SWAP Elastic-plastic Calculation of VISAR Data for Shot No. 540.	34
26	SWAP Calculation with Continuous Unloading Model, (x,t) Diagram.	35
27	Stress History of Spall Plane for Calculation Depicted in Figures 24 and 25.	36
28	Tuler-Butcher Prediction of Spall Thresholds for $K = 19 \text{ kbar}^2 - \mu\text{s}$ .	36
29	Hopkinson Bar Specimen Design.	38
30	Response of the SRL Amplifiers to a 10 kHz Square Wave Signal.	42
31	Response of the 1A7A Tektronix Amplifier to a 10 kHz Square Wave with a 1 MHz Filter Setting.	43
32	Response of the 1A7A Tektronix Amplifier to a 10 kHz Square Wave with a 100 kHz Filter Setting.	44
33	Separate Traces of Hopkinson Bar Strain Gages on the First Bar.	44
34	Results of Three Tests on 6061-T6 Aluminum at $500 \text{ s}^{-1}$ , $350 \text{ s}^{-1}$ , and $200 \text{ s}^{-1}$ .	46
35	Comparison of the Hopkinson Bar Analysis of 6061-T6 at Three Different Strain Rates to the Static Results of the Same Material.	47
36	Axi-symmetric Notched Tensile Specimen.	50
37	Velocity - Time Input Condition.	52



# List of Figures (Continued)

<u>FIGURE</u>		<u>PAGE</u>
38	Coarse Mesh Pattern for the Notched Tensile Specimen.	52
39	Variation of Axial Stress Along the Radius of Notch Minimum Cross Section for Initial Time Steps.	54
40	Variation of Effective Plastic Strain Along Minimum Cross Section at Various Time Steps.	54
41	Improved Finite Element Mesh.	56
42	Results Obtained with Mesh Shown in Figure 41 for Minimum Cross Section (a) $\sigma_m$ (b) Plastic Strain.	57
43	Comparison of MAGNA Prediction (dotted line) and Bridgeman Analysis (solid line) for Minimum Cross Section at 10.5 $\mu s$ .	58
44	OFHC Copper Specimen Just Prior to Rupture.	60
45	1020 Steel Specimen Just Prior to Rupture.	60
46	Comparison of Strains Computed from SHB Gauges (line) and Photographs (Points) for 1020 Steel Specimen.	62
47	Comparison of Strains Computed from SHB Gauges (Line) and Photographs (Points) for OFHC Copper Specimen.	62
48	Engineering Stress vs. Strain, OFHC Copper, Tests (a) 16 and (b) 18.	63
49	Variation of Diameter with Frame Number (Each Frame is 20 ns).	63
50	Variation of Radius of Curvature with Frame Number.	65
51	Effective Stress vs. Strain for Necked OFHC Copper Specimens.	65
52	Variation with Time of Bridgeman Factor, B, in Tests 16, 17, and 18.	66

# List of Figures (Continued)

<u>FIGURE</u>		<u>PAGE</u>
53	Comparison of Compression (1) and Tension (2) Stress Strain Curves for Hard Materials (a) 6061-T6 Aluminum, (b) Half Hard OFHC Copper.	68
54	Engineering Stress-Strain Behavior of Fully Annealed OFHC Copper, (1) Compression (2) Tension.	69
55	Stress-Strain Curves from Hopkinson Bar Analysis of Room Temperature Tests of the ORBITAL FORGED WAAM Warhead Liner.	70
56	Stress-Strain Curves from Hopkinson Bar Analysis of Room Temperature Tests of the F7A WAAM Warhead Liner.	71
57	Stress-Strain Curves from Hopkinson Bar Analysis of Room Temperature Tests of the C22 WAAM Warhead Liner.	72
58	Stress-Strain Curves from Hopkinson Bar Analysis of Room Temperature Tests of the F15 WAAM Warhead Liner.	73
59	Stress-Strain Curves from Hopkinson Bar Analysis of Room Temperature Tests of the C3A WAAM Warhead Liner.	74
60	Stress-Strain Curves from Hopkinson Bar Analysis of Room Temperature Tests of the M13A WAAM Warhead Liner.	75
61	Stress-Strain Curves from Hopkinson Bar Analysis of Room Temperature Tests of the M36 WAAM Warhead Liner.	76
62	Stress-Strain Curves for Unannealed and (a) annealed (b) WAAM Liner Materials.	79
63	True Stress-True Strain Measurement for 1020 Steel Specimen.	80
64	Smoothed Engineering Stress-Strain Behavior for 1020 Steel at Various Strain Rates.	81
65	Sample Streak Record from Expanding Rings Launched by Polyethylene Cylinders (a) 1100 Aluminum, (b) OFHC Copper.	83

## List of Figures (Continued)

<u>FIGURE</u>		<u>PAGE</u>
66	Effect of Tupture of Polyethylene Driver on Ring Expansion (a) Driver Intact, (b) Driver Rupture.	85
67	Velocity History for Copper Ring Launched by 47 mm Diameter Polyethylene Driver Cylinder.	86
68	Yield Stress Data for Copper from Various Tests.	88
69	Comparison of Midrange Expanding Ring Data with SHB Data; OFHC Copper.	88

## LIST OF TABLES

<u>TABLE</u>		<u>PAGE</u>
I	TEST SHOT MATRIX FOR OFHC COPPER, 1020 STEEL, AND 1100 ALUMINUM	10
II	DATA FOR COPPER	21
III	DATA FOR 1020 STEEL	32
IV	SPALL OBSERVATIONS IN 1100 ALUMINUM (Present Data Plus Data from Reference 2)	32
V	SUMMARY OF 6061-T6 TENSION AND COMPRESSION TESTS	77
VI	SUMMARY OF ROOM TEMPERATURE WAAM WARHEAD LINER COMPRESSION TESTS	77

## SECTION I

### INTRODUCTION

The behavior of materials under dynamic tensile loads continues to be an area of active research. Improved descriptions of flow and fracture are needed for numerical simulation of impact-induced tensile fracture, penetration of projectiles, and explosive forming.

In this report, new test techniques and new data are reported. Extensive flow stress and fracture data are included for OFHC copper. Limited data are also presented for mild steel, 1100 aluminum, and 3003 aluminum.

This report is a sequel to Reference 1. The principal results of Reference 1 are repeated herein, but the narrative is focused on work completed since Reference 1 was prepared.

## SECTION II

### PLATE IMPACT EXPERIMENTS

#### 1. EXPERIMENTAL TECHNIQUES

The range techniques have been modified in some important ways from those used in previous work. An improved launch technique and a heated target holder have been developed and placed in use. VISAR modifications, an electronic fiducial, and shot set-up techniques have improved the quality of data recorded.

##### a. Compressed Gas Gun

Previous work had been conducted with a 40 mm bore propellant gun. This system had turned out to have some drawbacks for determination of spall thresholds for weak materials. It could not be fired with better than 50 percent reproducibility for launch velocities below 200 m/s. Additionally, the 36 mm flyer diameter limited impact tilt precision and restricted duration of plane stress conditions in the targets.

Substitution of a 50 mm compressed gas gun has alleviated these problems. The flyer plate diameter was increased to 44 mm. The gas gun is 4.9 m long and 133 mm outside diameter. Its large air reservoir can be pressurized to 300 psi with air or helium. The gun is discharged with a fast acting butterfly valve.

Two position detectors are placed in the barrel near the muzzle and separated by 100.0 mm. The detectors consist of wire pins that protude into the bore a few millimeters, and which are insulated from the bore wall. The pins are grounded by an aluminum ring on the nose of the projectile. The performance of the gun is presented in Figure 1. A 0.08 mm Mylar diaphragm is used at pressures above 40 psi. When the total pressure exceeds 100 psi, the pressurization is done with helium.

Polycarbonate sabots are used with the air gun. The design is considerably less elaborate than that used previously, however

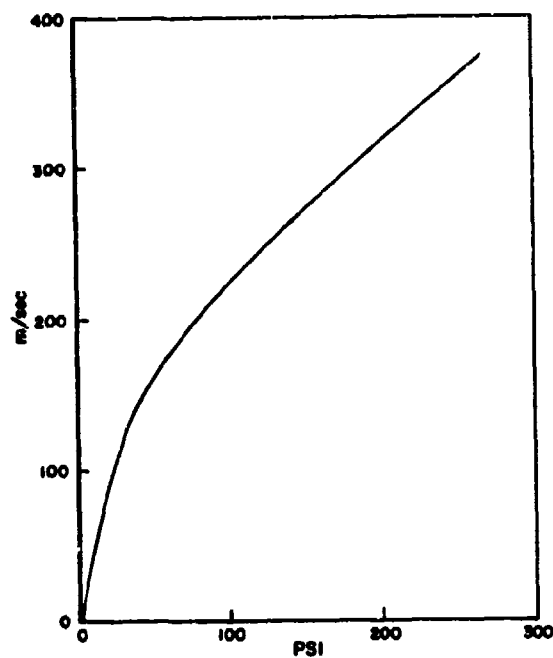


Figure 1. Performance of 50 mm Compressed Gas Gun.

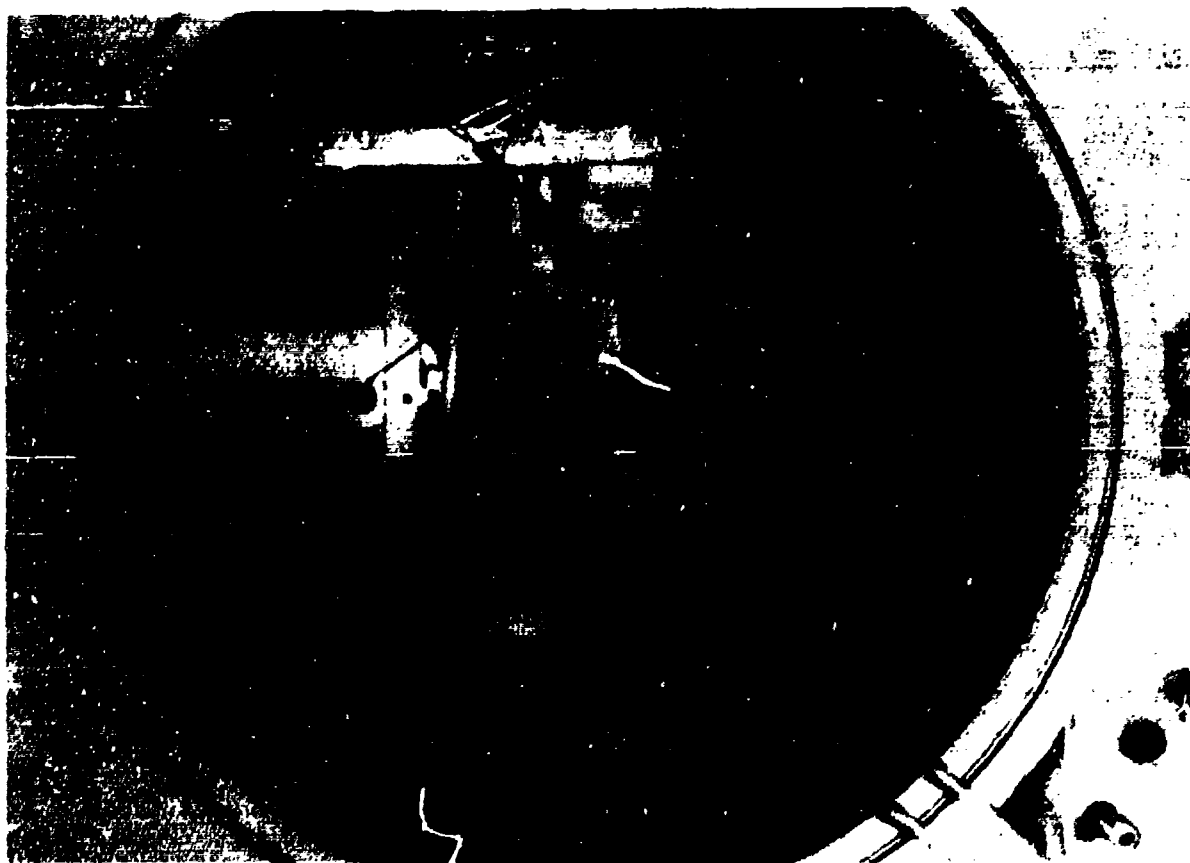


Figure 2. Photograph of Target and Mount for High Temperature Impact.

the launch is relatively benign. The body of the sabot is turned from a single rod of stock. The flyer plate diameters are 43 mm. The flyer plates are bonded in place using epoxy. A special fixture is used to ensure planarity. The launch mass, with a 2 mm steel flyer, is 178 g.

b. Target Mounting

The target fixturing has been modified so that targets may be heated prior to impact. Mechanisms and feedthroughs have been devised to allow a flat resistance heater to be quickly applied and withdrawn without opening the blast tank. Figure 2 illustrates this arrangement.

The resistance heater covers the rear surface of the target and consumes 240 watts. The target is heated in an inert atmosphere to eliminate oxidation of the target. Forty-five minutes are required to reach 425 to 450°C. During the heating process, the heater is raised periodically in order to check the VISAR fringe quality. Heated surfaces are less reflective, so a collector lens for the VISAR was placed inside the blast tank and to one side of the turning mirror. The lens has not been damaged but does require cleaning after each shot.

The target mount was modified to thermally insulate the target from the aluminum housing. An insulating ring separates them. The contact pins used for time of arrival measurements and VISAR triggering were fitted with ceramic sleeves and cemented in place with a high temperature adhesive.

c. Tilt Check

At the low velocities accessible with the newly installed 50 mm air gun, shock front tilt is more sensitive to impact tilt. The shock front tilt,  $\theta$ , is given by:

$$\theta = \tan^{-1} (C/u_0 \tan \phi) \quad (1)$$

or



$$\Delta t = W \tan \theta / C$$

(2)

$$\Delta t = D \tan \theta / u_0$$

where  $\phi$  is the impact tilt,  $C$ , is the shock speed;  $u_0$  is the impact velocity,  $W$  is the flyer diameter, and  $\Delta t$  is the tilt measured in units of time. It was desired to keep  $\tan \theta < 0.1$ . Hence,  $\Delta t < 0.36$  microseconds. At 100 m/s this implies  $\phi < 0.8$  milliradians for a 40 mm diameter flyer plate.

Measurements were made on flyer plates assembled in sabots by the standard technique. It was found that flyer plates may be tilted in the sabot during assembly resulting in non-planar impacts with the target by as much as  $\pm 0.25$  mm at the circumference of the projectile. This condition would result in an impact angle up to 11.6 milliradians for a 44 mm diameter projectile. Therefore, a new fixture was constructed to reduce assembly tilt to tolerable levels.

Tests were conducted to perform measurements to confirm our ability to control these parameters for future impact testing. These tests were performed by measuring the perpendicularity of the flyer plate to the outside diameter of the sabot and aligning the target perpendicular to the axis of the launch tube bore. Two flush mounted timing pins in the target were used to record the arrival of the flyer plate. The velocity of the flyer plate and the timing differences between pins were recorded. The results indicated that impact angle could be maintained at 1.0 milliradian.

#### d. Instrumentation

VISAR target lenses and accessory optics have been modified and up-graded to improve the optical intensity of the quadrature data signals by a factor of five times. The current experimental optical set-up for recording VISAR data is shown in Figure 3.

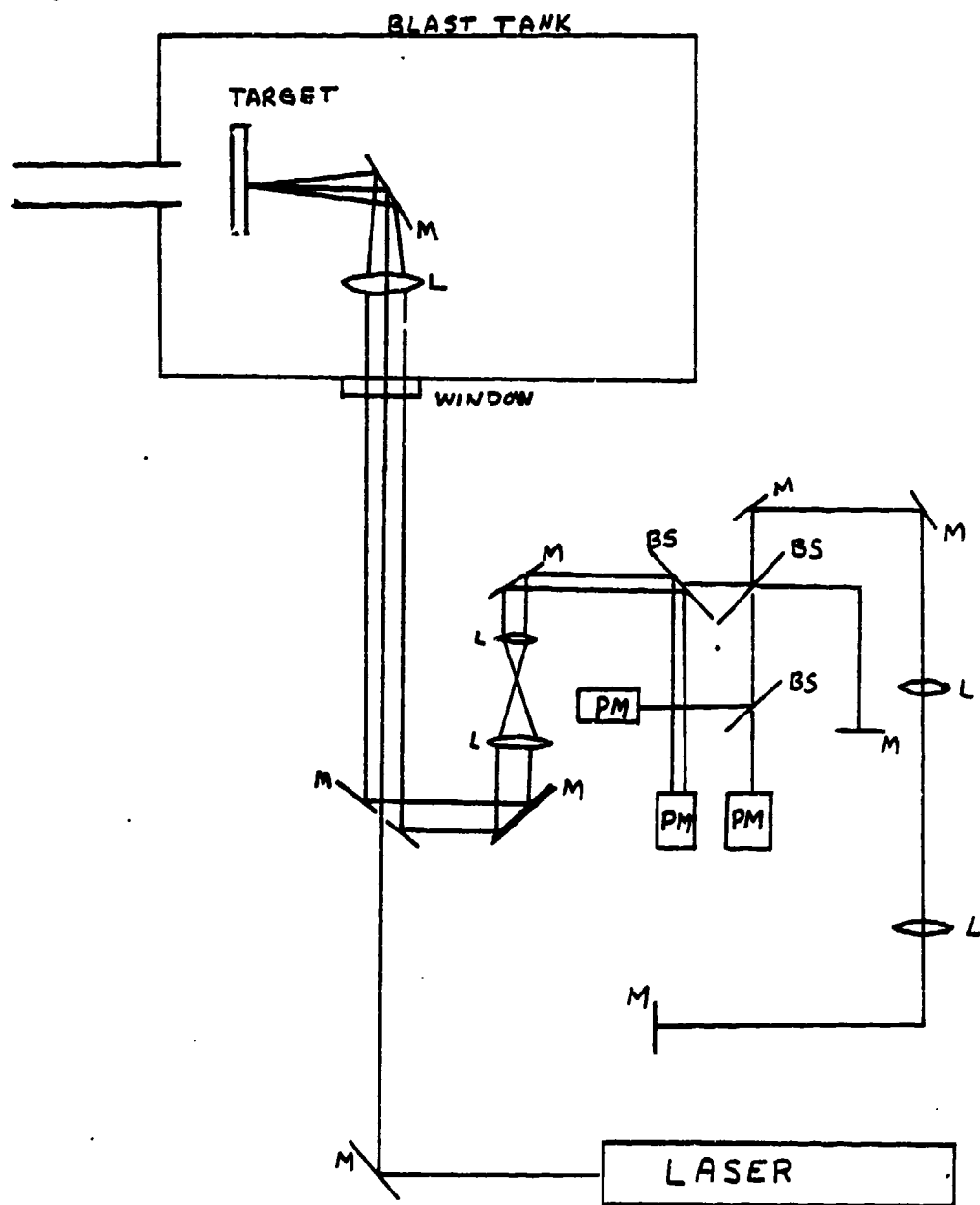


Figure 3. VISAR configuration used in spall experiments.

An electronic fiducial was added to the VISAR control unit to provide better time correlation of data channels. The ancillary instrumentation and blast tank configuration have not been changed significantly.

## 2. TEST PARAMETERS

The spall tests had two objectives: (1) determination of the threshold conditions associated with onset of spall fracture and (2) free surface velocity history associated with spall fracture.

Threshold conditions were mapped by varying the impact velocity and flyer plate thickness. The standard test configuration employed flat flyer plates (of thickness  $d$ ) striking flat targets (of thickness  $D$ ). Figure 4 is an  $(x,t)$  diagram of such an impact, showing how tensile stresses can be developed in the target. The tensile stress amplitude depends upon the striking velocity, and is essentially equal to the peak compressive stress. The duration of the tensile pulse is approximately proportional to the flyer plate thickness, except when  $d/D < 0.2$ .

In order to reduce the total number of shots required stepped flyer plates were used in many tests. There was one step, along a diameter, so two different flyer thicknesses were tested at once. Wedge shaped flyer plates were also used for some shots. These flyer plates were very helpful for determining spall thresholds in regions where stress duration effects overshadow stress amplitude effects. Altogether, six flyer plate designs were used for testing (Figure 5). The wedge flyer plates were backed with mating teflon wedges, and then cemented into Lexan projectiles. All other flyer plates were backed with Lexan, except in Shots 560, 561, and 562, in which the flyer plates were airbacked. The targets were all 76 mm diameter disks of either 2, 4, 5, 5.5, or 9 mm thickness. The test parameters are given in Table I.

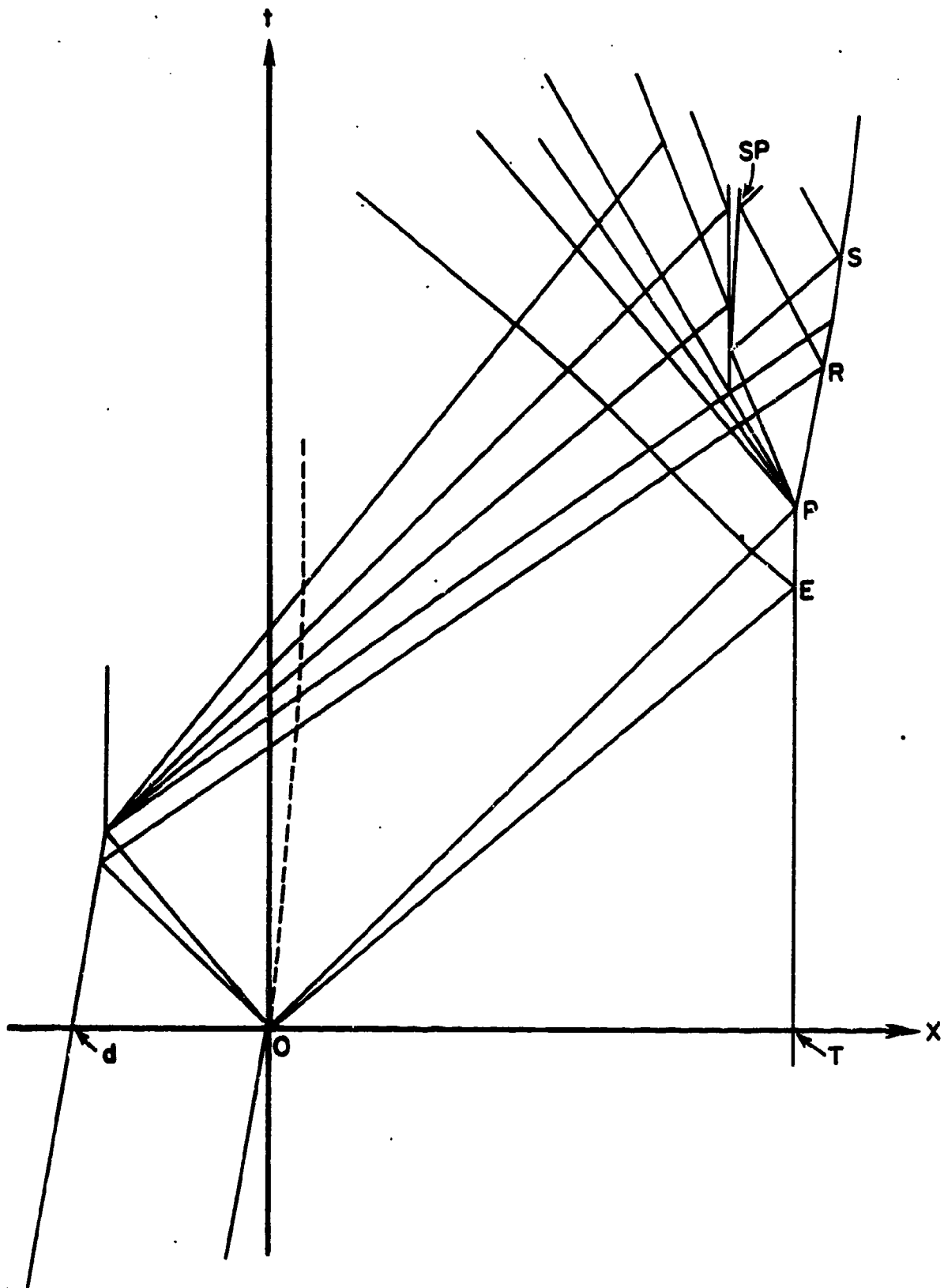


Figure 4.  $(x,t)$  Diagram for a Spall Test. (Spall Occurs at SP.)



(a) FLAT



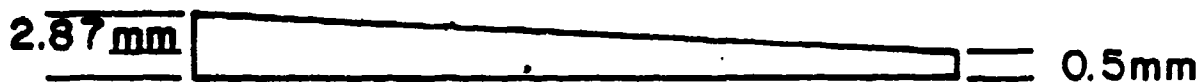
(b) STEPPED



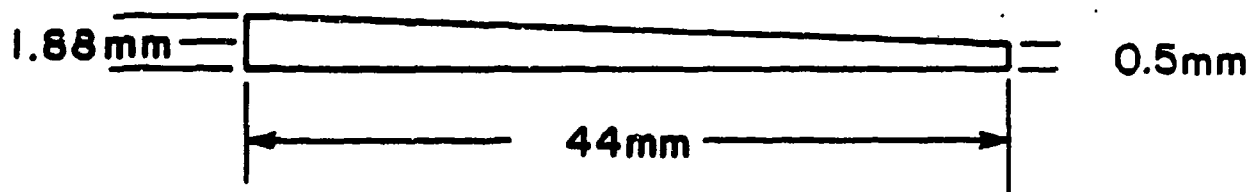
(c) THIN TAPER



(d) 5.7° TAPER



(e) 3° TAPER



(f) 1.8° TAPER

Figure 5. Flyer Plate Designs.

**TABLE 1**  
**TEST SHOT MATRIX FOR OFHC COPPER,**  
**1020 STEEL, AND 1100 ALUMINUM**

Test Material	Target Geometries	Projectile Geometries	Velocity Range M/S	Impact Temperature °C
Annealed OFHC Copper	4, 5, 5.5, and 9 mm Thick	0-4.9 mm Thick	60-200	Ambient and 425
1020 Steel	4 mm Thick	0.5 and 2 mm Thick	130 - 440	Ambient and 425
1100 Aluminum	2 mm Thick	0-1 mm Thick	402	Ambient

### 3. RESULTS FOR OFHC COPPER

The material used in these tests was annealed OFHC copper. The anneal cycle was two hours at 540°C, then cooled at approximately 100°C per hour. The hardness of the copper was Rockwell R42.

#### a. Description of damage

After impact testing, all target specimens were metallographically cross sectioned to determine the degree of damage and the distance between the damaged region and the rear surface of the target. The sections were taken along the diameter of the targets. Targets that were impacted by wedge flyer plates were cross sectioned along a diameter colinear with the wedge angle of the flyer plate.

Two standard metallographic polishing techniques were evaluated, viz. mechanical polishing and electrolytic polishing. Numerous targets were polished by both methods and compared microscopically. The results show that for the annealed OFHC copper, the electrolytic polishing exposed damage in the tensile stressed areas whereas the mechanical polish tended to "smear" material over cracks and voids, concealing damage that may have occurred. Figures 6 and 7 are typical of the observable difference in specimens prepared by each technique.

The criteria used to characterize the degree of damage is the same as previously reported, i.e., 50 to 100 percent void area along the spall plane is considered a "spall". Detectable voids at less than 50 percent areal fracture is termed "partial spall". Damage assessments do not include regions of the targets effected by edge-generated release waves.

Observed damage in partially spalled targets is generally consistent with conventional void nucleation and growth concepts. There is a range of void sizes present, with many more small ones than large ones.

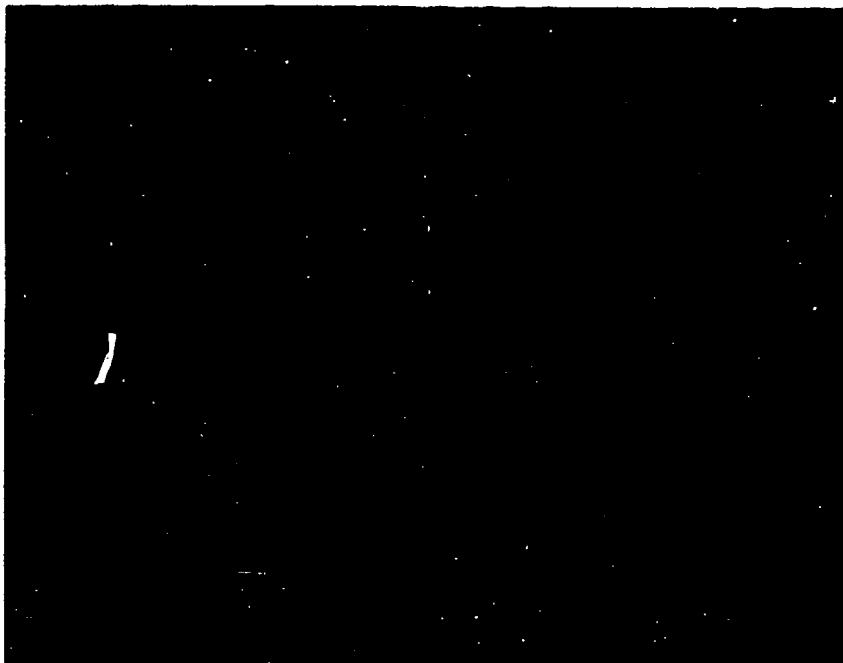
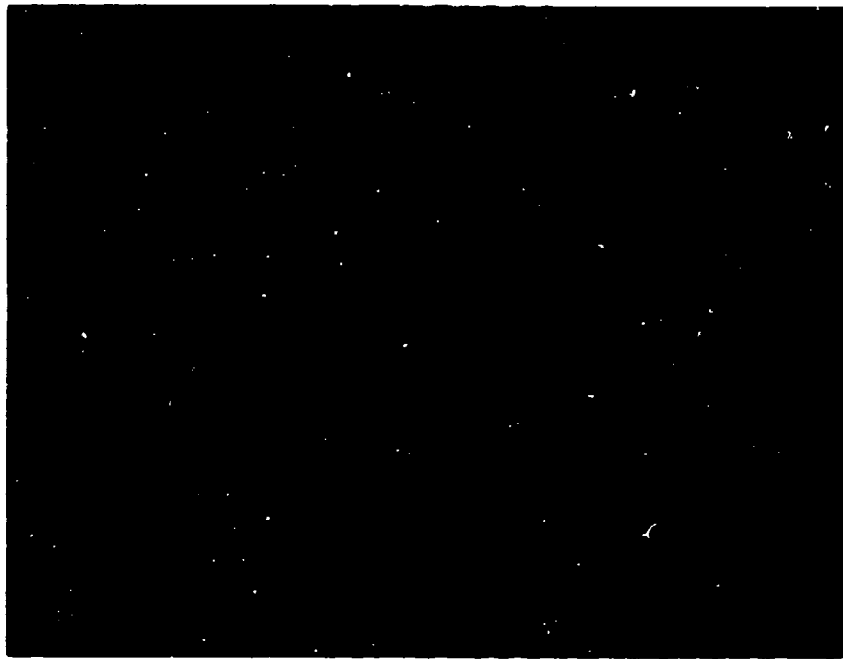


**Figure 6.** Comparison of Polishing Techniques, Shot 7-541  
(a) Electrolytic, (b) Mechanical.





a



b

Figure 7. Comparison of Polishing Techniques, Shot 7-537,  
(a) Electrolytic, (b) Mechanical.

b. Spall Threshold Data

Impact tests were carried out on OFHC copper at ambient temperature (nom. 20°C) and elevated temperature (nom. 425°C). The test matrix and summary of results are presented in Table II. Details are discussed below.

i. Ambient-Temperature Copper. The test matrix was designed to supplement the data reported in References 1 and 2 for ambient-temperature OFHC copper. Emphasis was placed on both definition of the spall threshold for short duration tensile pulses and improved diagnostics of the development of spall formation for stress conditions well above threshold values.

Tests with six wedged and four plane flyer plates were performed (Table I). The measured location of the spall planes closely agreed with the theoretical location of the damage plane in both the wedge and plane flyer plates, viz. at D-d away from the impact surface.

Figure 8 shows the new data and that generated previously<sup>(1,2)</sup> for annealed OFHC copper. The data form a consistent picture of threshold conditions for partial and complete spall. Figure 8 also indicates the peak tensile stress, estimated as equal to the peak compressive stress computed from the standard Hugoniot<sup>(2)</sup>. The duration of the tensile pulse is given approximately by:

$$t_t = 2d/c_0 \quad (3)$$

ii. Spall at Elevated Temperature. Six OFHC copper spall tests were performed with the targets heated to  $425 \pm 25^\circ\text{C}$ . (This is approximately 40 percent of the melting temperature.) The elevated temperature data are summarized in Figure 9.

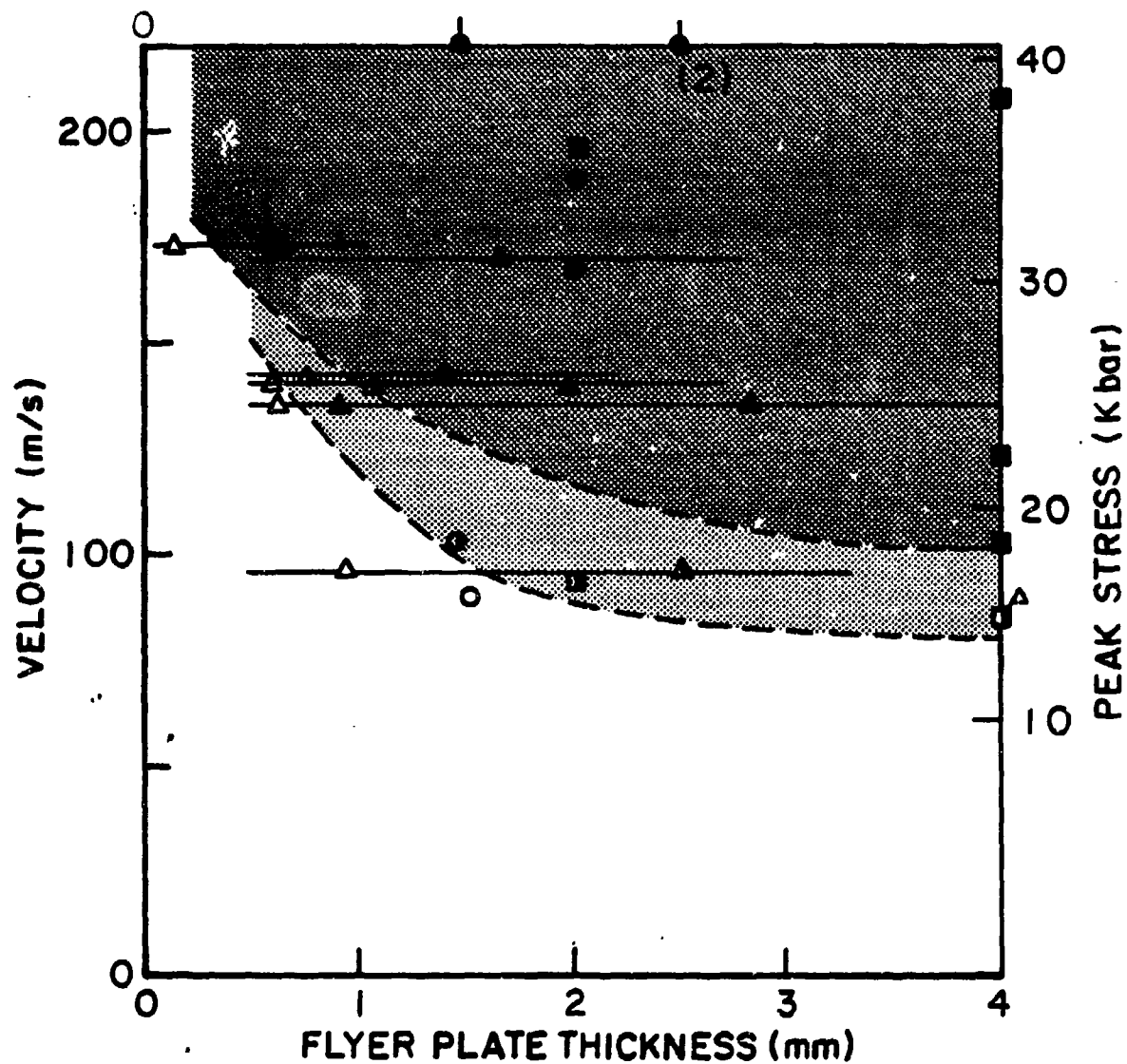


Figure 8. Spall Data for Room Temperature OFHC Copper. Regions of complete and partial spall are indicated. (Shadings indicate extent of spall; flag denotes only scattered void nucleation. Squares are present data; circles are from Reference 1.)

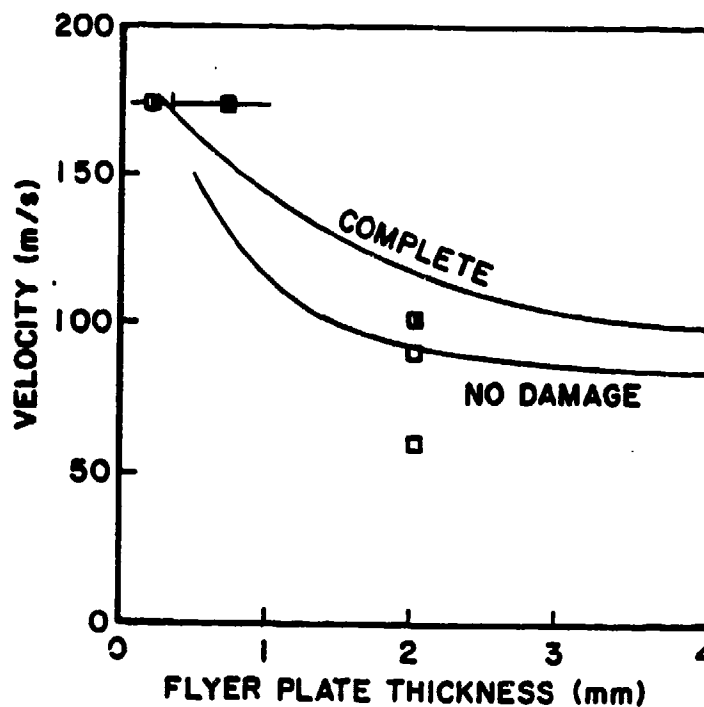


Figure 9. Spall Data for OFHC Copper at Elevated Temperature. (Symbols have same meanings as Figure 8.) Boundaries between complete and partial spall at ambient temperatures as shown for comparison.

The data for 2 mm thick flyers show the effect of temperature on spall threshold criteria. The critical velocity for initiation of damage at elevated temperature is 10 m/s (or 10 percent) higher than for ambient temperature.

Metallographic evaluation of the damaged regions of ambient and heated targets reveal significant differences in the void characteristics. Heated targets exhibit a relatively larger population of small voids which are dispersed over a relatively wide zone.

Figure 10 illustrates the appearance of the partial spall in ambient and elevated temperature targets. Figure 11 shows the corresponding void size distributions in the cross section. However, since these specimens were electrochemically polished, small voids may have been preferentially enlarged, accounting for the relatively depleted population of voids



a



b

Figure 10. Effect of Temperature on Spall Damage in OFHC Copper. (a) 20°C ( $u_0 = 95$  m/s, Shot 545), (b) 425°C ( $u_0 = 102$  m/s, Shot 541).

less than 60  $\mu\text{m}$ . The true void size distribution can be related to the apparent void distribution by assuming a void shape<sup>(3)</sup>. This has not been done with these data because the computation is extremely laborious.

The observations portrayed in Figures 8 through 12 lead to a qualitative understanding of how spall is effected by target temperature. The relative insensitivity of the partial spall threshold to temperature indicates that the stress history necessary for void nucleation does not depend strongly on temperature. The greater width of the damage zone in higher temperature targets suggests that the growth rate of voids is less in those targets; otherwise, prompt stress release on the spall plane would have quenched void growth elsewhere. These inferences are borne out by interpretation of the VISAR data, as explained below.

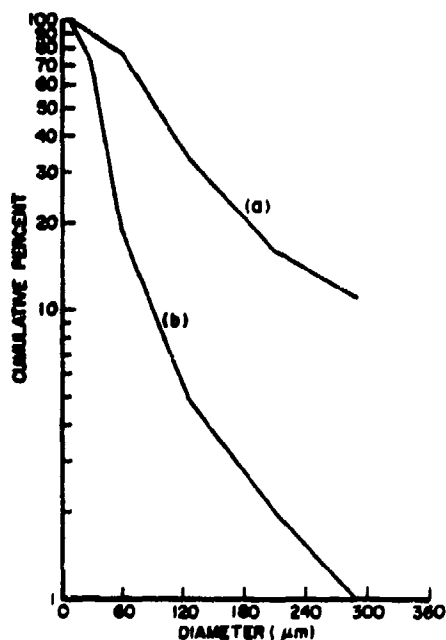


Figure 11. Apparent Void Size Distribution from Section in Figure 10. (a) 20°C, (b) 425°C.

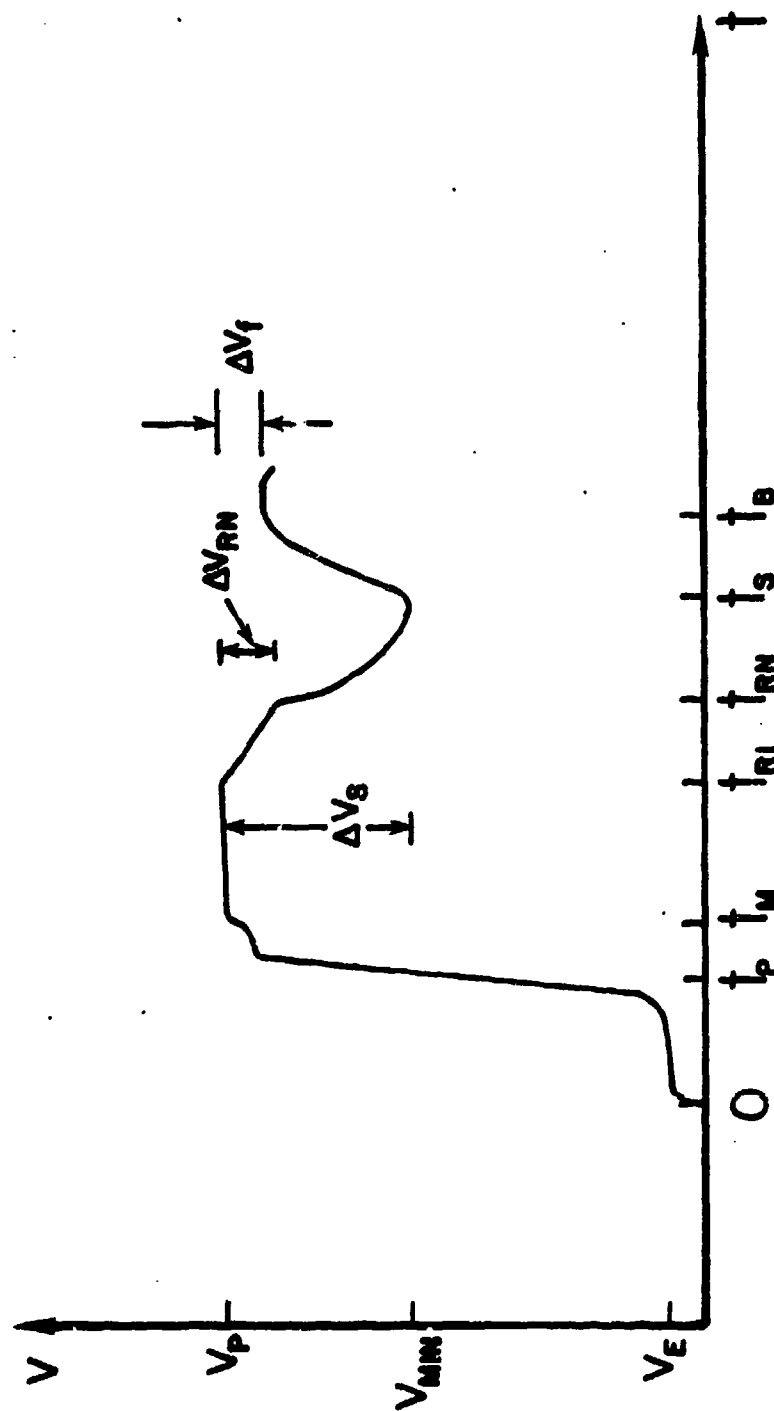


Figure 12. General Form of Free Surface Velocity History for Spalled Target.

### c. Free Surface Velocities

VISAR free surface velocity measurements were recorded for ten of the OFHC copper shots. These shots are representative of the combinations of various experimental parameters (i.e., flyer plate thickness, velocity). The level of confidence in the VISAR data is relatively high. For example, the average difference (nine shots) between the measured projectile velocity and the peak VISAR-measured velocity was only 2.5 percent.

Figure 12 represents a generalized free surface velocity history. Data for tests listed in Table II are shown in Figures 13 through 21. The quantities  $V_s$  and  $V_f$  may be related to the apparent spall stress\*  $\sigma'_s$  and apparent residual stress on the spall plane,  $\sigma'_r$ , by:

$$\sigma'_s = 1/2 \rho_o c_o \Delta V_s \quad (4)$$

and

$$\sigma'_r = 1/2 \rho_o c_o \Delta V_f \quad (5)$$

(For a discussion of these relationships, see Reference 2, for example.) These equations are only approximate; however, they tend to be more exact for materials like OFHC copper for which  $|\sigma_s|$  is relatively small, and spall development is relatively gradual. Values of  $\sigma'_s$  and  $\sigma'_r$  are listed in Table II for shots in which they were well determined.

The values of  $\sigma'_s$  calculated from equation (4) are all 11 to 12 kbar. This is true both for shots near threshold and for well above threshold, for wedge and flat flyer plates, and for target temperatures of 20°C and 425°C. Depending on the mechanics of the opening spall,  $\sigma'_s$  might be equal to  $\sigma_o$  (where voids first occur) or  $\sigma_s$  (where the fracture is at least 50 percent complete). The constant value observed for  $\sigma'_s$  for all types of tests is consistent with  $\sigma'_s \approx \sigma_s$ .

---

\*Spall stress is defined as the most tensile stress reached before spall occurred.



TABLE II  
DATA FOR COPPER

FLYER		TARGET		RESULTS			S/N
$u$ (m/s)	$d$ (mm)	$D$ (mm)	$T$ (NOM.) (°C)	DAMAGE O.=No Spall P.S.=Partial Spall S.=Spall	$\sigma'_s$ Kbar	$\sigma'_r$ Kbar	S/N
180	0,0.5,1.0	2.0	20°	0.3-1.0 mm S. 0.1-0.3 mm P.S.	12	0.2	551
142	0.5,1.2,1.9	4.0	20°	1.0-1.9 mm S. 0.5-1.0 mm P.S.			534
170	0.5,1.7,2.9	4.0	20°	0.5-2.9 mm S.			533
140	0.5,1.7,2.9	5.5	20°	1.25-2.9 mm S. 0.75-1.25 mm P.S. 0.50-0.75 mm O.			535
136	0.5,2.7,4.9	5.5	20°	1.0-4.9 mm S. 0.7-1.0 mm P.S. 0.5-0.7 mm O.	12		536
96	0.5,2.7,4.9	5.0	20°	1.5-4.9 mm P.S. 0.5-1.5 mm O.	11	7.3	537
95	2.0	4.0	20°	Partial Spall	12	9.3	545
196	2.0	9.0	20°	Spall	11	4.6	538
304	2.5	4.0	20°	Spall			513
86	4.0	9.0	20°	Partial Spall	11		540
102	4.0	6.0	20°	Partial Spall			562
123	4.0	6.0	20°	Spall	12	<9	561
209	4.0	6.0	20°	Spall	12	1.8	560
173	0.0,0.5,1.0	2.0	425°	0.3-1.0 mm S. 0.1-0.3 mm P.S.			552
60	2.0	4.0	425°	No Spall			549
90	2.0	4.0	425°	No Spall			543
102	2.0	4.0	425°	Partial Spall			541
102	2.0	4.0	425°	Partial Spall	12	4.9	542
196	2.0	9.0	425°	Spall			539

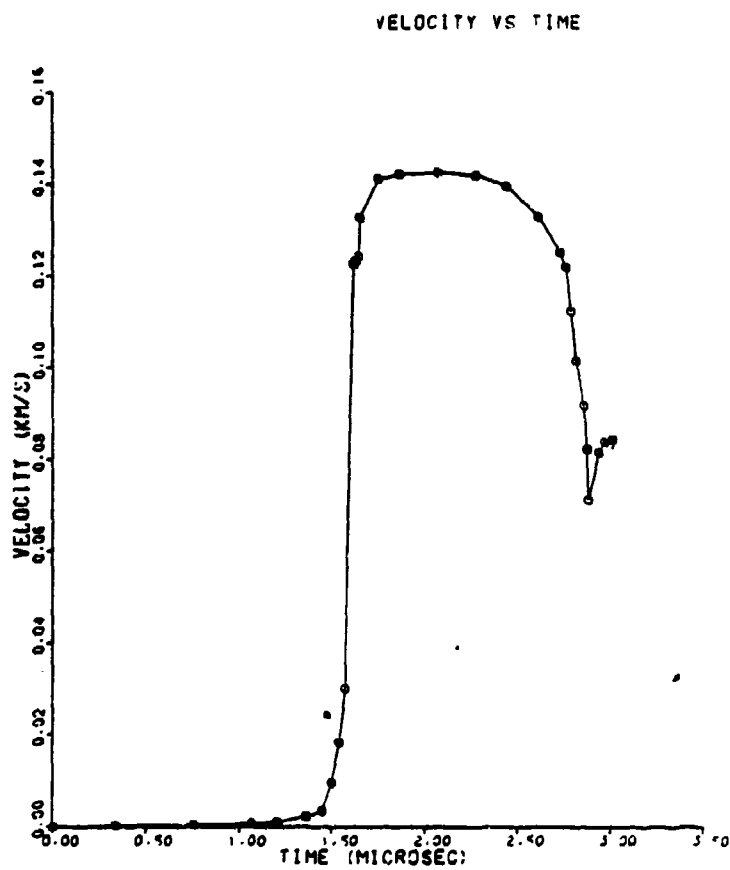


Figure 13. VISAR Data for Shot #7-536.

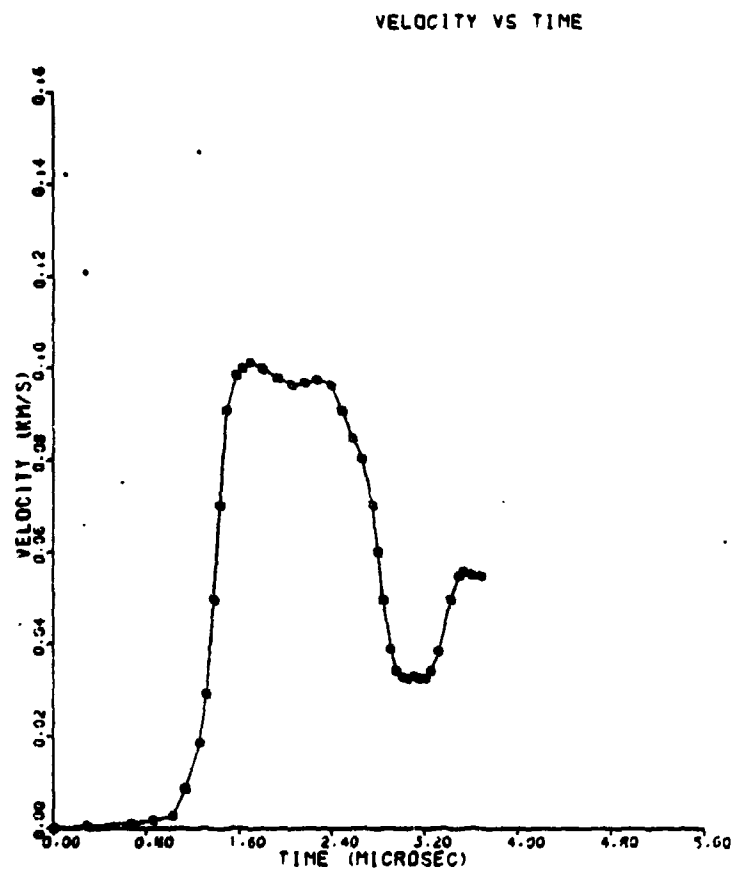


Figure 14. VISAR Data for Shot #7-537.

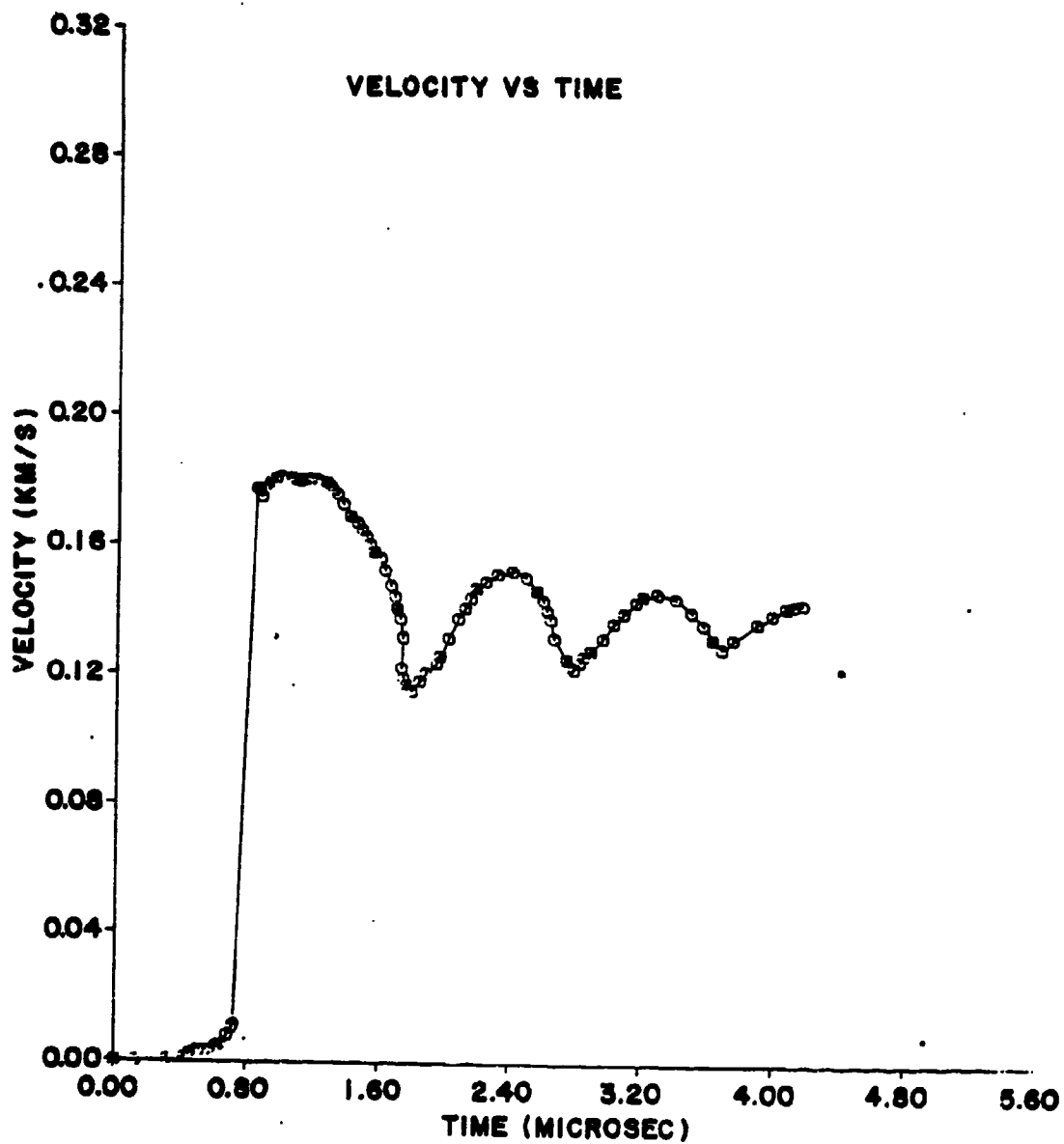


Figure 15. VISAR Data for Shot #7-538.

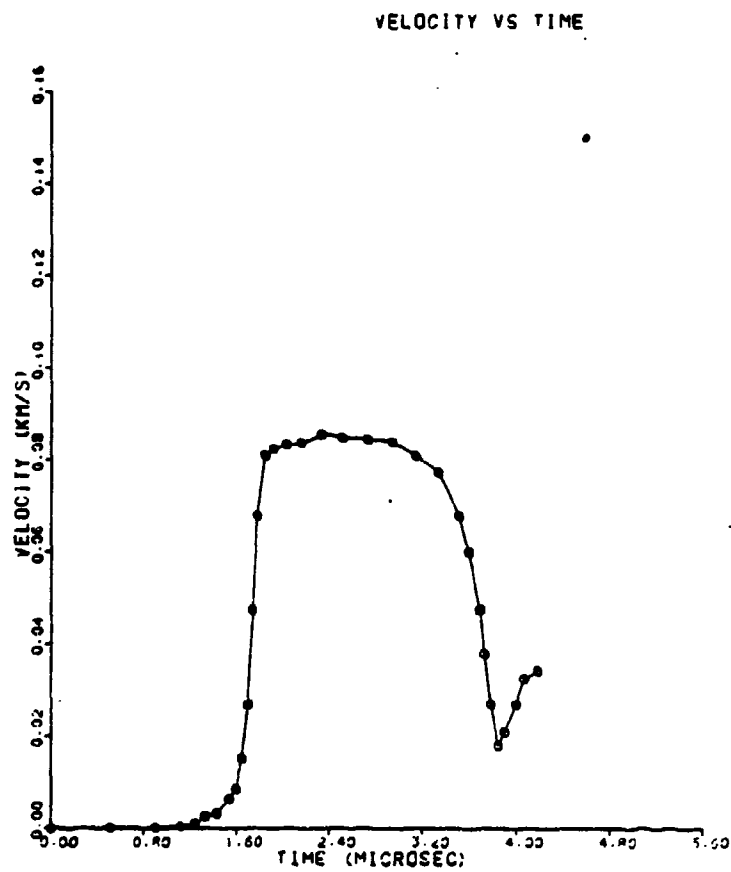


Figure 16. VISAR Data for Shot #7-540.

# VELOCITY VS TIME

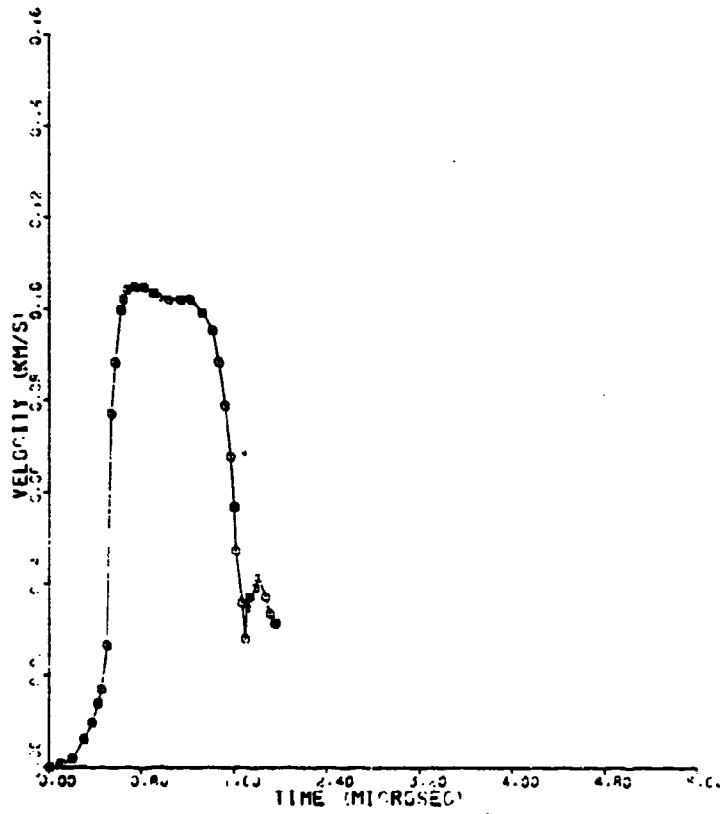


Figure 17. VISAR Data for Shot #7-542.

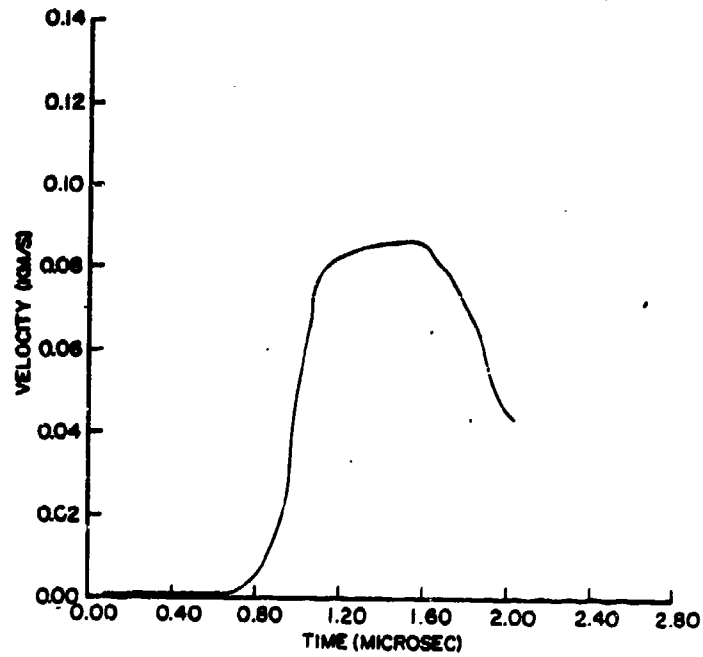


Figure 18. VISAR Data for Shot #7-543.

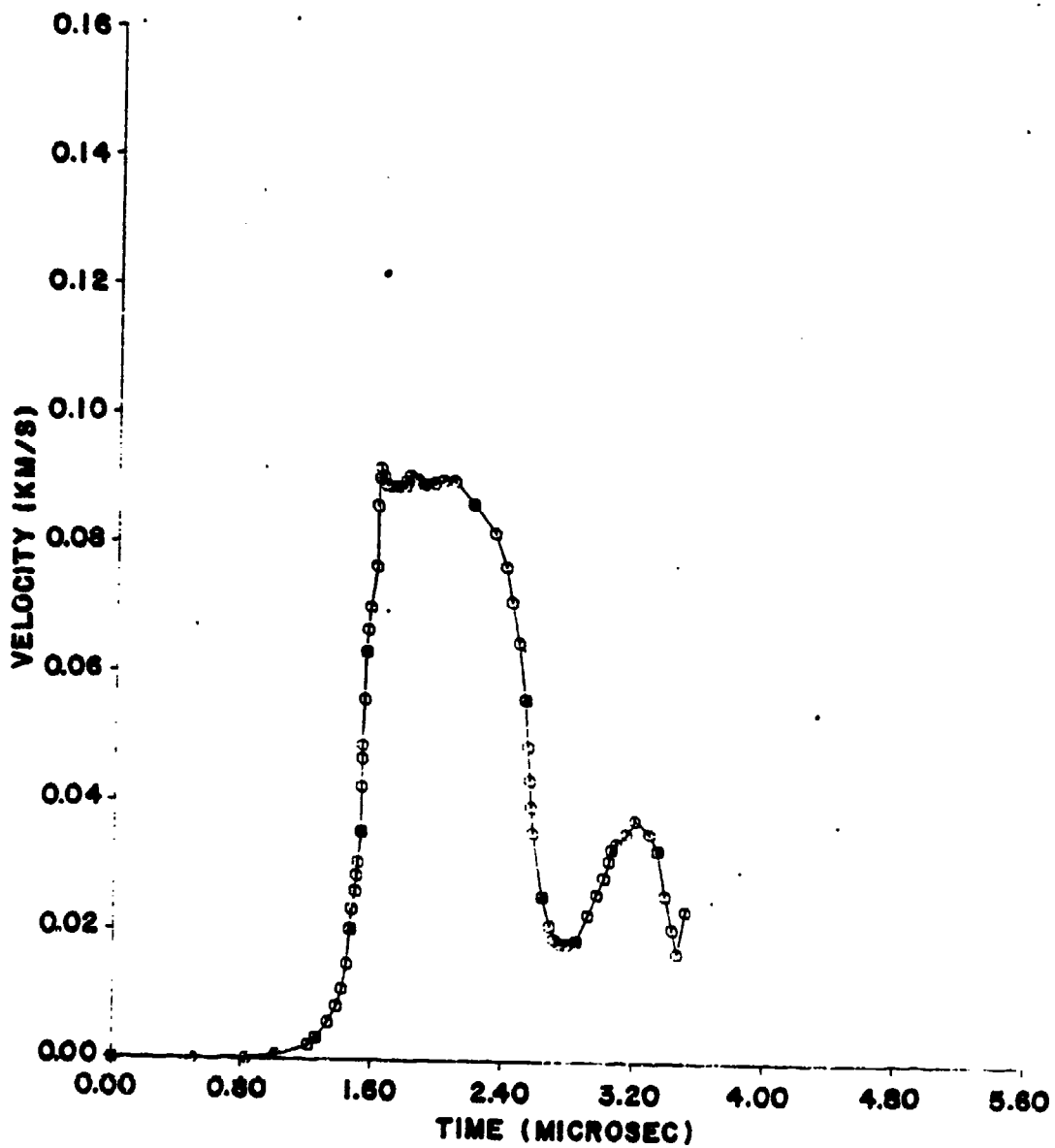


Figure 19. VISAR Data for Shot #7-545.

VELOCITY VS TIME

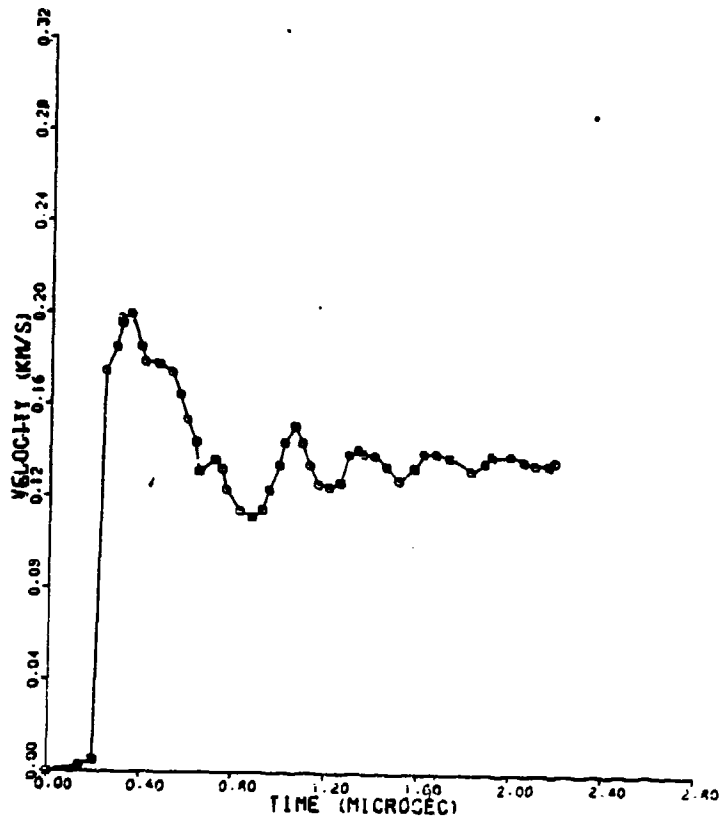


Figure 20. VISAR Data for Shot #7-552.



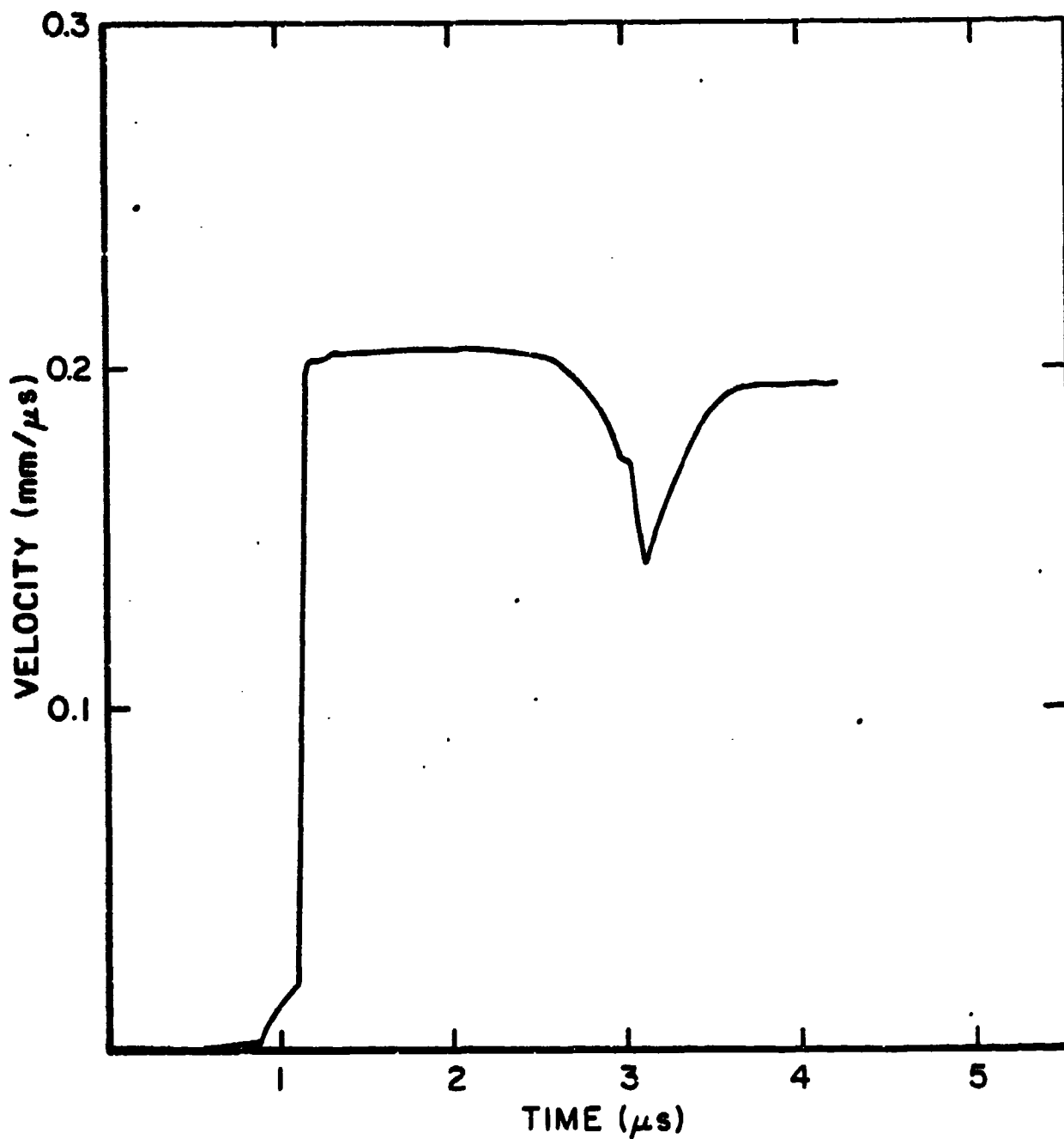


Figure 21. VISAR Data for Shot #7.560.

The data for  $\sigma'_r$  are relatively less complete. The value of  $\sigma'_r$  is nearly equal to  $\sigma'_s$  for elevated temperature targets. This indicates that damage accumulates gradually, and the stress on the spall plane after damage begins tends to be constant, and equal to  $\sigma'_s$ , rather than relaxing to zero. There is a tendency for  $\sigma'_r$  to be less when the spall is highly overdriven; this is consistent with relatively rapid fracture.

#### 4. RESULTS FOR MILD STEEL

Seven plate impact experiments were conducted with 1020 steel. Three of these were at ambient temperatures; those shots were intended to supplement the data reported in Reference 2. The other four tests were at 425°C. The test results are summarized in Table III.

The threshold data from Table III and Reference 2 are plotted in Figure 22. The wedge flyer datum provides dramatic evidence for the greater stress required to produce damage from short duration pulses. The data for 2-mm flyer plates clearly show that the steel is easier to spall at 425°C than at 20°C. The damage at 219 m/s at 425°C was an open crack, whereas even at 239 m/s at 20°C (Shot 107, Reference 2), the damage consisted of a line of partially connected voids that occupied just less than 50 percent of the spall plane. A complete crack formed at 20°C at  $u_0 = 283$  m/s (Shot 55, Reference 2). This is interpreted as indicating that the spall stress decreases 22 percent when the temperature is raised from 20°C to 425°C.

VISAR free surface velocity data obtained at 425°C in Shot 555 are shown in Figure 23.  $\Delta V_g = 123$  m/s for this shot, and  $\Delta V_f = 39$  m/s. This leads to  $\sigma'_g = 17$  kbar and  $\sigma'_r = 5$  kbar. The identification of  $\sigma'_g$  with  $\sigma'_s$  is very uncertain because calculations in Reference 2 showed that shocks from the spall surface formation reduce the observed value of  $\sigma'_g$  in steel (computed from Equation 4). The relatively low value of  $\sigma'_r$  indicates that spall was prompt and complete.

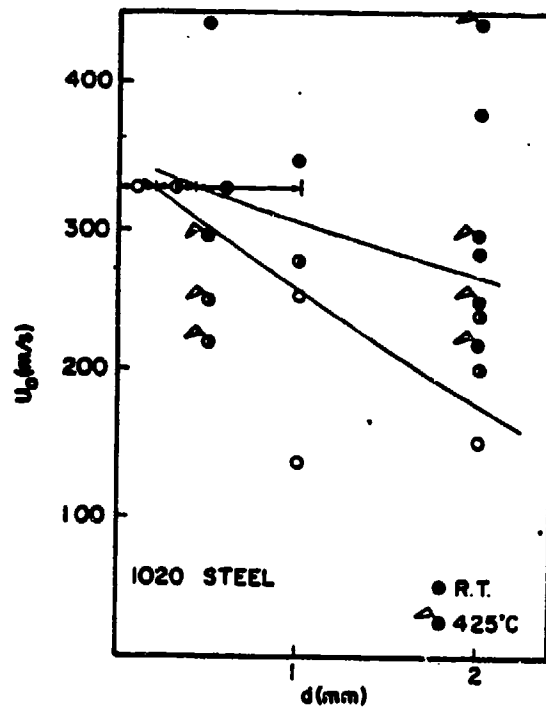


Figure 22. Spall Threshold Data for 1020 Steel. (Shading of dots indicates extent of fracture.)

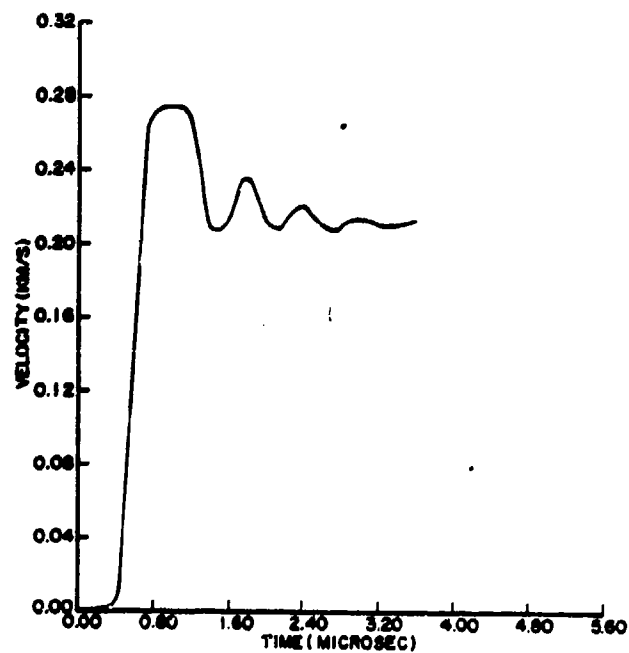


Figure 23. VISAR Data from Shot 555.

TABLE III  
DATA FOR 1020 STEEL

$\cdot u_o$ (m/s)	d (mm)	D (mm)	T (°C)	Results	S/N
150	2.0	4.0	20	spall	547
201	2.0	9.0	20	partial spall	553
320	0-1	2.0	20	<0.25 no spall 0.25-0.4 PS >0.4 spall	559
219	0.5/2	4.0	425	PS/spall	558
249	0.5/2	4.0	425	PS/spall	557
293	0.5/2	4.0	425	spall/spall	555
441	0.5/2	4.0	425	spall/spall	556

TABLE IV  
SPALL OBSERVATIONS IN 1100 ALUMINUM  
(Present Data Plus Data From Reference 2)

u (m/s)	d (mm)	T (mm)	Shot No.	Description	$x_s$ (mm)	F (%)
402	0 to 1.0	2.0	554	spall at $x_s=0.3$	0.3	50
211	1.0	4.0	376	no damage	---	0
234	1.0	4.0	383	no damage	---	0
300	1.0	4.0	272	connected voids	$0.83 \pm 0.06$	30
324	1.0	4.0	271	connected voids	NM	85
365	1.0	4.0	270	connected voids	$0.79 \pm 0.05$	70
472	1.0	5.0	51	cracks	$0.80 \pm 0.11$	75
590	1.0	5.0	50	voids	NM	NM
1556	1.0	5.0	52	voids	NM	NM
211	2.0	4.0	376	no damage	---	0
234	2.0	4.0	383	connected voids	NM	~80
270	2.0	4.0	500	NM	NM	NM
409	2.0	5.0	47	voids	---	--
570	2.0	5.0	49	connected voids	$1.95 \pm 0.09$	30
579	2.0	5.0	499	connected voids	NM	NM
894	2.0	5.0	106	connected voids	NM	NM
1024	2.0	5.0	48	connected voids	NM	NM

## 5. RESULTS FOR 1100 ALUMINUM

One test with an 1100 aluminum wedge flyer plate was conducted to complement the data in Reference 1. In Shot 554, a 0 to 1 mm thick tapered flyer plate was used with a 2 mm thick target. Two other tests, Shots 499 and 500, were carried out in order to obtain high quality free surface velocity data for spalled targets. The data are summarized in Table IV. In the table, F denotes the fracture of a cross section through the incipient spall plane that is occupied by voids.

The data show a clear dependence of  $\sigma_s$  on flyer plate thickness. The critical impact velocity for spall is between 211 and 234 m/s for  $d = 2$  mm, and about 300 m/s for  $d = 1$  mm. At  $u_0 = 400$  m/s, the critical value of  $d$  (deduced from the observed damage in Shot 554) is 0.3 mm. The value of  $\sigma'_s$  determined in Shot 499 was 13 kbar. Recovery was slight,  $\sigma'_r = 9$  kbar, showing incomplete void coalescence.

## 6. SWAP SIMULATIONS

SWAP code simulations were carried out for OFHC copper. The purpose was to calculate the stress history on the spall planes in order to better define spall criteria.

An  $(x,t)$  diagram for an OFHC copper experiment is shown in Figure 24. A conventional elastic plastic model was used with  $Y = 1$  kbar. This model accurately reproduced the observed shock waves, although the modeling of the release wave was rather crude, as shown in Figure 25.

Trial runs were made to improve the SWAP model of release wave structure. In particular, the unloading was modeled as a continuous plastic process. The isentrope was reflected around the  $\sigma$ -axes so unrealistic low values of  $\partial\sigma/\partial t$  would not accompany tensile stresses. The isentrope slope was varied to give an initial unloading speed equal to  $c_\ell$  and a final speed (at zero pressure) equal to  $c_0$ . Figure 26 illustrates an  $(x,t)$  diagram. The release fan from the flyer plate rear surface was successfully broken up into a large number of characteristics. However, since  $\partial\sigma/\partial t$  was such a strong function of pressure, a dramatic slow

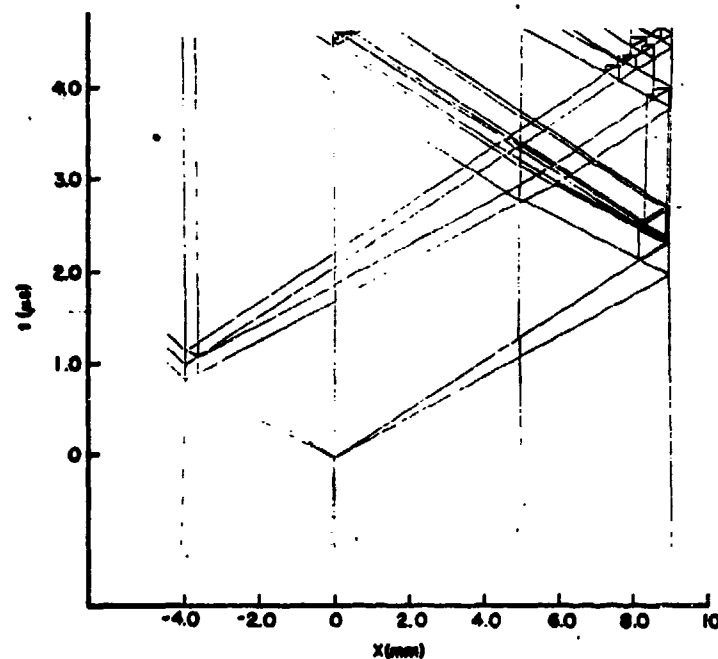


Figure 24. SWAP Elastic-plastic Calculation for Shot No. 540, (x,t) Diagram.

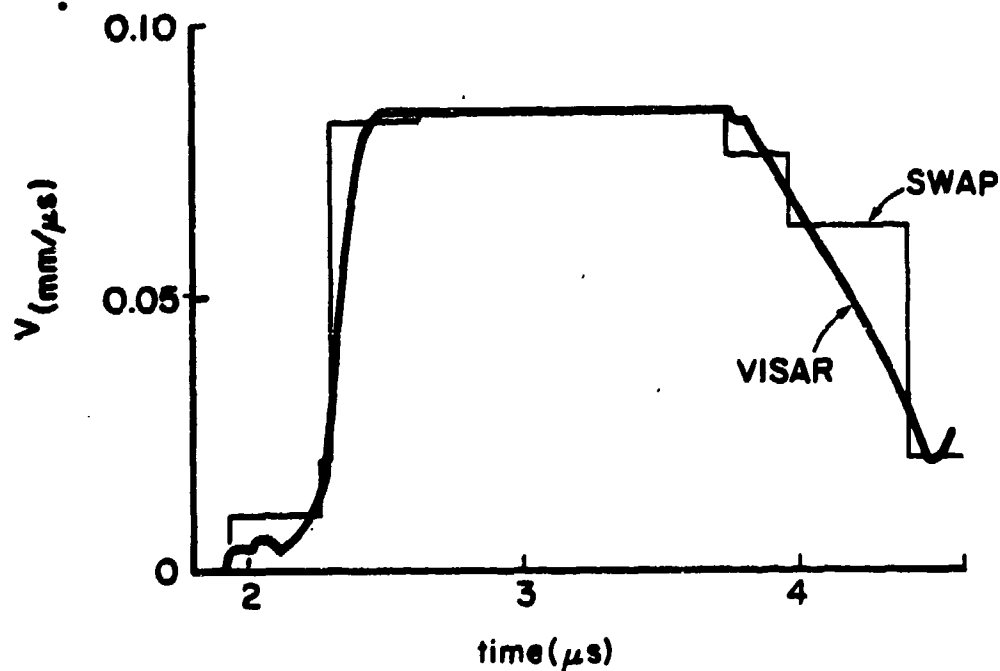


Figure 25. SWAP Elastic-plastic Calculation of VISAR Data for Shot No. 540.

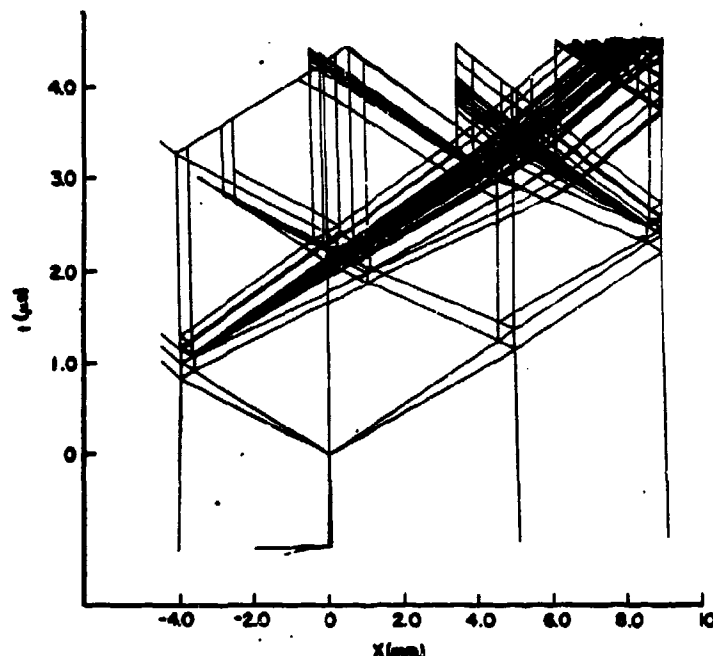


Figure 26. SWAP Calculation with Continuous Unloading Model (x,t) Diagram.

down of the characteristics occurred after the incipient spall plane was reached. This is probably unphysical and provides an interesting example in which an observed VISAR velocity record might be reproduced with a physically incorrect material description.

Since the unphysical slow down of release waves in Figure 26 precluded calibration of the all-plastic release model, it was decided to retain the elastic plastic description. When considering the  $(\sigma, t)$  records on the spall plane (Figure 27), the slight inaccuracies in computing  $\partial\sigma/\partial t$  along the leading and trailing edge do not significantly affect the accuracy of stress function integrals.

Spall criteria of the Tuler-Butcher form were investigated,

$$K = \int (\sigma - \sigma_0)^\lambda dt \text{ for } \sigma < \sigma_0 \quad (6)$$

The threshold data were best described by  $\sigma_0 = -7.5 \text{ kbar}$ ,  $\lambda = 2$ , and  $K = 19 \text{ kbar}^2 - \mu\text{s}$ . The predicted spall thresholds change little as  $K$  is increased, but  $K = 40 \text{ kbar}^2 - \mu\text{s}$  is clearly an inferior fit to the measured data. Figure 28 compares the measured and computed thresholds. This value even described spall in Shot 560, for which spall occurred at  $K = 37 \text{ kbar}^2 - \mu\text{s}$ .

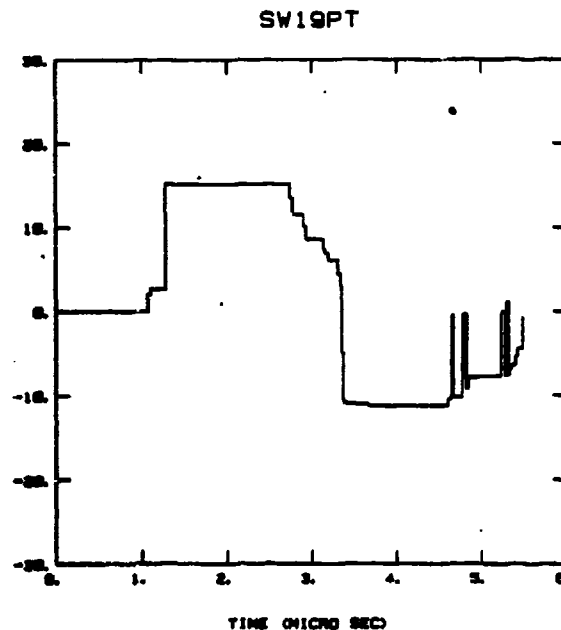


Figure 27. Stress History on Spall Plane for Calculation Depicted in Figures 24 and 25. (Stress is in kbar).

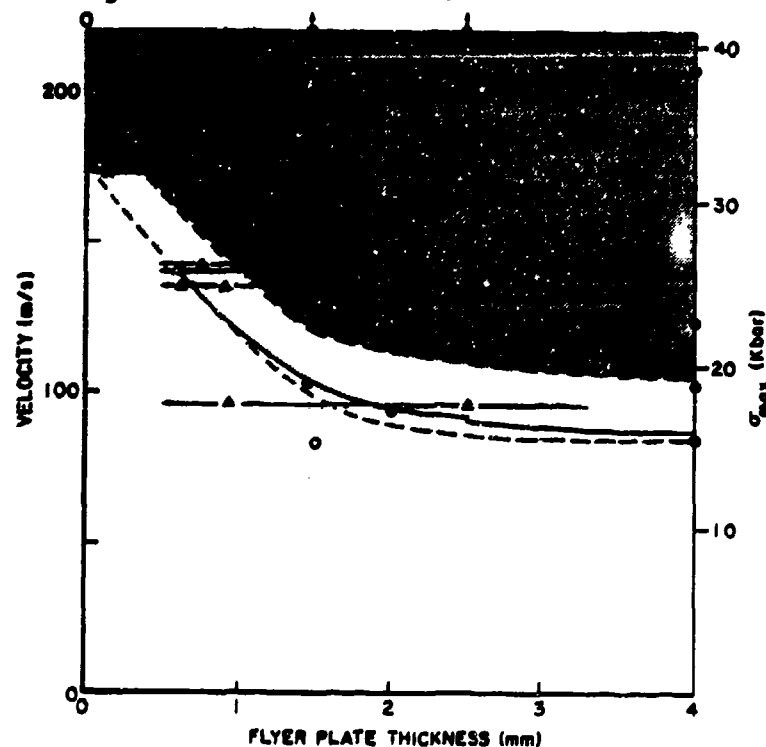


Figure 28. Tuler-Butcher Prediction of Spall Thresholds for  $K = 19 \text{ kbar}^2 \cdot \mu\text{s}$  ( $D = 4 \text{ mm}$  for  $d < 2.5 \text{ mm}$ ;  $D = 9 \text{ mm}$  for  $d > 2.5 \text{ mm}$ ).



### SECTION III

#### TENSILE TESTS WITH A HOPKINSON BAR

The split Hopkinson bar provides one of the few research tools for investigating the behavior of materials under uniaxial stress loading at strain rates above  $500 \text{ s}^{-1}$ . The University's Hopkinson bar has been designed to measure tensile, as well as compressive, stress-strain relationships. It has also been augmented to permit studies of necking specimens.

##### 1. HOPKINSON BAR APPARATUS

A split Hopkinson bar consists of three in-line bars, a striker bar, a pressure bar, and a transmission bar. The University's bars are 12.7 mm diameter. The striker bar is launched by a torsional spring. Its speed is measured as it crosses two lamp/photodetector stations. The striker bar strikes the pressure bar, producing an elastic compressive stress wave travelling at  $C_E = \sqrt{E/\rho}$ . The duration of the stress wave is twice the transit time through the striker bar, 300  $\mu\text{s}$ . For compressive tests, a button sample is placed between the pressure and transmission bars. For tensile tests, a collar is placed around the specimen to transmit the compressive pulse from the pressure bar to the transmission bar. The pressure wave reflects at the free end of the transmission bar and returns as a tensile wave. The specimen, shown in Figure 29, is screwed into both the transmission bar and pressure bar. The specimen is loaded in tension by the tensile pulse arriving in the transmission bar. Analyses of the stress waves reflected and transmitted by the sample can be used to deduce the stress-strain history of the specimen.

The Hopkinson bar apparatus used in this program is essentially identical to that described in References 1 and 3. A number of minor mechanical modifications were carried out. The bars were realigned, which necessitated reworking the Teflon

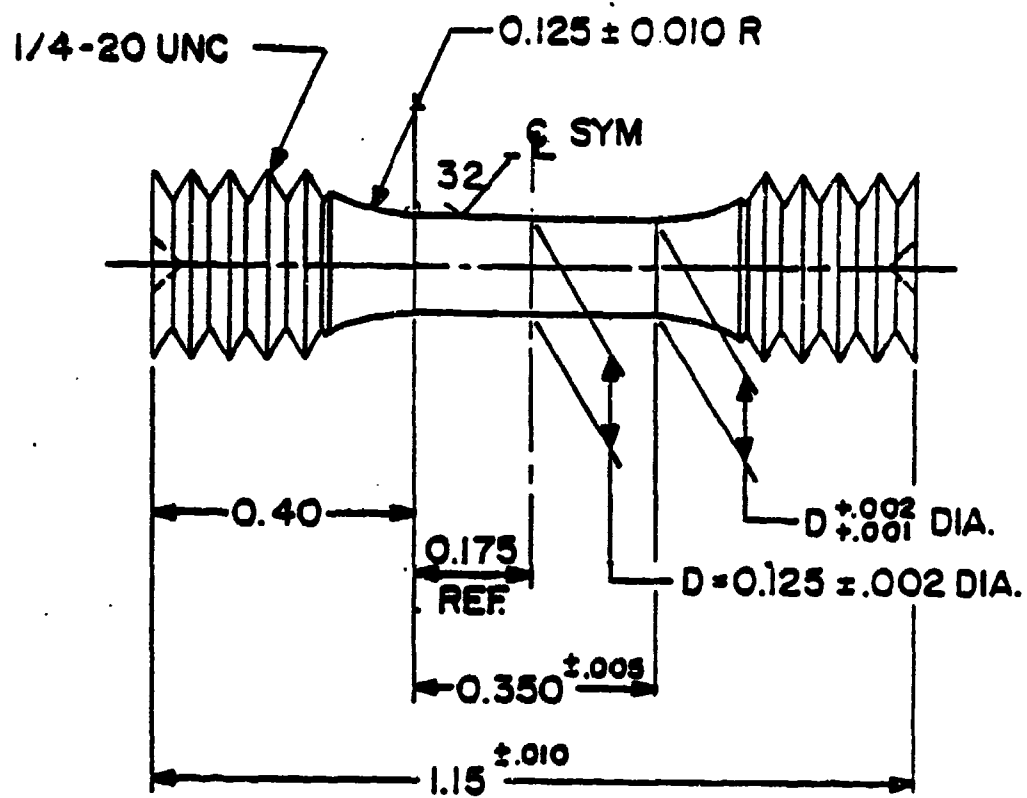


Figure 29. Hopkinson Bar Specimen Design (Dimensions in Inches).

bushing mounts, an oven was designed and fabricated, and new strain gauges were mounted.

The essential equations used to calculate specimen stress and strain have been described by many authors (for example, Reference 3). A brief account is given here for completeness.

Strain gauges are placed equi-distant from the sample. When the bar apparatus is used as a compression test, the initial compressive pulse is transmitted to the sample. The incoming pulse is partially transmitted through the sample, and partially reflected. Since the bars are much larger than the specimen, the boundary condition imposed is nearly one of constant velocity, or, equivalently, strain rate.

The specimen stress is given by:

$$\sigma_{sp} = E \frac{A_b}{A_s} \epsilon_t \quad (7)$$

where  $E$  and  $\epsilon_t$  are the Young's modulus of the bar and the transmitted strain and  $A_b/A_s$  is the ratio of bar cross sectional area to sample cross sectional area. The specimen strain rate is given by:

$$\dot{\epsilon}_s = -\frac{2c}{l} E \epsilon_r \quad (8)$$

Where  $l$  is the sample length (effective gauge length) and  $\epsilon_r$  and  $\epsilon_s$  are reflected strain and specimen strain. Following Reference 4,  $l$  was set equal to 8.9 mm.

These equations show that the specimen strain is obtained by integrating the strain pulse reflected from the specimen, the specimen stress, is proportional to the transmitted strain pulse, and the strain rate is proportional to the reflected strain pulse. The equations show that high strain rates are obtained by high striker velocities or short sample lengths. The equations are not valid for elastic response because equilibrium is not

established during the time needed for the sample to "ring up" to the bar boundary conditions, as discussed above.

The above equations give average, or engineering, stress and strain. True stress and strain can be computed from:

$$\sigma_T = \sigma_{sp}(1 - \epsilon_s) \quad (9)$$

and

$$\epsilon_T = \ln(1 - \epsilon_s) \quad (10)$$

The bar strain gauges are calibrated by performing a compressive test with no specimen<sup>(4)</sup>. Two bar materials were used: 4340 steel and Inconel 718.

## 2. DIAGNOSTIC TESTS OF HOPKINSON BAR

A study was conducted in order to optimize data recovery from the Hopkinson bar and check for possible systematic errors. The objectives were as follows:

- Determine the bandwidth requirements for the measurement system.
- Determine the amount of sample prestrain that occurs when the compressive pulse passes through the collar.
- Check that the "effective gauge length," determined previously<sup>(4)</sup>, was correct at high strain rates.
- Check that the computed specimen stress is correct.

### a. Signal Recording

In order to establish the actual bandwidth of the amplifiers, a 10 kHz square wave was generated and driven through each set of amplifiers. The square wave approximated the wave shape experienced in the Hopkinson bar test.

The square wave signal was driven through both the amplifiers currently in use<sup>(1,4)</sup> ("SRL" amplifiers) and a set of 1A7A Tektronix amplifiers, to see if a better response could be

gained by replacing the amplifiers. On the old set up, there was an oscillation of the signal at the leading edge of the wave, as shown in Figure 30. This oscillation was due to the rapid rise time of the signal and the bandwidth limitation of the amplifier.

The same signal was driven through the 1A7A amplifiers. This type amplifier has a bandwidth of at least 1 MHz, and a selectable low pass filter range of 10 kHz to 1 MHz. The pulse was driven through filter settings of 1 MHz, 300 kHz, 100 kHz, and 30 kHz. The results for the 1 MHz and 100 kHz settings are shown in Figures 31 and 32. At 1 MHz the signal is passed without distortion. Reduction of the filter frequency from 1 MHz to 300 kHz, reduces the high frequency noise without affecting the highest frequency components of the signal. If the filter cutoff frequency is reduced to 100 kHz or lower, significant high frequency components of the signal are lost, causing the leading edge of the wave to be rounded. Therefore, all subsequent experiments have been conducted with the Tektronix amplifiers set at 300 kHz.

Some earlier data had also displayed a confusing zero line shift between the first compressive wave and the returning tensile pulse. A second set of strain gauges was attached to the long bar, just in front of the first set, and a test was conducted to determine the cause of the shift in the zero line voltage. The original gauges were put on separate bridges and attached to separate channels of the amplifier. The individual traces were recorded. Although for small disturbances, the two signals were 180 degrees out of phase, there was considerable difference in the voltage between the two signals at larger time scales. The 180 degree out-of-phase signals are ascribed to bending in the bar. The addition of the response of the gauges causes the out-of-phase components to cancel; however, due to the drift in zero-line voltage, complete cancellation did not occur. Next, the same test was conducted on the new set of strain gages. The results (Figure 33) showed the 180 degree out-of-phase

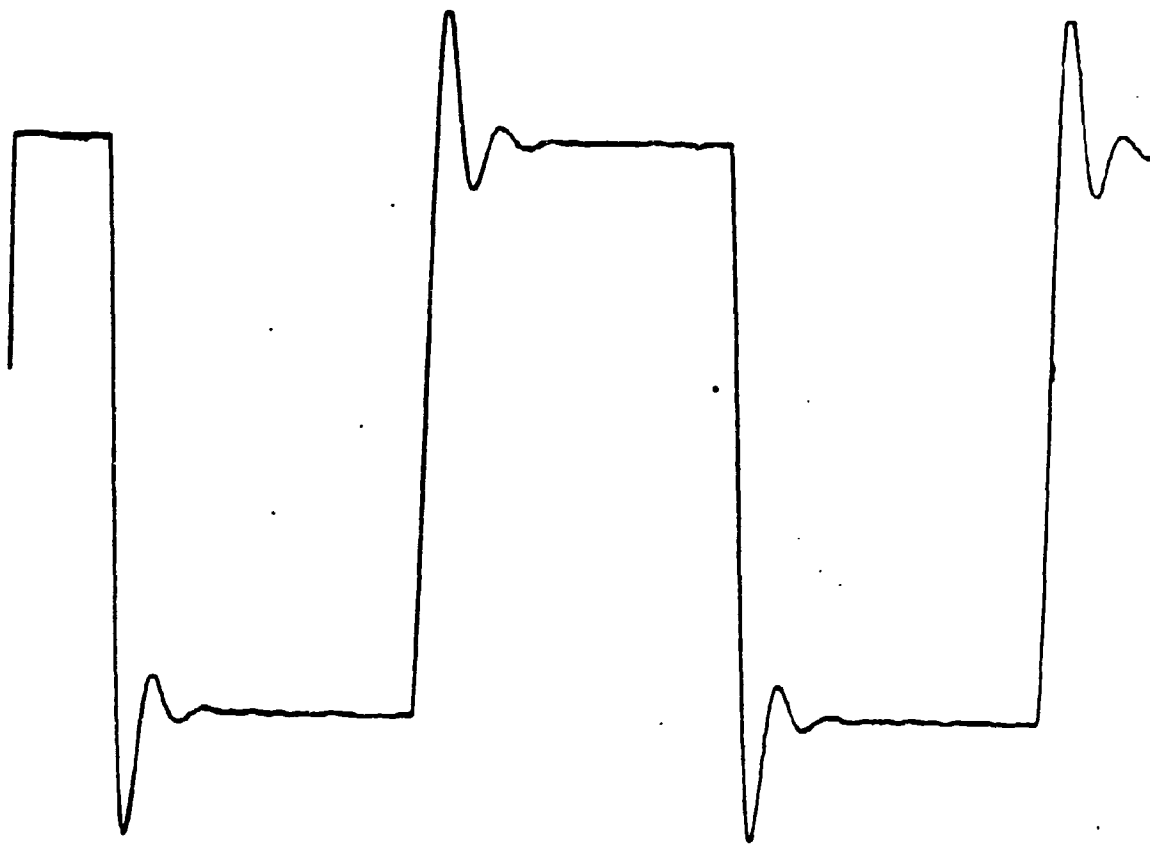


Figure 30. Response of the SRL Amplifiers to a 10 kHz Square Wave Signal.

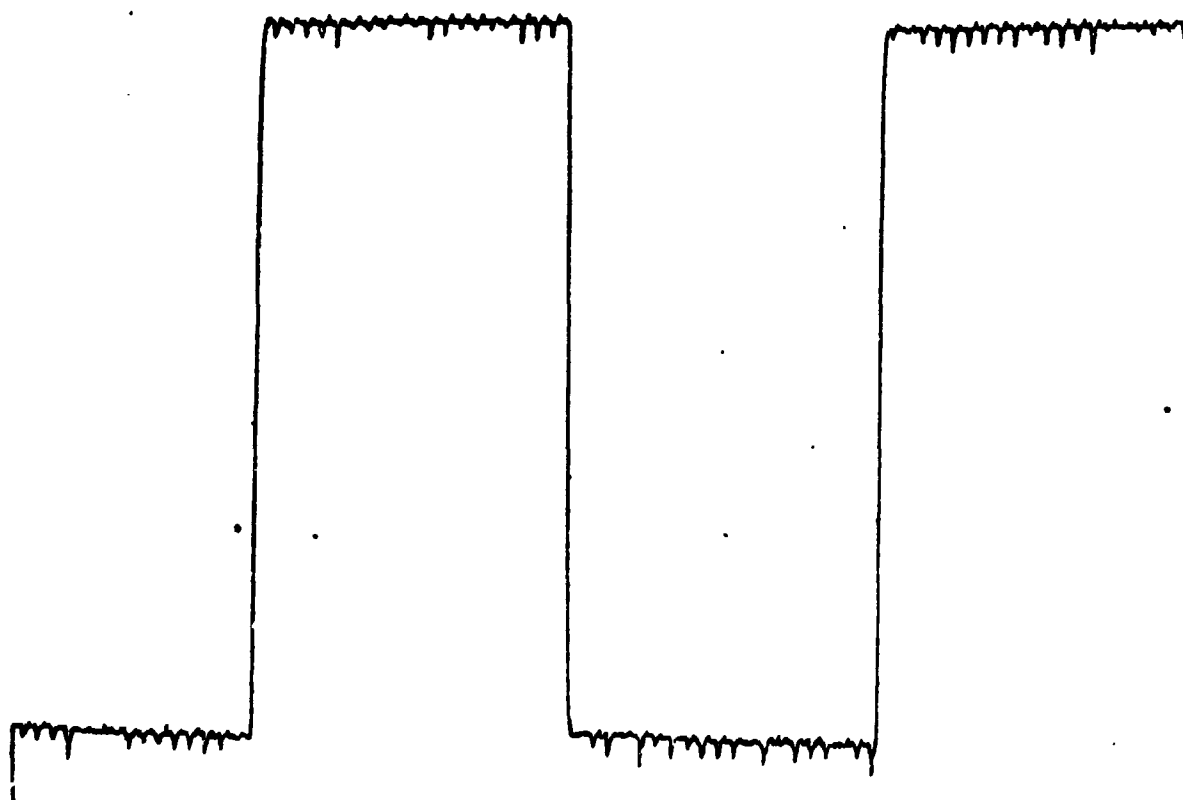


Figure 31. Response of the 1A7A Tektronix Amplifier to a 10 kHz Square Wave with a 1 MHz Filter Setting.

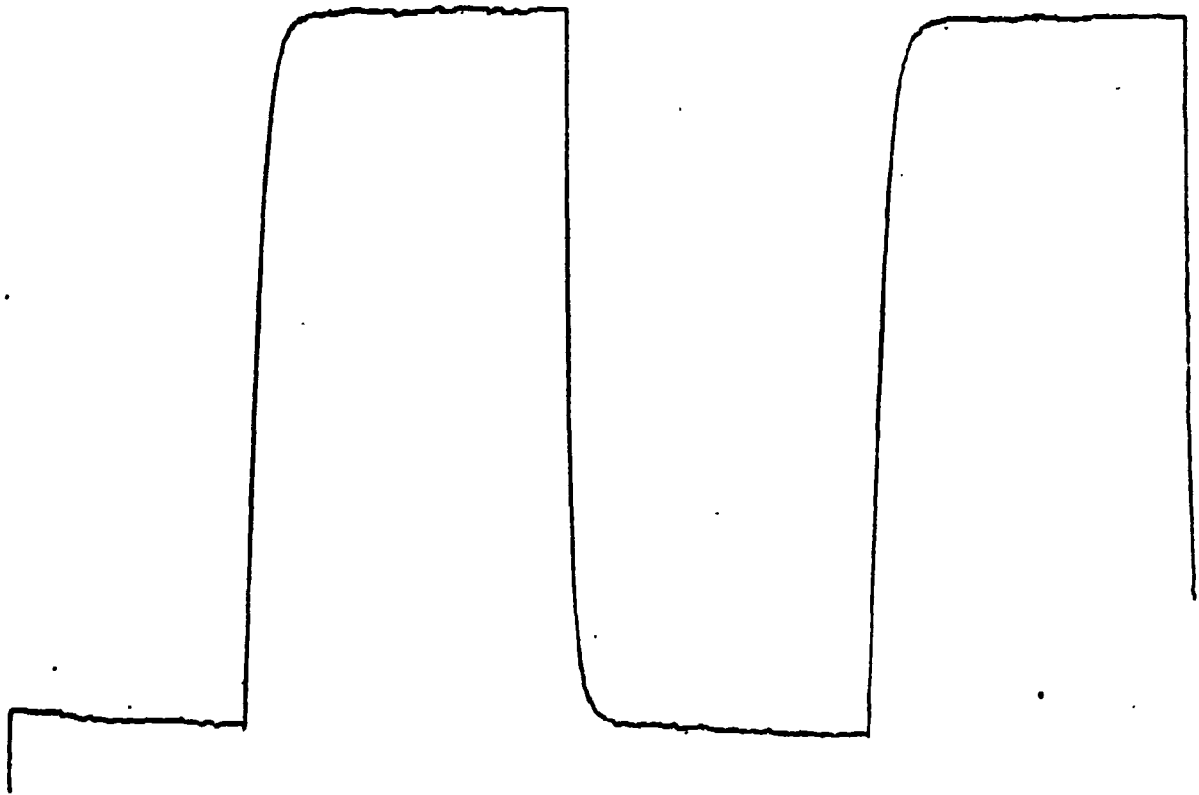


Figure 32. Response of the 1A7A Tektronix Amplifier to a 10 kHz Square Wave with a 100 kHz Filter Setting.

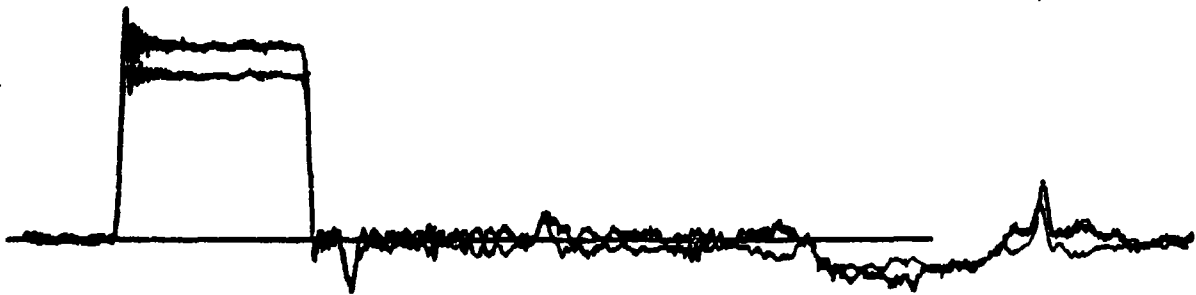


Figure 33. Separate Traces of Hopkinson Bar Strain Gages on the First Bar (the Differences in Amplitude are Due to an Offset in the Gain of the Two Amplifiers).



components as before; however, the drifts in voltage were much smaller. Thus, the previous zero line shift was evidently due to one bad strain gauge, and it was cured by gauge replacement.

### b. Stress Validation

The accuracy of the Hopkinson bar was checked by performing experiments with 6061-T6 aluminum. This material is well known to have relatively rate-independent constitutive properties<sup>(4)</sup>. Three samples were tested statically. Then six specimens were tested with the Hopkinson bar, two each at three different strain rates. One trace at each strain rate is shown in Figure 34. The repeatability of tests at the same strain rate was better than could be resolved. The difference between the static and dynamic ultimate stress was 8.1 percent. The average static and dynamic behavior is compared in Figure 35.

According to Reference 5, the ultimate stress of this material at  $10^3 \text{ s}^{-1}$  is  $4.0 \pm 0.1$  kbar. Our mean value at 220 to  $550 \text{ s}^{-1}$  was  $3.73 \pm 0.12$  kbar.

### 3. NECKING

The boundary condition in a Hopkinson bar specimen is one-dimensional stress. It follows that the ratio of mean stress to effective stress:

$$\sigma_m / \sigma_{\text{eff}} = -1/3 \quad (11)$$

This stress trajectory limits the utility of Hopkinson bar experiments for study of impact-induced tensile fracture. In flat plate impact tests

$$\sigma_m / \sigma_{\text{eff}} \ll -1. \quad (12)$$

In scenarios of engineering interest, fracture takes place at values of  $\sigma_m / \sigma_{\text{eff}}$  considerably less than  $-1/3$ , but seldom as negative as in a flat-plate spall test. Unfortunately, available

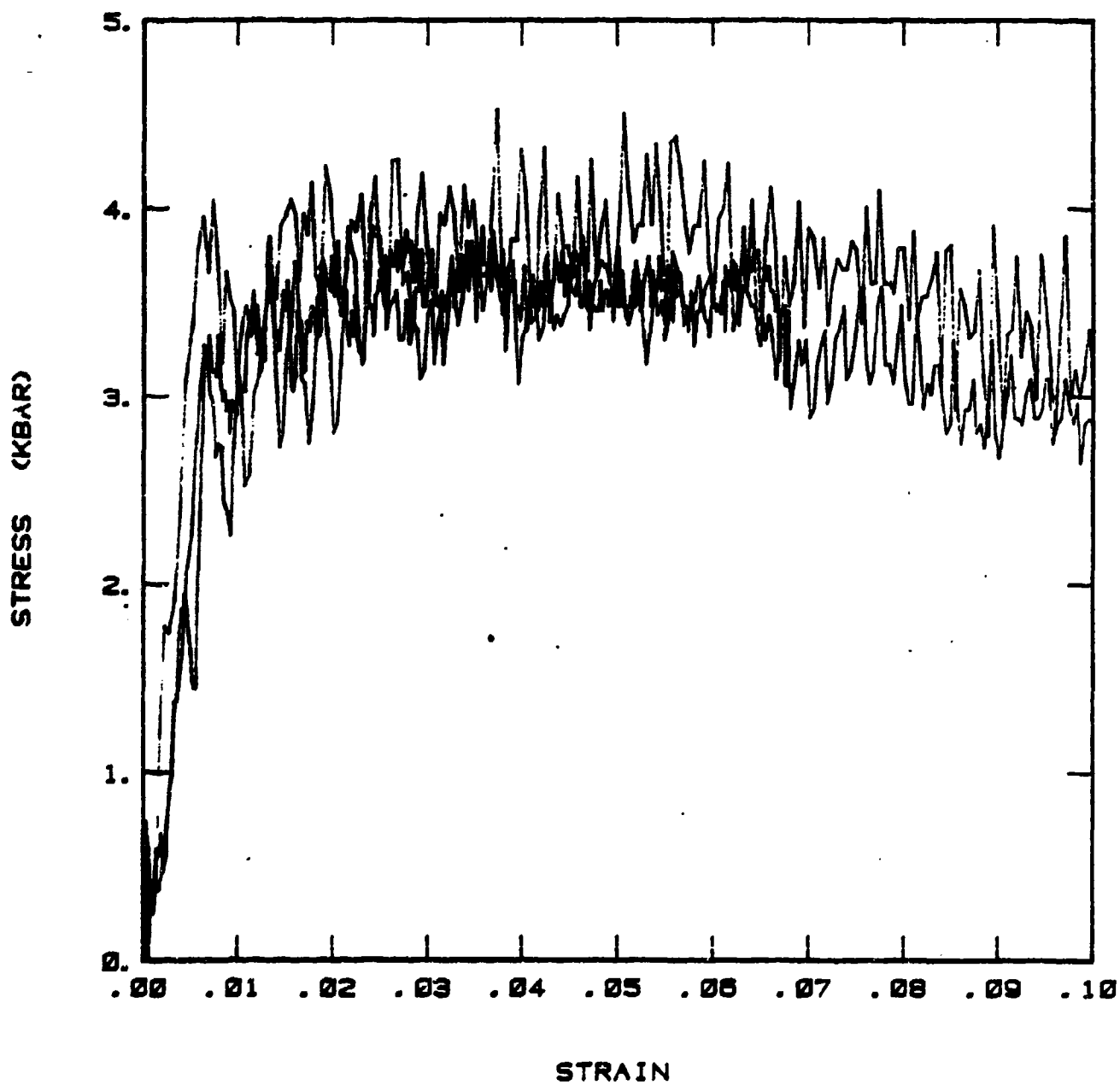


Figure 34. Results of Three Tests on 6061-T6 Aluminum at  $500 \text{ s}^{-1}$ ,  $350 \text{ s}^{-1}$ , and  $200 \text{ s}^{-1}$ .

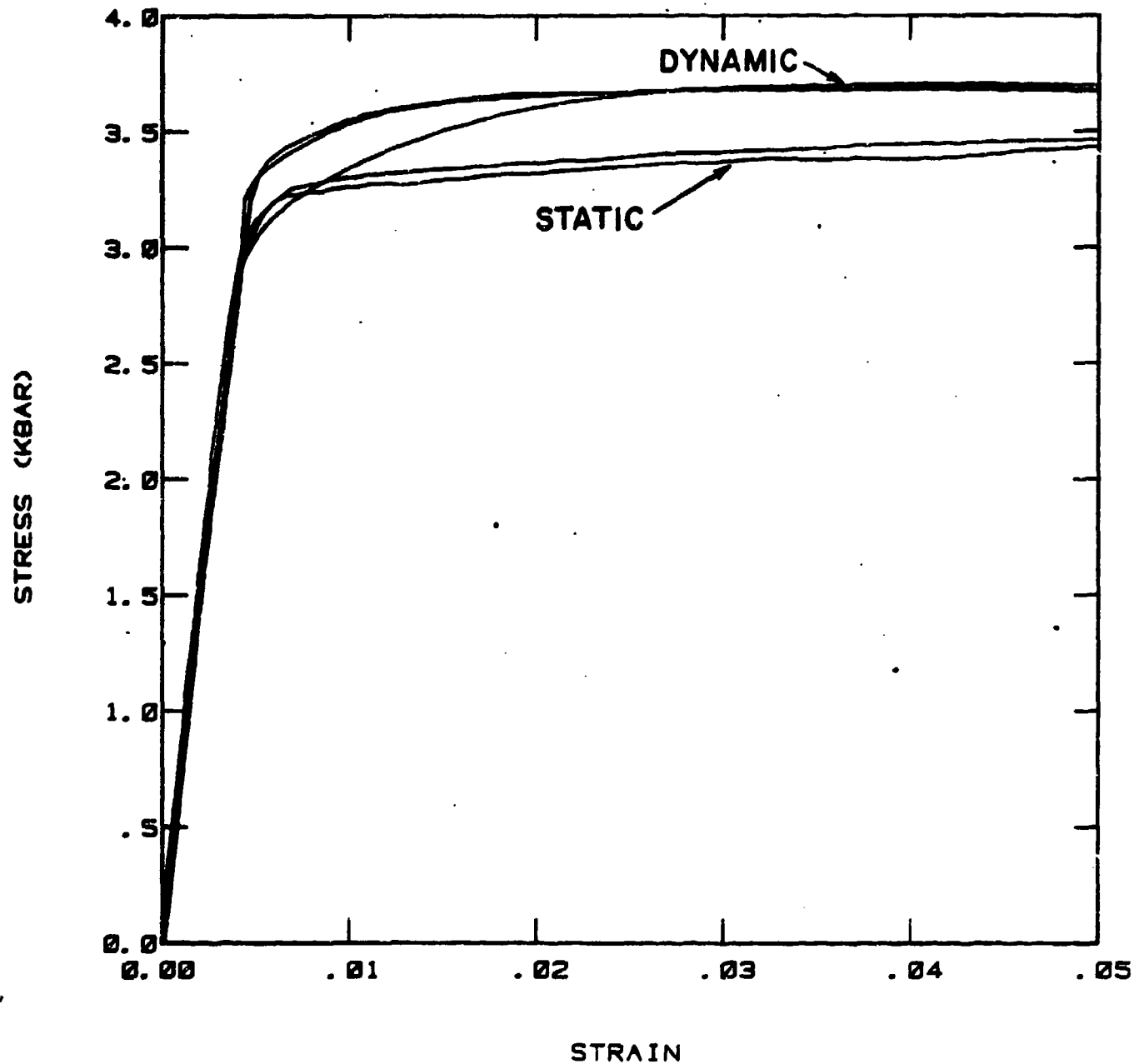


Figure 35. Comparison of the Hopkinson Bar Analysis of 6061-T6 at Three Different Strain Rates to the Static Results of the Same Material. (Hopkinson bar data are smoothed.)

data generally show that the value of  $\epsilon_p$  associated with fracture is often ten times greater in a Hopkinson bar test than in a spall test. Hence, there is a critical need to develop experimental techniques to investigate dynamic fracture at intermediate values of  $\sigma_m/\sigma_{eff}$ .

a. Non-uniform Tensile Specimens

Specimens undergoing rapid tensile deformation are subject to a well-known necking instability. As the specimen cross section becomes non-uniform, the stress tensor becomes more spherical, and the value of  $\sigma_m/\sigma_{eff}$  decreases.

In spite of several analyses of necking behavior<sup>(6,7,8)</sup>, the state of stress and strain in a necked sample is only approximately known. The most useful and widely used approximation for the stress state in a necked specimen is that of Bridgeman<sup>(5)</sup>. The axial strain,  $\epsilon_z$ , across the neck is assumed uniform and equal to:

$$\epsilon_z = 2 \ln d/d_0 \quad (13)$$

where  $d$  is the current neck diameter and  $d_0$  is the original diameter. The effective stress is related to the engineering stress,  $\sigma_{eng}$ ,

$$\sigma_{eff} = B \sigma_{eng} \quad (14)$$

where  $B$  is given by

$$B = \frac{(a_0/r)^2}{[(a/r)^2 + 2(a/r)] \ln[1 + (a/r)/2]} \quad (15)$$

Here  $a = d/2$ ,  $a_0 = d_0/2$ , and  $R$  is the radius of curvature of a circle that osculates the specimen at the necked silhouette. The engineering stress is just the applied load divided by  $\pi a_0^2$ . The ratio  $\sigma_m/\sigma_{eff}$  is given by:

$$\frac{\sigma_m}{\sigma_{eff}} = \frac{1}{3} + \ln \left( \frac{a}{2R} + 1 \right) \quad (16)$$

This analysis has been used to obtain fracture data at values of  $\sigma_m/\sigma_{eff}$  up to -1.4 at low strain rates using prenotched specimens<sup>(9)</sup>.

The Bridgeman analysis is based on assumptions of uniform strain and  $\sigma_z = \sigma_\theta$ . It also implies the assumption that void formation has not begun. The effects of void growth on stress distribution in a necked specimen have been treated in Reference 10. Bridgeman type analyses were shown to be valid only up until void formation begins. This is not a concern in the present study because sectioning of specimens that have failed in Hopkinson bar tests indicates that the void formation and growth was very rapid and is significant only immediately preceeding rupture.

#### b. Finite Element Analysis of a Necked Specimen

The analysis of necked specimens began with the analysis of specimens with a preformed circular notch. The stress-strain states at the notch section were computed through the finite element method for the specimen geometry shown in Figure 36. The specimen geometry was modelled after those used in Reference 9, which used the Bridgeman analysis<sup>(6)</sup>. The present investigation was carried out for the following three distinct reasons.

1. To check the validity of Bridgeman stress-strain state at the minimum cross-section of the notch under static and dynamic loading conditions.
2. To calculate the stress-strain state at the notch for various loading conditions through finite element analysis.
3. To verify the validity of the developed constitutive models under triaxial stress-state by comparing the loads

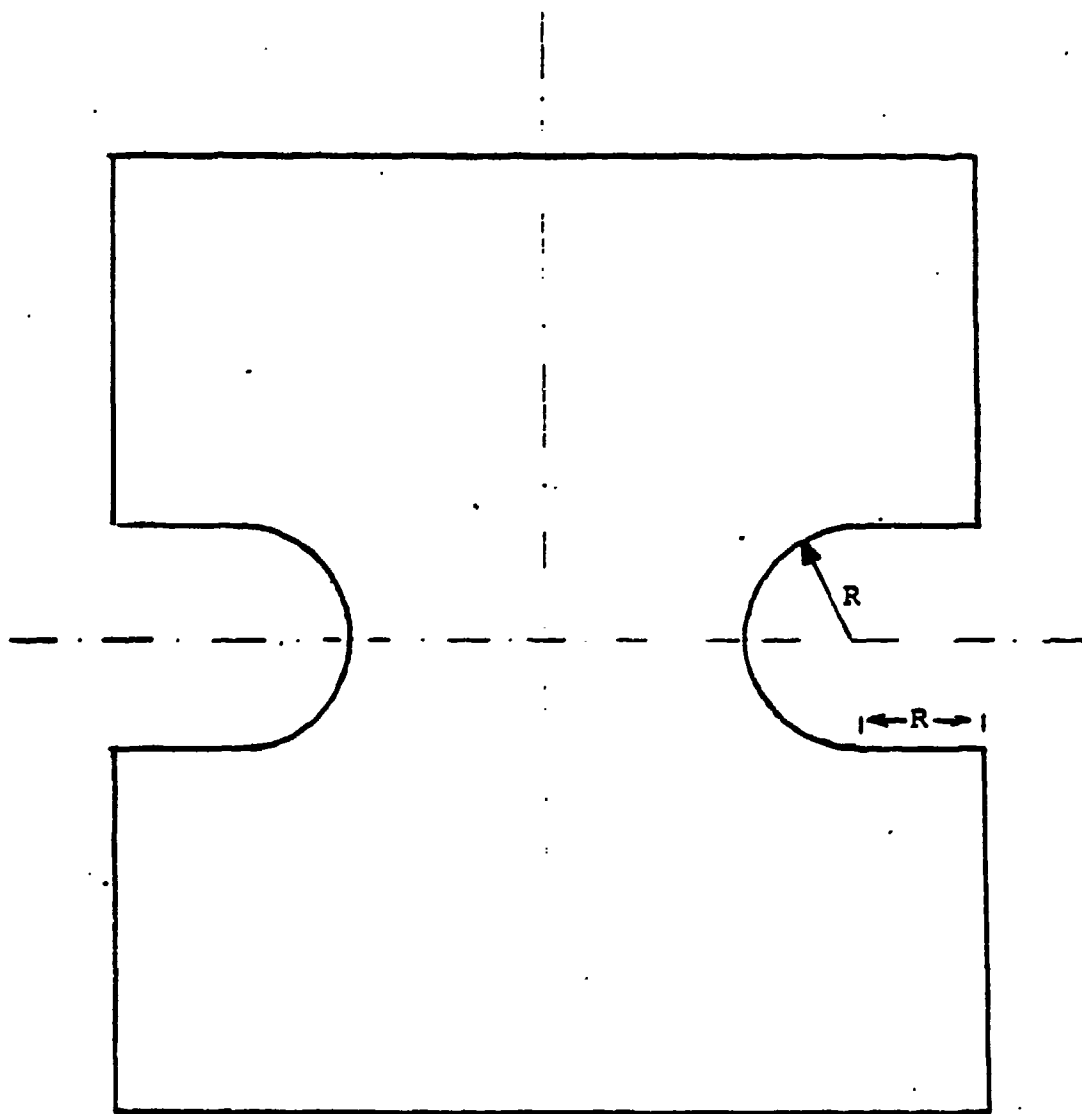


Figure 36. Axi-symmetric Notched Tensile Specimen.

and displacements in numerically simulated notched tensile specimens to those measured in actual tests.

As of this report, the first and second aims have been partially accomplished through the numerical solutions of the notched tensile specimen under static and dynamic loading conditions. Calculations were carried out with the MAGNA finite element program for a pull velocity of 10 m/s under dynamic and static loading. In static analysis, the pull velocity was used without inertia effects. In that case, the time steps became dummy variables. The pull velocity was not applied instantaneously; instead a quarter sinusoidal waveshape was assumed with a rise time of 10  $\mu$ s as shown in Figure 37. Since the notched tensile specimen is an axisymmetric geometry, special axisymmetric two-dimensional elements were employed for the finite element analysis. Taking advantage of the geometry, only a quarter portion of the specimen geometry was considered as shown in Figure 38. The computational space was divided into eight node quadrilaterals. There were 40 elements with 147 nodal points. Solutions were carried out for the first 10  $\mu$ s.

Using the "RESTART" facility provided by MAGNA, the solutions were obtained through several computer runs. The solution was stable and convergence was achieved with a maximum of fifteen iterations. The full Newton-Raphson method was used to calculate the stiffness matrix. This means that the global stiffness matrix was updated at each equilibrium iteration. The convergence tolerance were through displacements and nodal forces. Stringent tolerance limits were specified for each run to obtain stable solution with the increasing applied displacement.

The results for the first few loading steps showed that the entire specimen experienced only elastic deformations. The longitudinal elastic stress reached maximum values at the notch

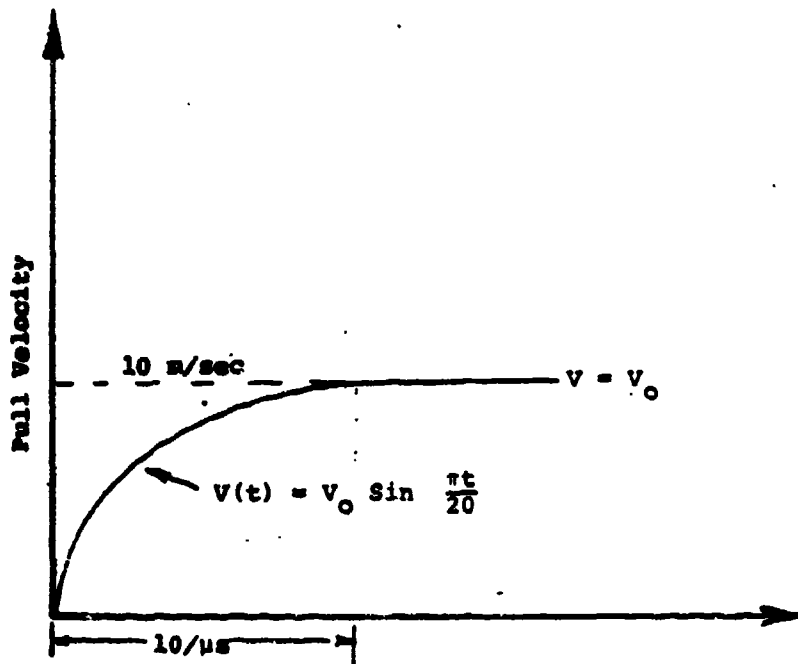


Figure 37. Velocity - Time Input Condition.

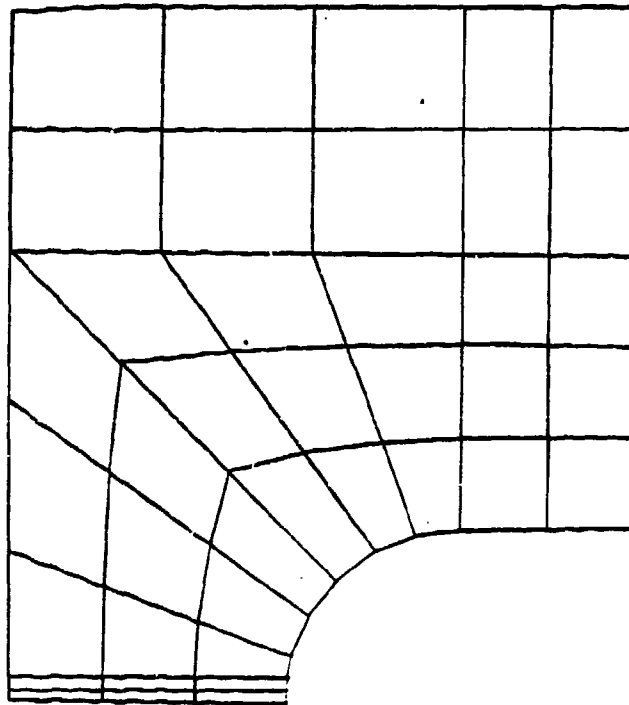


Figure 38. Coarse Mesh Pattern for the Notched Tensile Specimen. One quarter portion of the axi-symmetrix geometry. (Nodes: 147; Elements: 40)



surface while the values were minimum at the axis. These results, as shown qualitatively in Figure 39 are in agreement with the rigorous solution obtained by Neuber<sup>(7)</sup> for the elastic case. On subsequent loading steps, the stress maximum at the notch surface started shifting towards the axis. At this early stage of the loading history, the minimum cross section of the specimen had already plastically deformed. At later time steps, the entire notched portion of the specimen undergoes plastic deformation. The effective plastic strain was greatest near the notch surface and least at the axis, as shown in Figure 40. Both static and dynamic analyses predicted qualitatively similar variations of stress and effective plastic strain at the minimum cross section of the notch. The mean and longitudinal stress maxima were just inside the notch surface, and shifted inward slightly as the load was increased. At the end of 5 or 6 microseconds, the cross section area of the notch root section reduced by 4 to 5 percent.

Bridgeman<sup>(6)</sup> hypothesized that the effective plastic strain is constant across the minimum section and that the stress maximum would occur at the axis and the minimum at the surface. To compare the present numerical simulation with the approximate analytical results of Bridgeman, and also with the results reported by Norris et al.<sup>(8)</sup>, Curran et al.<sup>(11)</sup>, and Chen<sup>(12)</sup>, the present solution should be carried out beyond 50 percent reduction of the area of the notch (or neck).

Since the plastic strain was greatest near the notch surface, failure initiation (in terms of void nucleation and growth) should possibly occur there. This is consistent with the results reported by Curran<sup>(11)</sup> that the failure initiates near the notch surface; whereas, Norris et al.<sup>(8)</sup>, predict failure initiation on the axis.

It is interesting to note that the trend of the present solution appears to be consistent with the result reported by

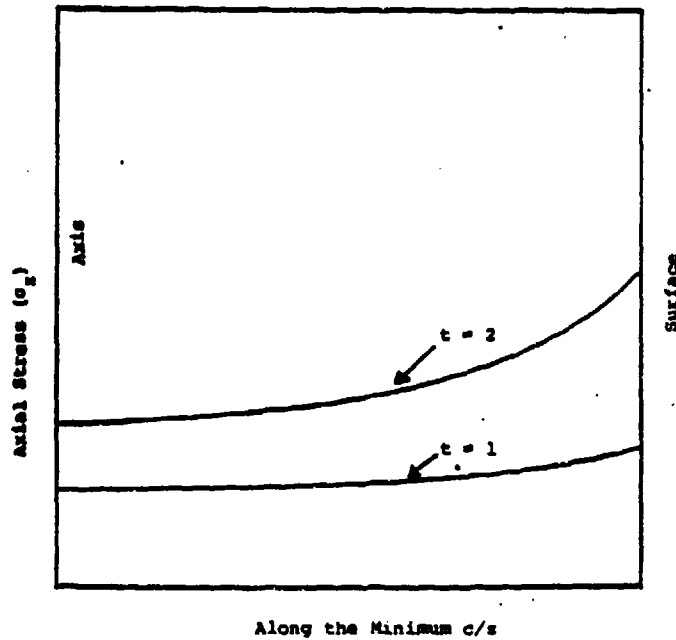


Figure 39. Variation of Axial Stress Along the Radius of Notch Minimum Cross Section for Initial Time Steps.

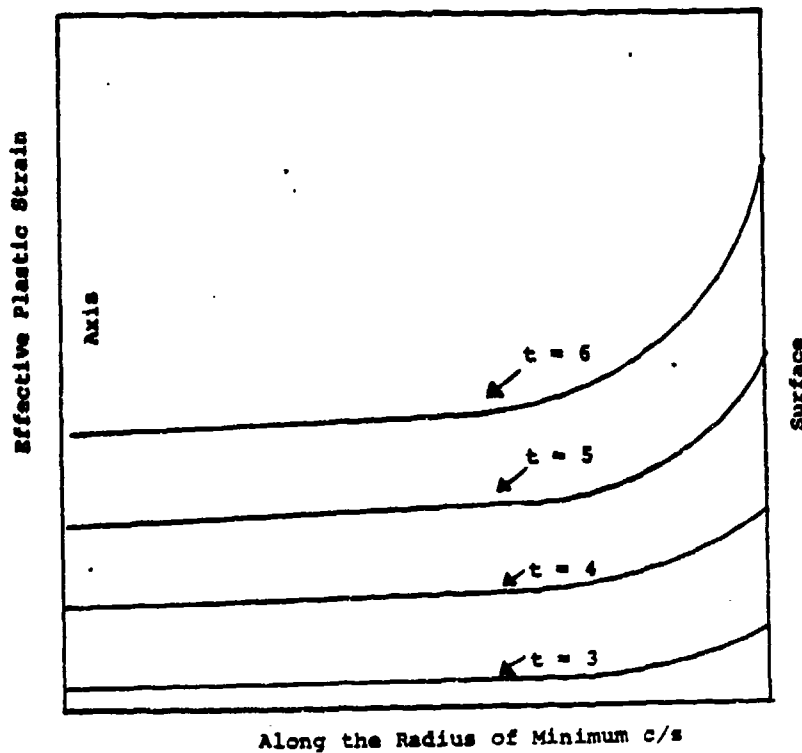


Figure 40. Variation of Effective Plastic Strain Along Minimum Cross Section at Various Time Steps.

Chen<sup>(12)</sup>. Chen carried out the numerical solutions for large plastic strains and continued his calculation to  $a/a_0 = 0.467$ . His calculations also showed that the peak mean stress occurred between the axis and the notch surface.

The coarse analysis could not be continued beyond eight loading steps because of the coarse finite element grid. When the plastic strains increase significantly, the stresses near the notch showed instabilities after few solution steps, and the solutions developed unphysical features.

In order to overcome solution instabilities, an improved mesh pattern was developed. The number of 4-node quadrilateral elements was increased by several orders of magnitude. Finer elements are used near the notch surface, as shown in Figure 41. Solutions were repeated with the new mesh, and the preliminary results show smooth variation of stresses from the axis to the surface, as shown in Figure 42a. The variation of longitudinal strain from the axis to the surface is shown in Figure 42b. The maximum plastic strain at this stage of the deformation was around 30 percent.

The Bridgeman analysis is expected to be valid for large and widespread plastic deformation in the specimen. Values of  $\sigma_m/\sigma_{eff}$  and the equivalent plastic strains along the minimum cross section of the notch were calculated and compared in Figure 43. It can be seen from these figures that the results do not compare well. The plastic strain is not uniform, but instead increases toward the surface, and the mean stress maximum does not occur on axis. Therefore, we conclude that in order to use Bridgeman analysis, the plastic strains must be significantly higher than these values.

It is important to further strengthen the numerical solution procedure so that the stress states for the entire test duration are accurately computed. The solutions have to be

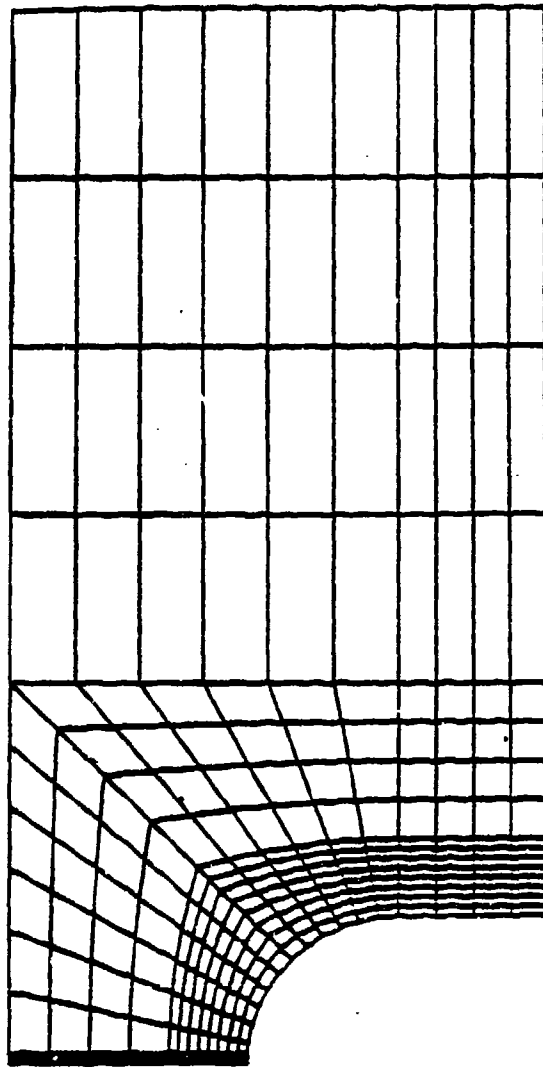


Figure 41. Improved Finite Element Mesh. (Nodes: 291; Elements: 256).

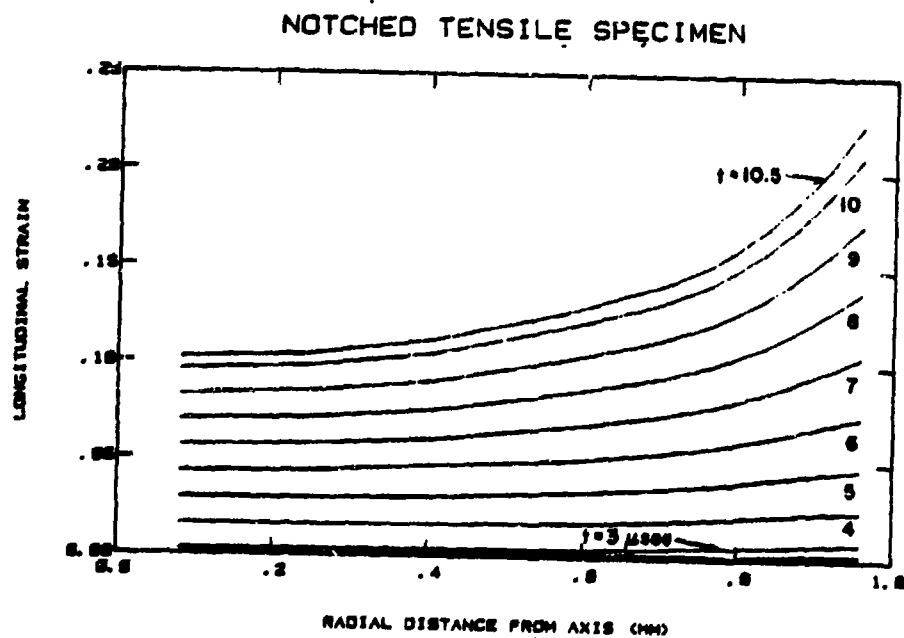
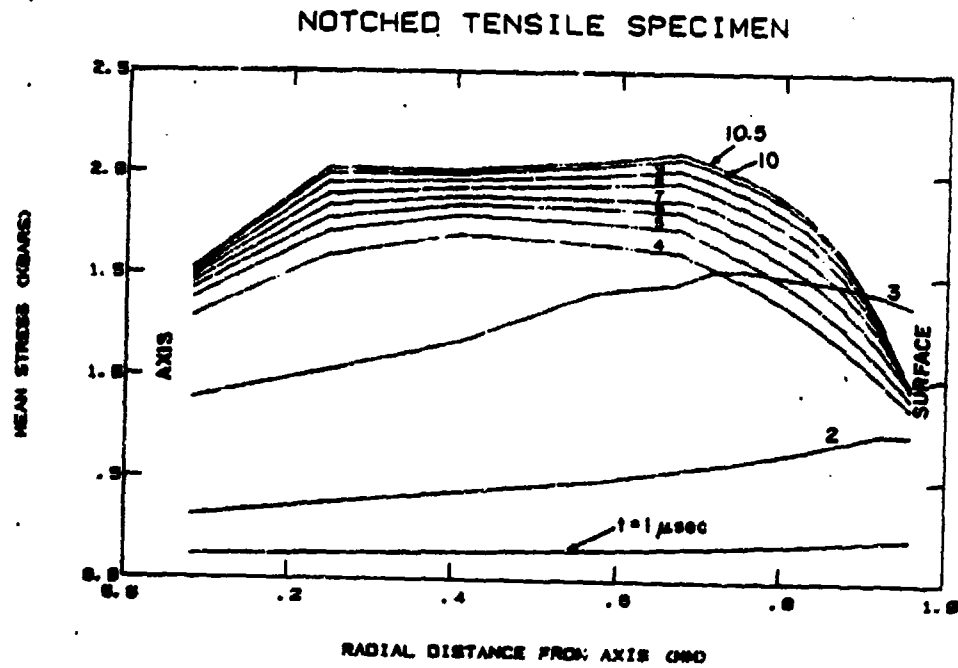
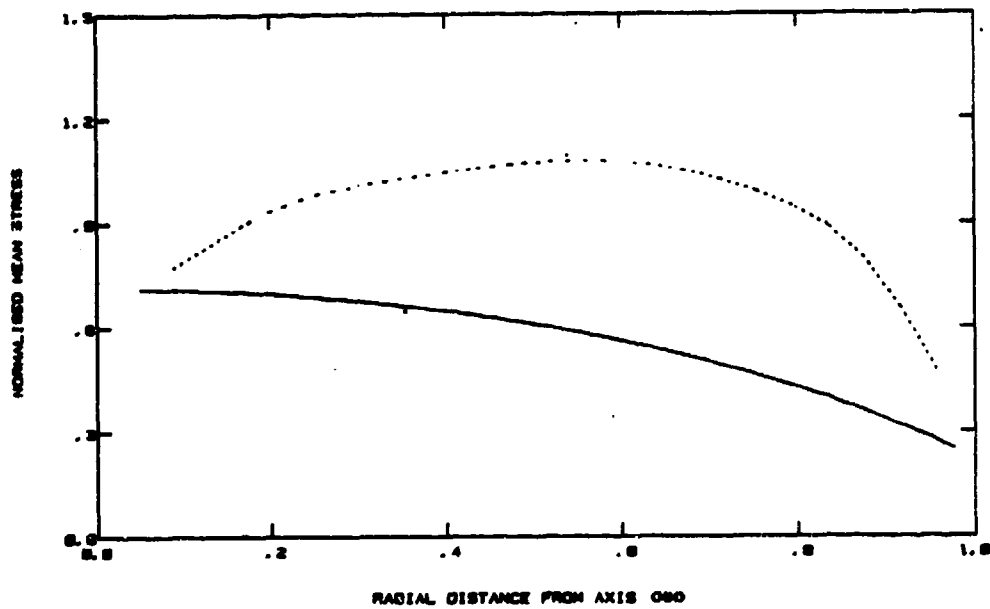
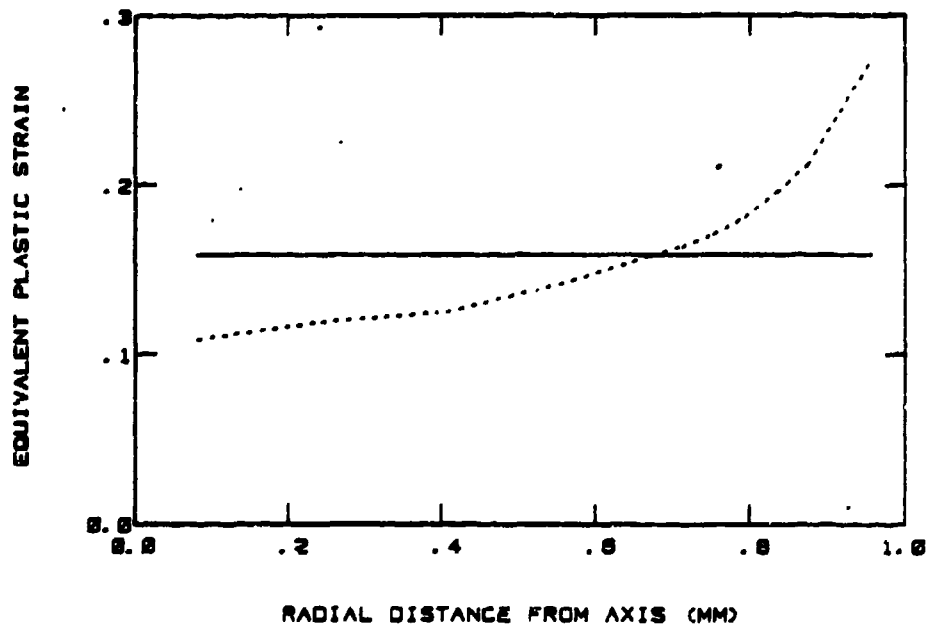


Figure 42. Results Obtained with Mesh Shown in Figure 41 for Minimum Cross Section. (a)  $\sigma_m$  (b) Plastic strain. Note: Finite element data obtained at integration points have not been smoothed.

# NOTCHED TENSILE SPECIMEN.



(a)



(b)

Figure 43. Comparison of MAGNA Prediction (dotted line) and Bridgeman Analysis (solid line) for Minimum Cross Section at 10.5  $\mu$ s. (a)  $\sigma_m/\sigma_{eff}$ , (b) Plastic Strain.

carried up to ultimate failure, in order to evaluate the constitutive models for damaged material. The accuracy of computations should be evaluated by comparison with measured average uniform axial stress and displacements, as well as detailed analysis of predicted and measured notch contours.

c. Experimental Investigation of Necking

Experiments were conducted in which the behavior of copper and steel specimens after load maximum was quantitatively observed. Results are preliminary, but very encouraging.

1. Experimental Techniques. A back-lit photographic system was developed to photograph (split) Hopkinson Bar (SHB) specimens during tensile tests. A 35 mm drum camera was used to record 160 images at approximately unity magnification. The light source was a small LED, driven at 50 kHz, with a pulse duration of 0.15  $\mu$ s. Pulses were generated by a Hewlett-Packard 8011B pulse generator. The pulse generator was initiated by contact of the striker bar on the driver bar. The trigger pulses to the LED were inductively coupled to one of the strain gauges, so that the time of each exposure could be precisely correlated with the strain gauge records. The recording medium was Kodak RAR 2749 pushed by developing for eight minutes at 85°F in D-19. Figures 44 and 45 show sample silhouettes of an OFHC copper and steel specimens just prior to rupture.

Three experiments each were conducted with OFHC copper and 1020 steel. Strain was computed from the specimen diameter using equation (13). Figures 46 and 47 show the excellent correlation between strain computed from equations (13) and (8). In those figures, strain is normalized to the start of the tensile pulses.

The data revealed that many specimens experience a compressive strain prior to the arrival of the tensile pulse.

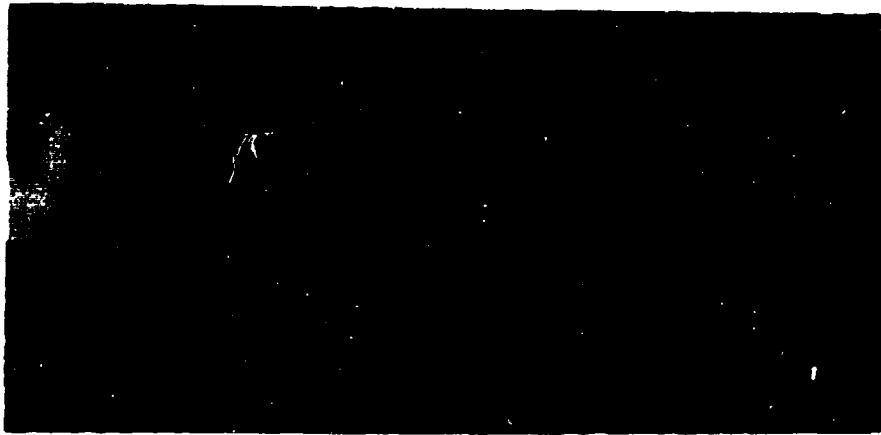


Figure 44. OFHC Copper Specimen Just Prior to Rupture.



Figure 45. 1020 Steel Specimen Just Prior to Rupture.



For 1020 steel specimens, the prestrain in the three tests was 0.015, 0.012, and 0.009. The measurement accuracy was about 20 percent. The prestrain in OFHC copper specimens was less than could be resolved.

Another key feature of the photographic technique is that it provides a measure of the radius of curvature of the necked sample profile. These data may be used to calculate the triaxial stress state in the specimen using Bridgeman's approximation, as described below.

ii. Results. No appreciable necking occurred in steel specimens during the principal tensile cycle, resulting in, the good agreement between the two strain curves in Figure 46. Necking does occur early in the copper specimens. Thus, in Figure 47, the strains correlate only to about 200  $\mu$ s. After this time, comparisons are no longer meaningful because the photographically determined strain is the local value in the necked region, while the SHB data are average values for the uniform cross section. The additional uniform strain after localized necking occurs confirms the results of Hutchinson and Neal<sup>(13)</sup> that significant post elongation strain occurs in strain rate sensitive materials (such as OFHC copper).

The three copper specimens were labeled 16, 17, and 18. Data from the bar strain gauges were only obtained from tests 16 and 18. For tests 16 and 18, the bar gauge records were used to compute average strain and  $\sigma_{eng}$  as functions of time. The results are shown in Figure 48.

The sequential picture frames were numbered. The reference marks on the strain gage records were used to bring the photographs into register with the strain gauge time scale. The frame number corresponding to onset of the tensile pulse was found to be 49 in both tests 16 and 18.

The photographs were analyzed to determine both  $\epsilon$  and  $R$  at the waist of the neck. Usually four independent

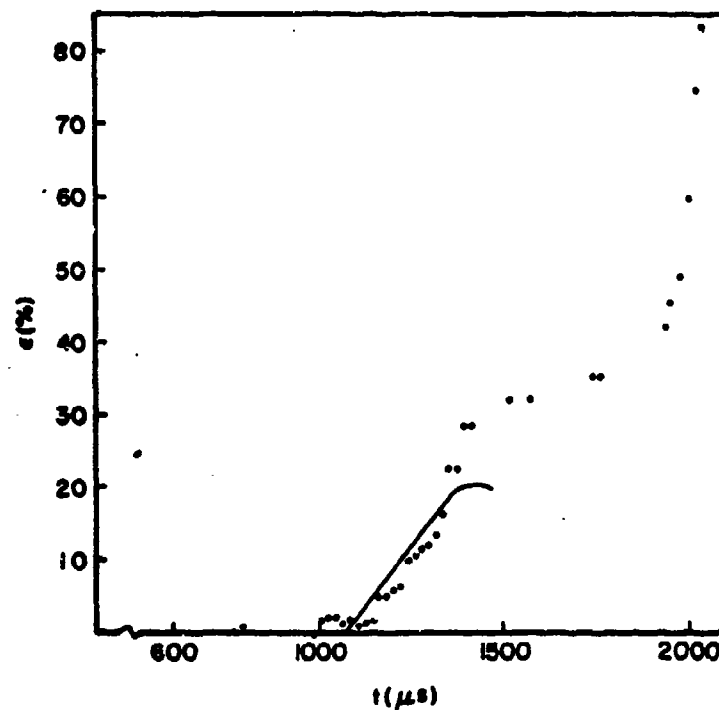


Figure 46. Comparison of Strains Computed from SHB Gauges (Line) and Photographs (Points) for 1020 Steel Specimen.

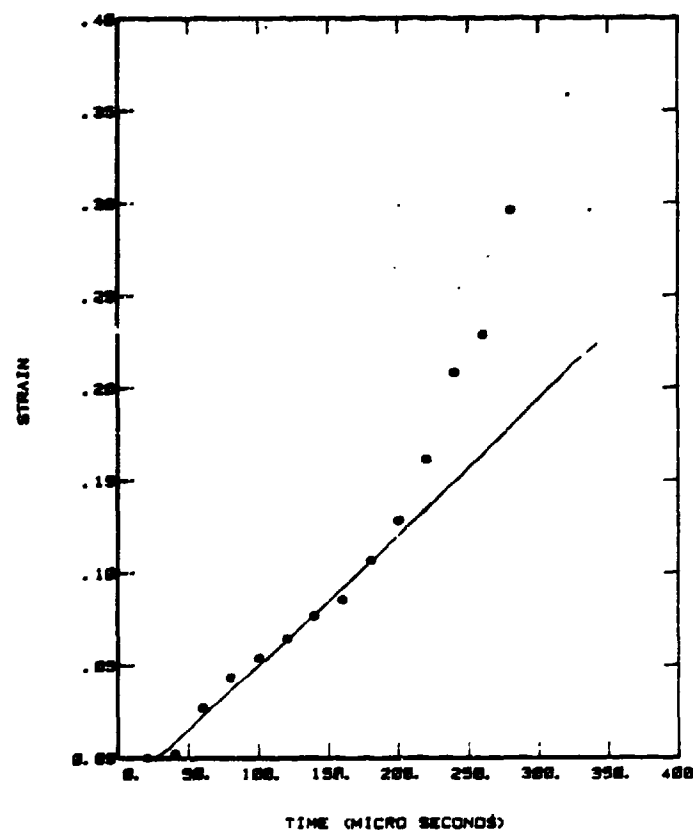


Figure 47. Comparison of Strains Computed from SHB Gauges (Line) and Photographs (Points) for OFHC Copper Specimen.

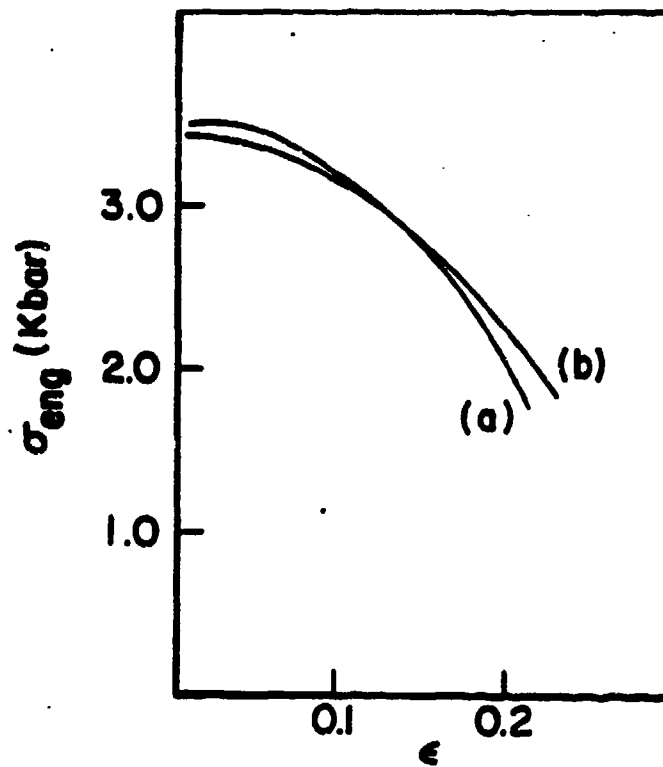


Figure 48. Engineering Stress vs. Strain, OFHC Copper, Tests (a) 16 and (b) 18.

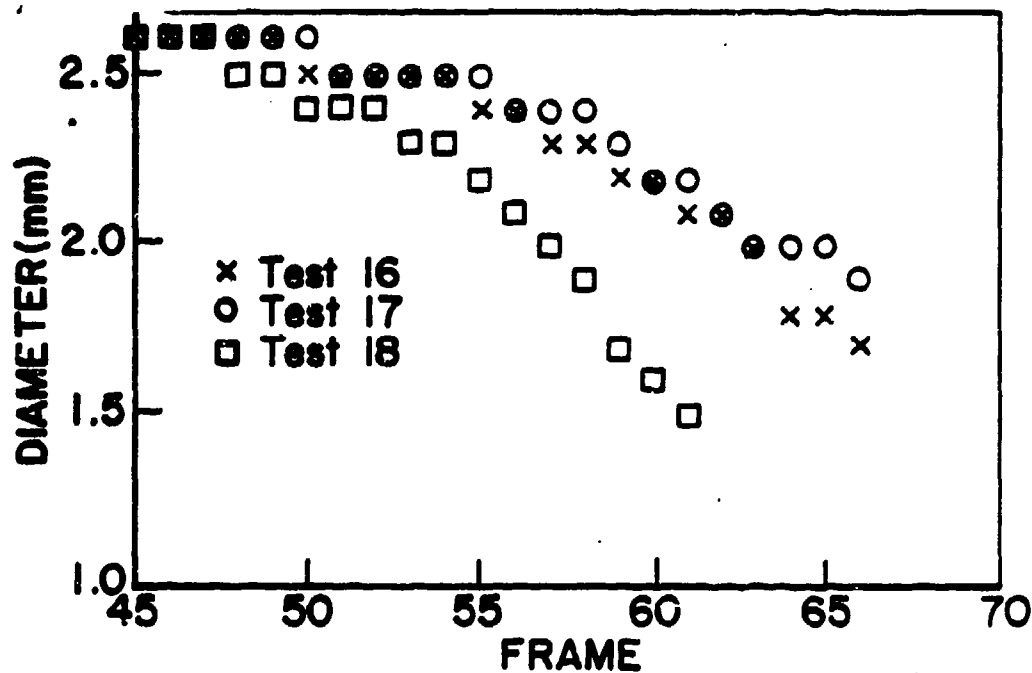


Figure 49. Variation of Diameter With Frame Number (Each Frame is 20  $\mu$ s).

measurements were made of each frame using the two sides of the sample, and the original film negative and an enlarged print. The radius of curvature was estimated by overlaying various radii circles on the neck silhouette. The results of these measurements are displayed in Figures 49 and 50.

The strain gauge data and neck shape parameters were used to compute  $\sigma_{eff}$ , using equations (11), (12), and (13). The results are shown in Figure 51.

The  $(\sigma_{eff}, \epsilon)$  curves from tests 16 and 18 appear quite different, even though the  $(\sigma_{eng}, \epsilon)$  curves are similar. Several possible reasons for the variation in effective stress behavior were examined.

The local strain rate was significantly higher in test 18 than in test 16 or 17. In test 18, the maximum value of  $\dot{\epsilon}$  during the first tensile cycle was  $6 \times 10^3 \text{ s}^{-1}$ , whereas in tests 16 and 17,  $\dot{\epsilon}_{max}$  was only  $3 \times 10^3 \text{ s}^{-1}$ .

The difference in the  $\sigma_{eff}(t)$  data in these tests is traceable to differences in the shapes of the necked regions. In order to clarify the relationship between  $\sigma_{eff}$  and neck shape, Figure 52 was prepared. It is clear that in test 18 the diameter began decreasing at a faster rate and at an earlier time, and ended up at a smaller value. However, the radius of curvature as a function of diameter did not vary significantly from test to test. However,  $b$  (equation 13) is much more sensitive to  $a$  than  $R$ . Thus, it appears that the necking instability initiated sooner in test 18, causing test 18 to achieve a higher strain rate.

Synchronization errors were considered. It was found that no plausible synchronization error could significantly alter the discrepancies in  $\sigma_{eff}(t)$  between tests 18 and 16.

The tentative conclusion that has been reached is that the  $(\sigma_{eff}, \epsilon)$  curves from tests 16 and 18 are both correct.

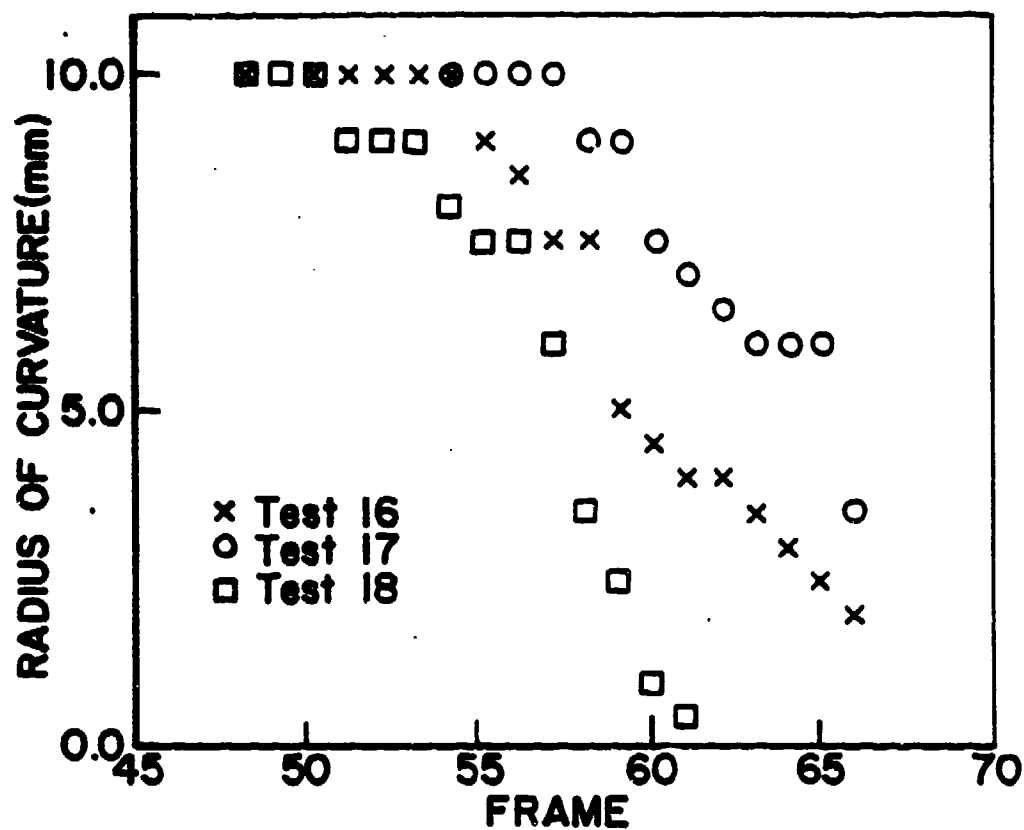


Figure 50. Variation of Radius of Curvature With Frame Number.

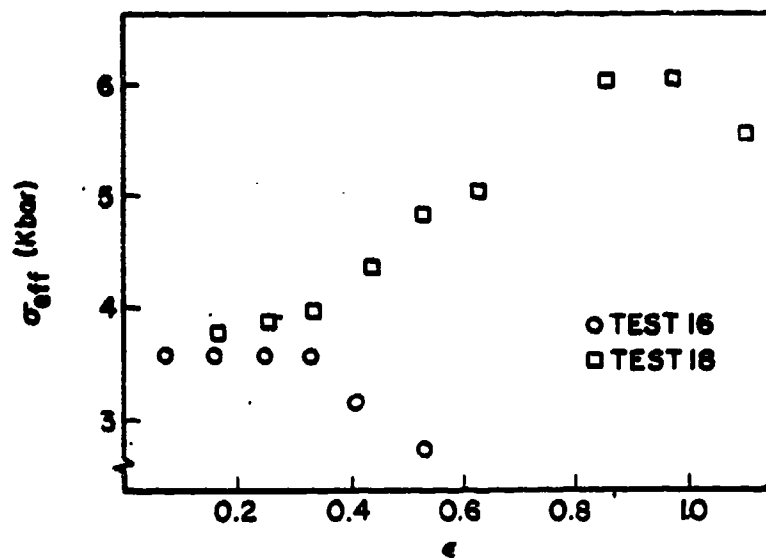


Figure 51. Effective Stress vs. Strain For Necked OFHC Copper Specimens.

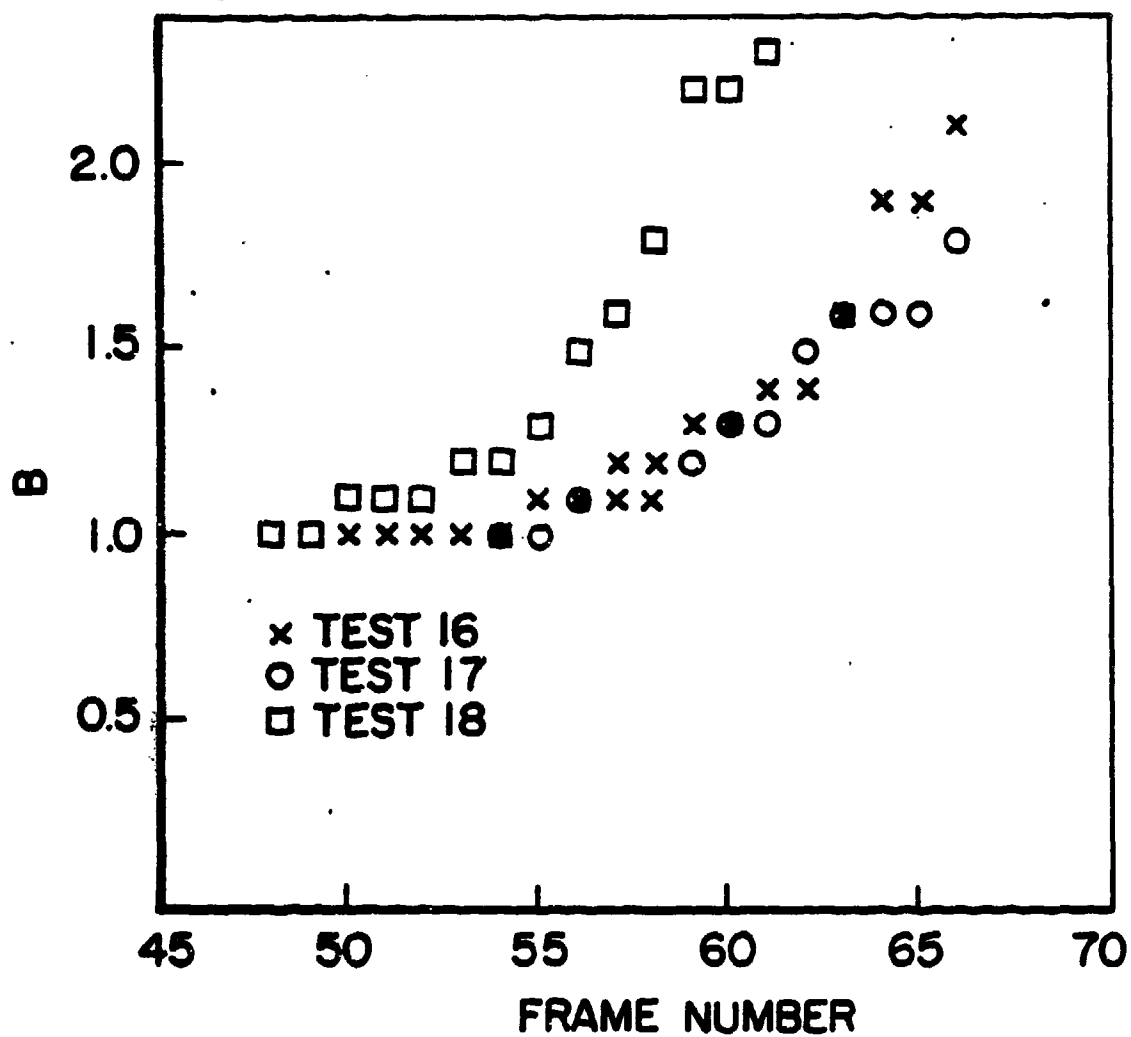


Figure 52. Variation With Time of Bridgeman Factor,  $B$ , in Tests 16, 17, and 18.

They represent the behavior of copper under very high strain rates and high values of  $|\sigma_m/\sigma_{eff}|$ . The differences between the data from the two tests are due chiefly to the differences in strain rate.

#### 4. TEST ON WAAM COPPER LINERS

Seven types of WAAM warhead liners were tested using the split Hopkinson bar apparatus. The liners were labeled as C22, C3A, F7A, M36, F15, M13A, and ORBITAL FORGED. The A suffix indicates that the warhead liners had been annealed. The thinness of the warhead liners dictated that only compression specimens could be machined and tested. The dimensions of the compressive specimens were 2.54 mm thick and 6.36 mm in diameter. Vacuum grease lubrication was applied to the specimens and bar ends to reduce the transverse shear stress caused by friction between the specimen and bar ends.

In order to aid interpretation of compressive tests results, tests were also run with annealed OFHC copper and 6061-T6 aluminum. Compression and tensile data were compared. Agreement was excellent for hard materials (Table V and Figure 53). However, for annealed materials, the flow stresses only agreed after considerable strain (Figure 54).

Room temperature tests on the WAAM materials were conducted with a striker bar velocity of 6.35 m/s. This launch velocity resulted in a strain rate of 1,000 to 1,450  $s^{-1}$  for all specimens except for those from the C22 material, which had strain rates of 400  $sec^{-1}$ . The results of these tests in terms of test number, material type, strain rate (at 10 percent strain), maximum true stress and maximum true strain are shown in Table VI. The true stress-strain curves are shown in Figures 55 through 61. Each figure contains data collected for the same warhead liner. Specimens from the annealed warhead liners show significant work hardening, lower ultimate stresses, greater

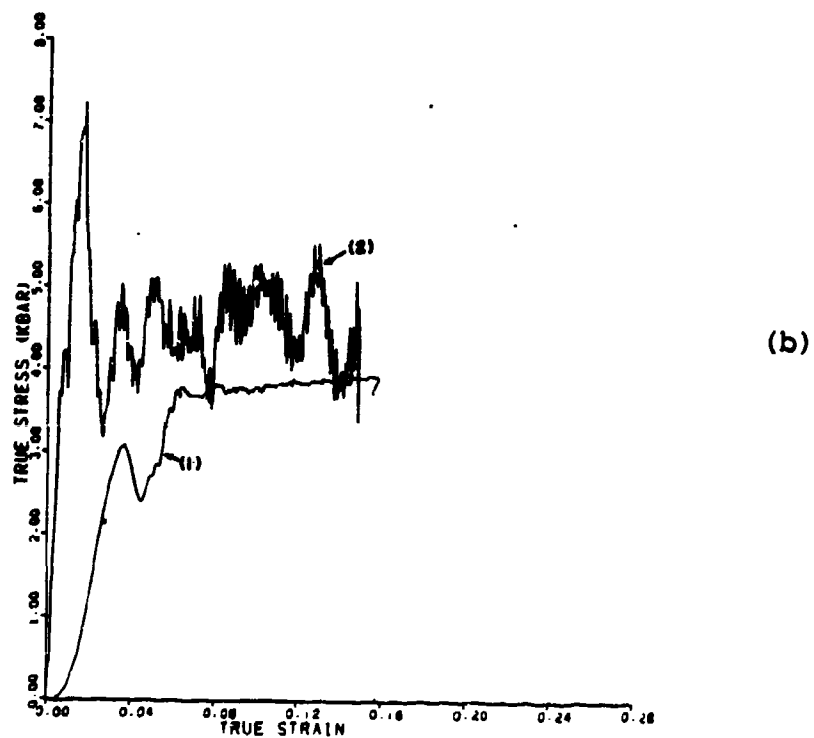
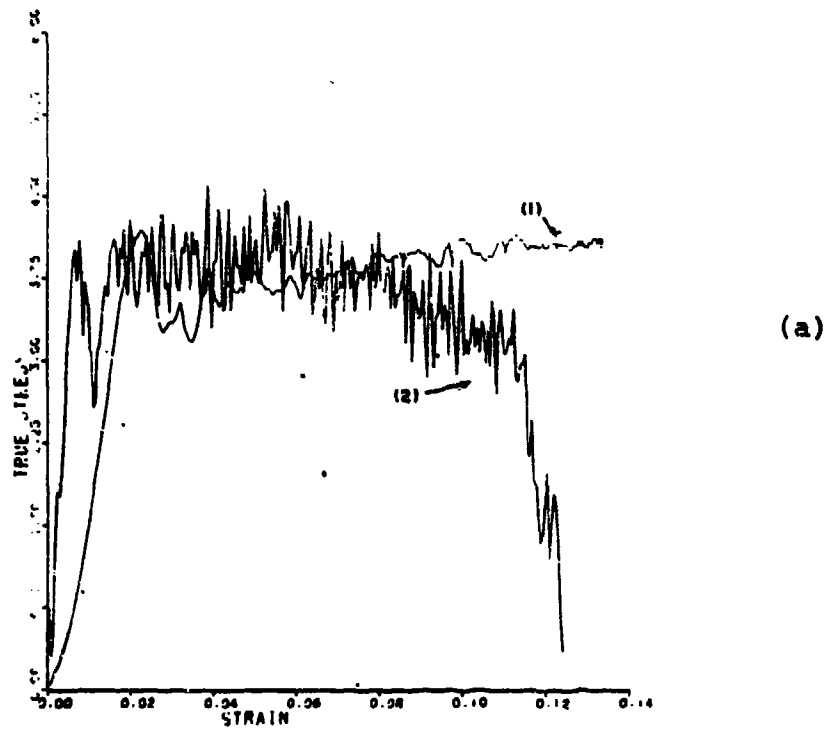


Figure 53. Comparison of Compression (1) and Tension (2) Stress Strain Curves for Hard Materials (a) 6061-T6 Aluminum, (b) Half Hard OFHC Copper.



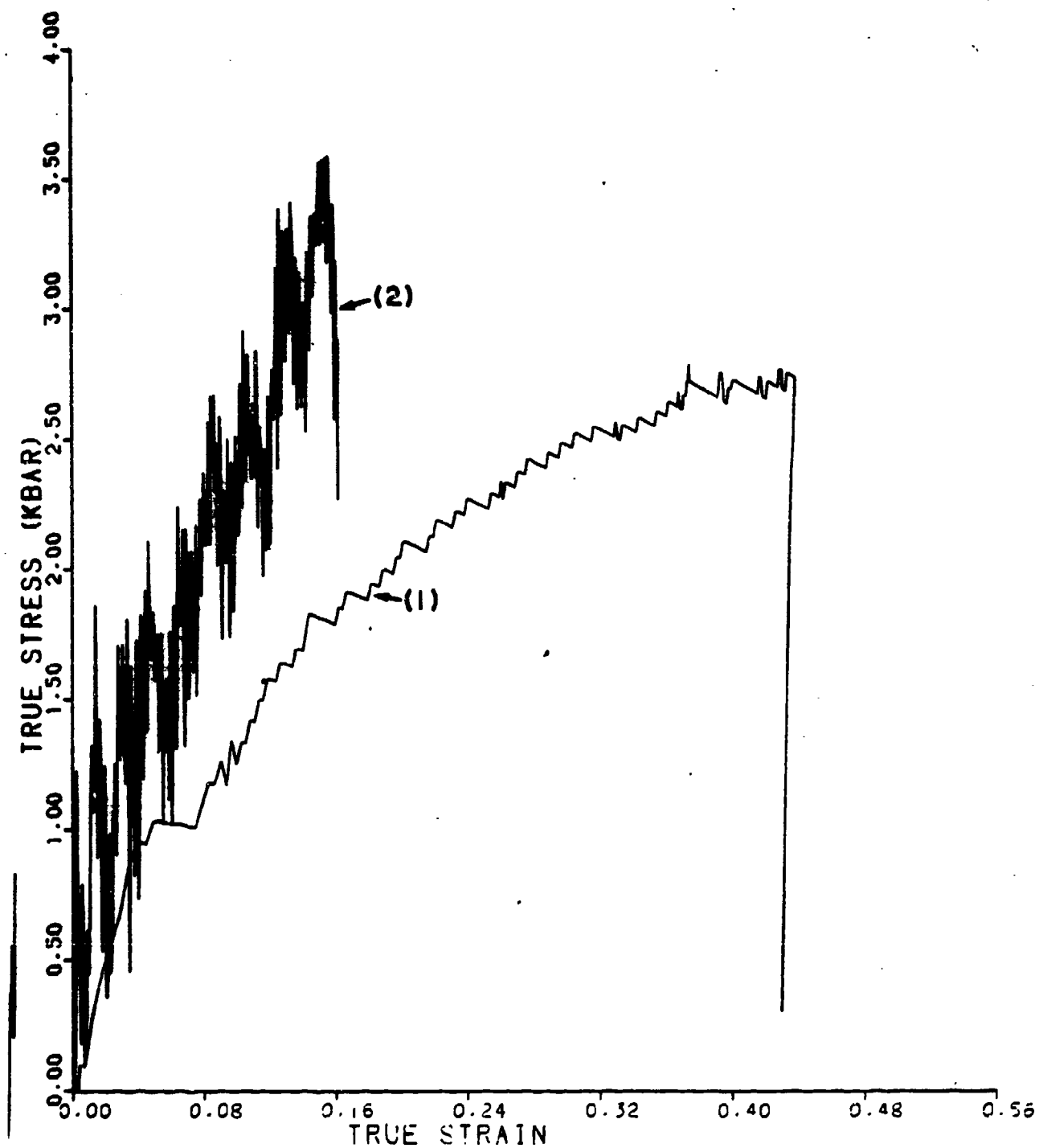


Figure 54. Engineering Stress-Strain Behavior of Fully Annealed OFHC Copper, (1) Compression (2) Tension.

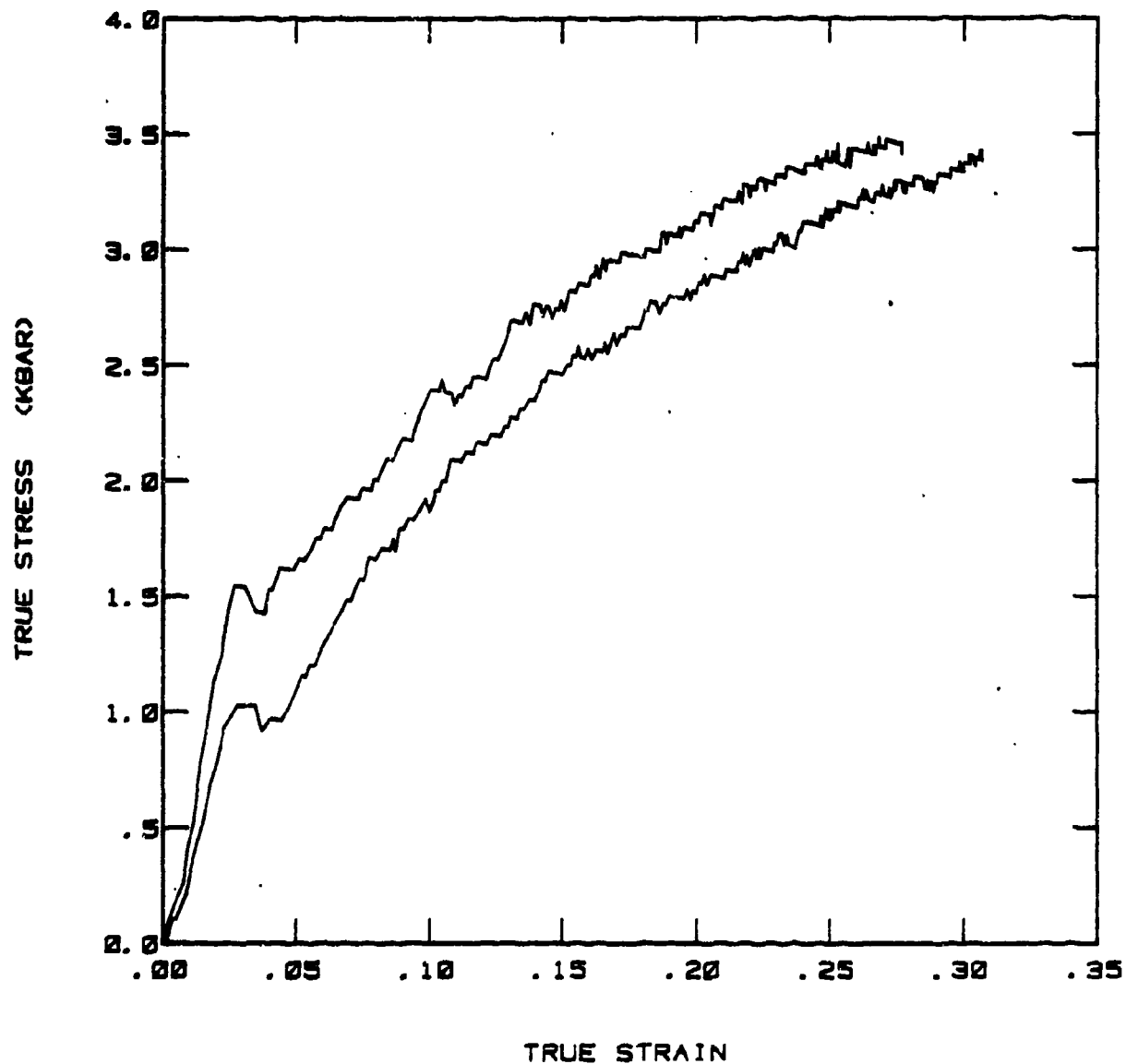


Figure 55. Stress-Strain Curves From Hopkinson Bar Analysis of Room Temperature Tests of the ORBITAL FORGED WAAM Warhead Liner.

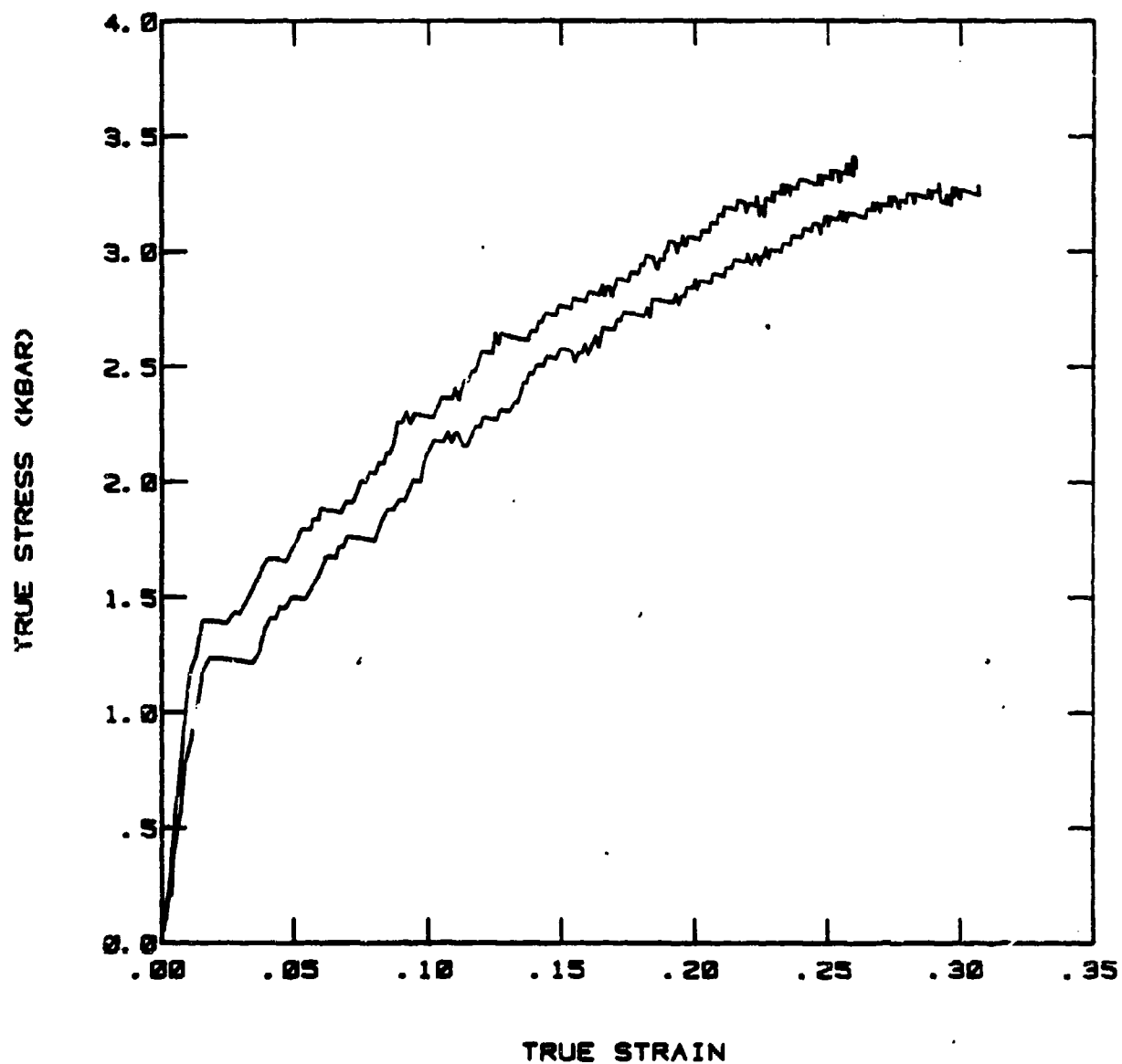


Figure 56. Stress-Strain Curves From Hopkinson Bar Analysis of Room Temperature Tests of the F7A WAAM Warhead Liner.

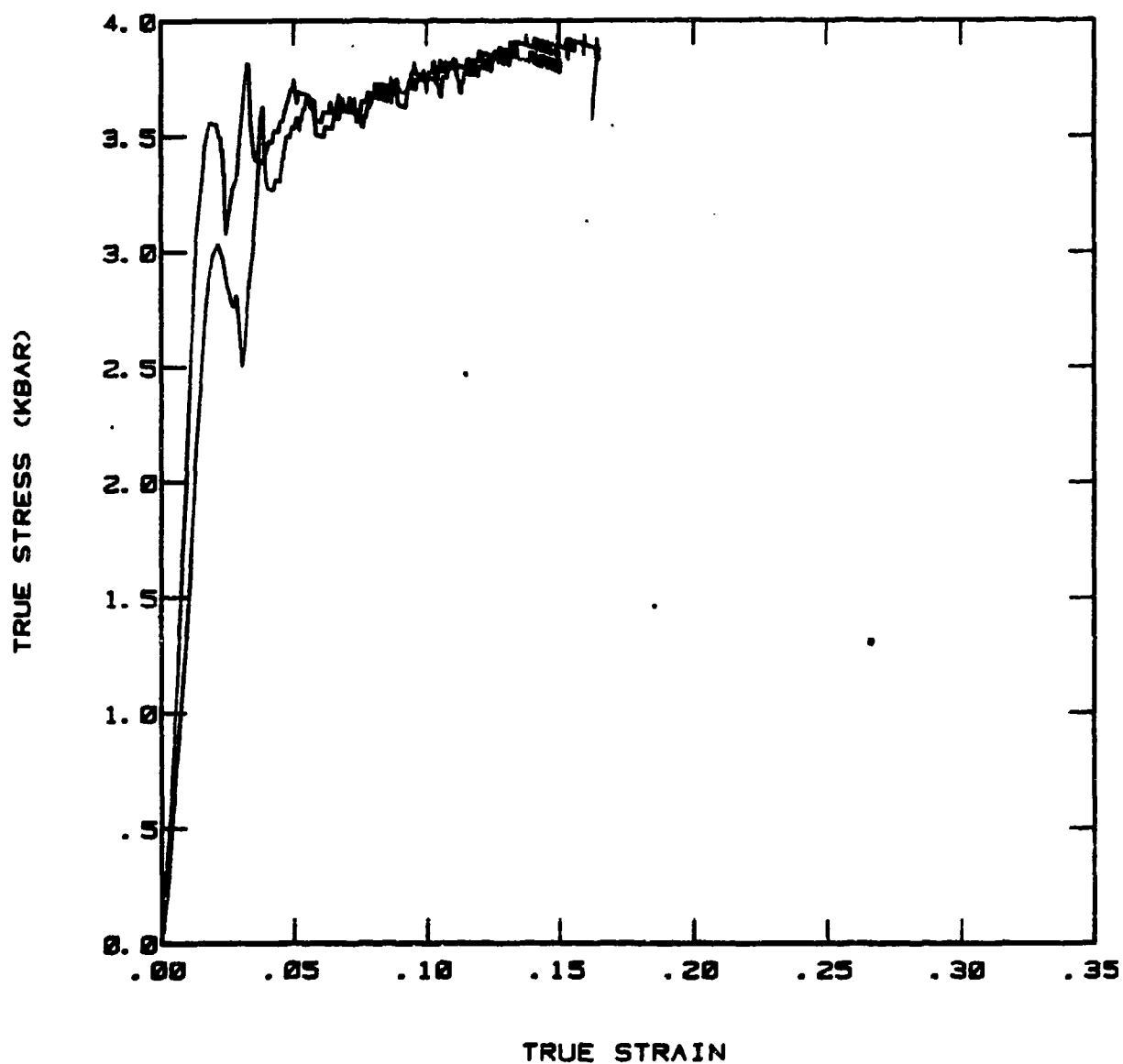


Figure 57. Stress-Strain Curves From Hopkinson Bar Analysis of Room Temperature Tests of the C22 WAAM Warhead Liner.

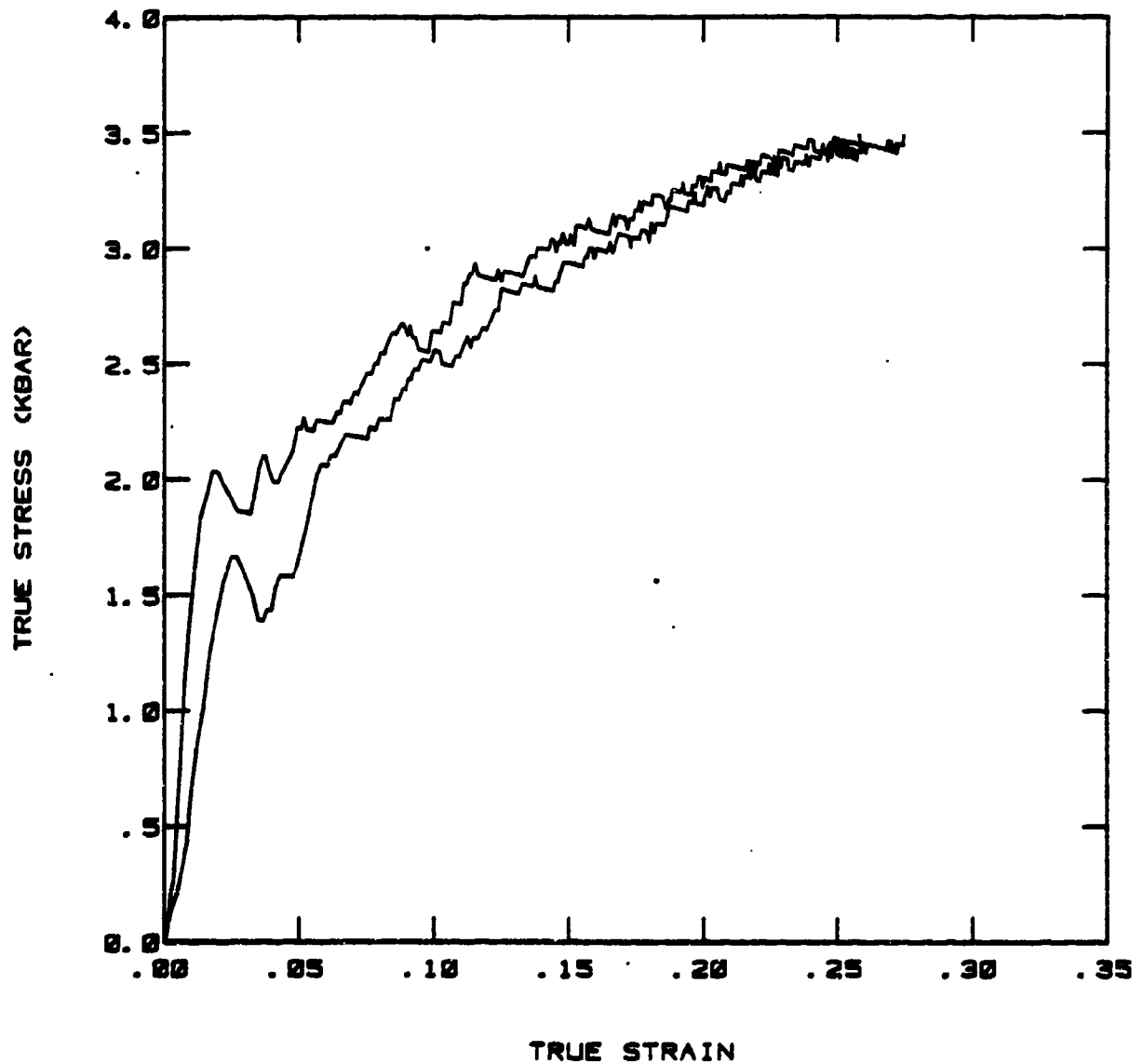


Figure 58. Stress-Strain Curves From Hopkinson Bar Analysis of Room Temperature Tests of the F15 WAAM Warhead Liner.

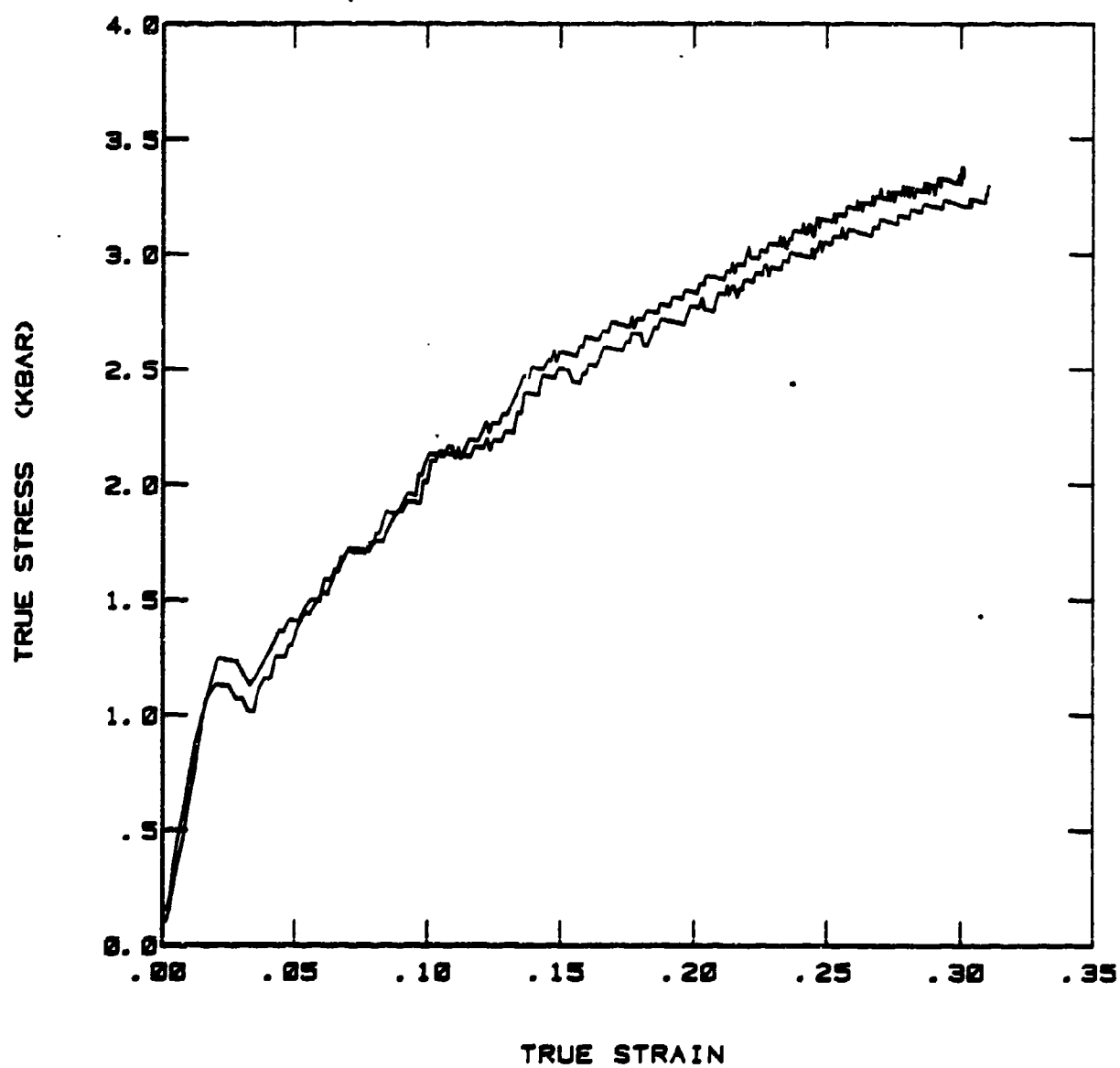


Figure 59. Stress-Strain Curves From Hopkinson Bar Analysis of Room Temperature Tests of the C3A WAAM Warhead Liner.

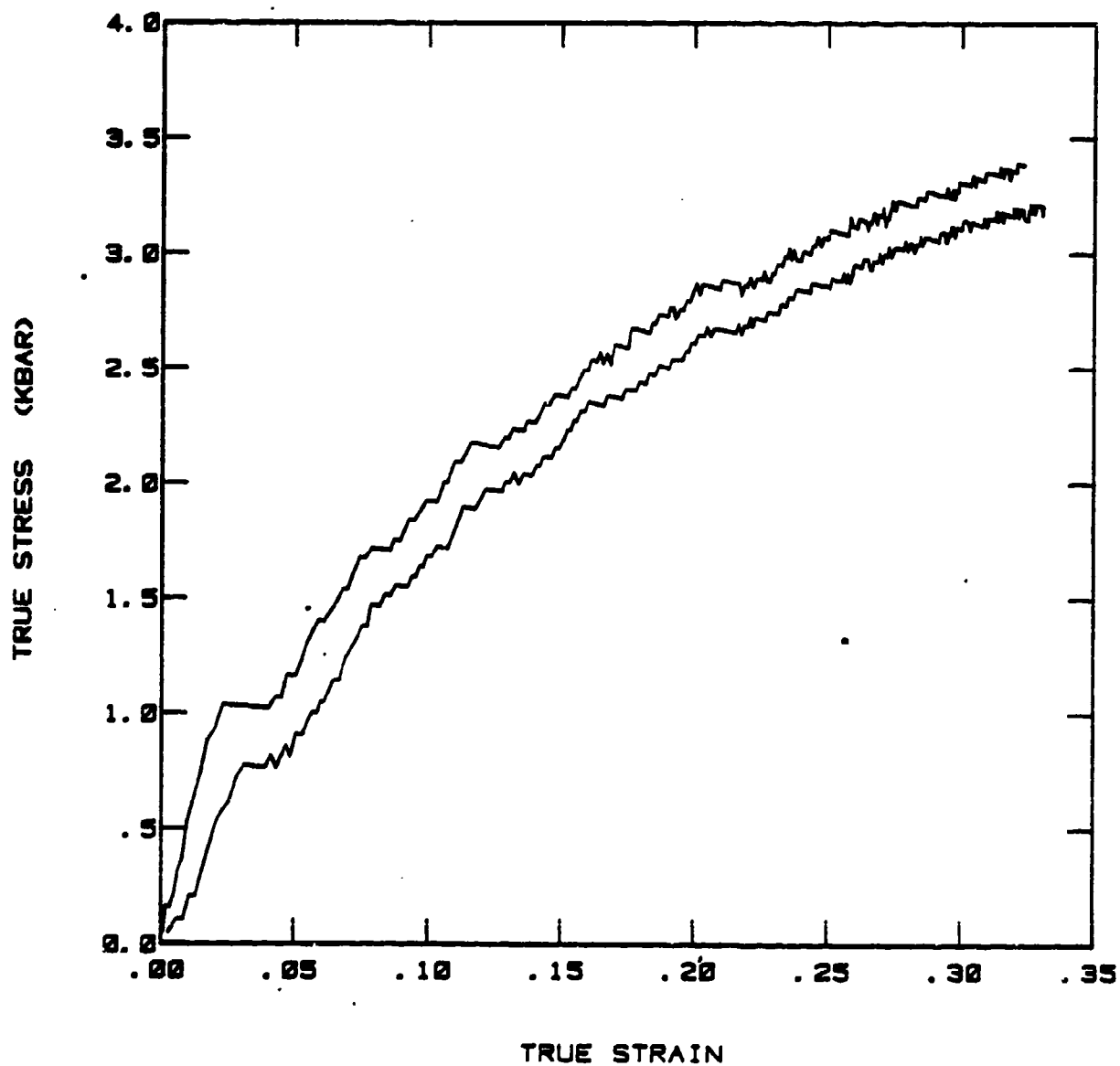


Figure 60. Stress-Strain Curves From Hopkinson Bar Analysis of Room Temperature Tests of the M13A WAAM Warhead Liner.

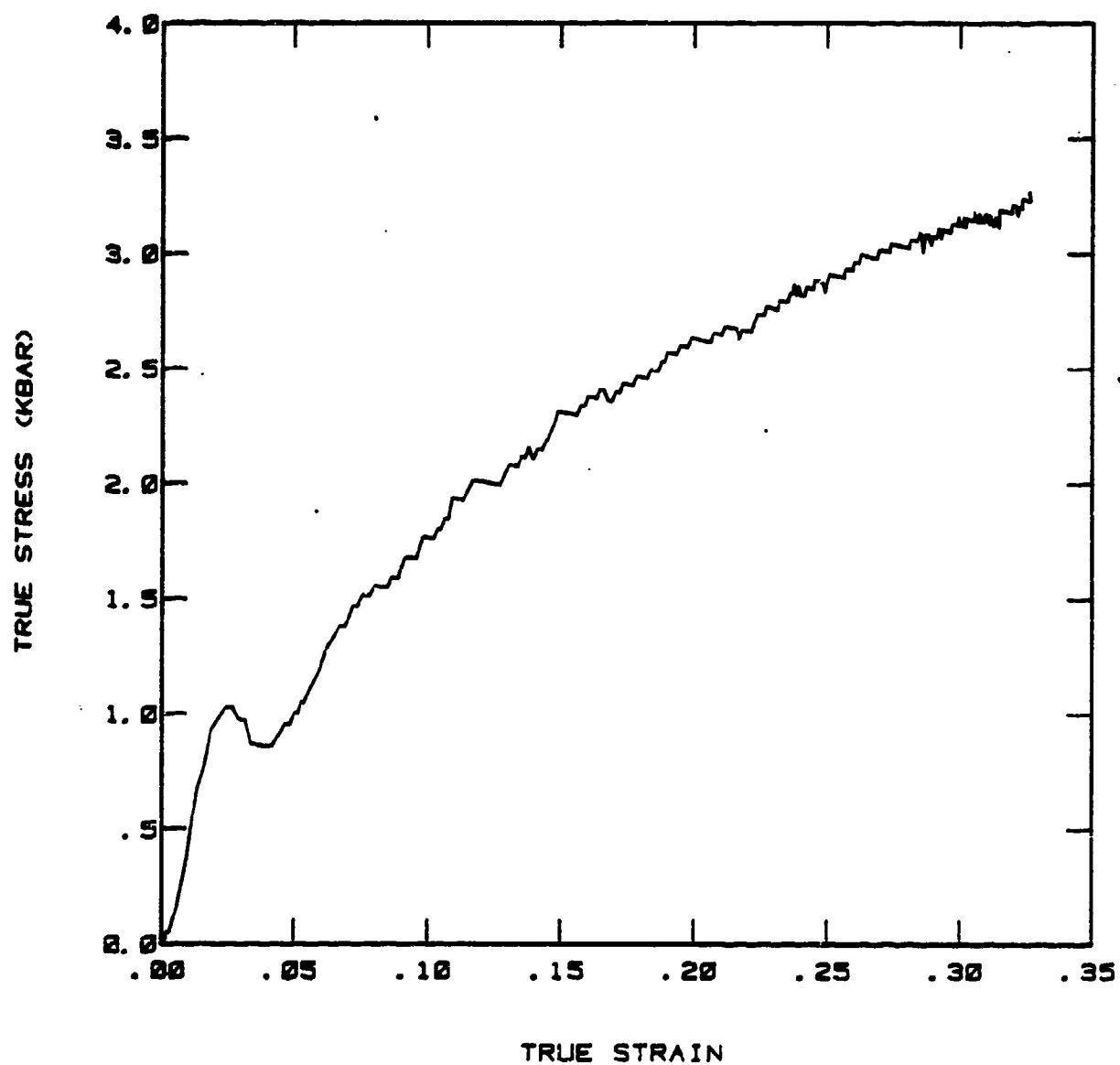


Figure 61. Stress-Strain Curves From Hopkinson Bar Analysis of Room Temperature Tests of the M36 WAAM Warhead Liner.



TABLE V  
SUMMARY OF 6061-T6 TENSION AND COMPRESSION TESTS

Test Number	Type Of Test	Strain Rate At 5% Strain	Maximum True Stress (Kbar)
HB-131	Tension	380	3.68
HB-132	Tension	390	3.68
HB-133	Tension	230	3.70
HB-134	Tension	220	3.70
HB-135	Tension	530	3.72
HB-136	Tension	540	3.84
HB-139	Compression	700	3.80
HB-140	Compression	400	4.05
STA-1	Tension	STATIC	3.48
STA-2	Tension	STATIC	3.46
STA-3	Tension	STATIC	3.51

TABLE VI  
SUMMARY OF ROOM TEMPERATURE WAAM WARHEAD  
LINER COMPRESSION TESTS

Test Number	Material Type	Strain Rate @ 10% Strain	Maximum True Stress (Kbar)	Maximum True Strain (%)
HB-118	C22	380	3.88	15.0
HB-119	C22	410	3.86	16.6
HB-120	C3A	1320	3.25	31.1
BH-121	C3A	1340	3.32	30.0
HB-122	F7A	1120	3.38	25.9
HB-123	F7A	1320	3.26	30.8
HB-124	M36	1830	3.20	33.0
HB-125	F15	1020	3.45	25.8
HB-126	F15	1100	3.42	27.7
HB-127	M13A	1460	3.35	32.0
HB-128	M13A	1420	3.18	35.0
HB-129	Orbital Forged	1340	3.38	30.8
HB-130	Orbital Forged	1150	3.44	27.7

ductility and higher strain rates than the nonannealed specimens. Figure 62 illustrates these differences by comparing the stress-strain curve from a C22 warhead specimen to that of a C3A warhead specimen.

## 5. RESULTS OF HOPKINSON BAR TESTS FOR OTHER MATERIALS

During the period since our last report<sup>(1)</sup>, additional tensile test data have been obtained for 1020 steel and OFHC copper. Those results are presented here, along with the previous data for completeness. Reference 1 also reports data for 2024-T4 aluminum, 3003 aluminum, 1100 aluminum, and nickel 200.

### a. 1020 Mild Steel

The 1020 steel samples were machined at the University and were tested in tension at strain rates ranging from 350 to 1,000  $s^{-1}$ . A typical true stress-true strain plot from the unfiltered Hopkinson bar data is presented in Figure 63. The stress-strain plots, for the various strain rates tested, were smoothed and are presented in Figure 64. The "overshoot" often observed in mild steel at the beginning of the stress-strain curve (Reference 4) could not be distinguished from the digital stress-strain plots, possibly because of the superimposed oscillations at the beginning of the signal attributed to the wave propagation mechanism in a long bar.

### b. OFHC Copper

Additional tests on OFHC Copper, partially and fully annealed, were carried out in compression and tension. Those results are summarized in Figure 54. The fully annealed specimens were maintained at 1,000°F for two hours.

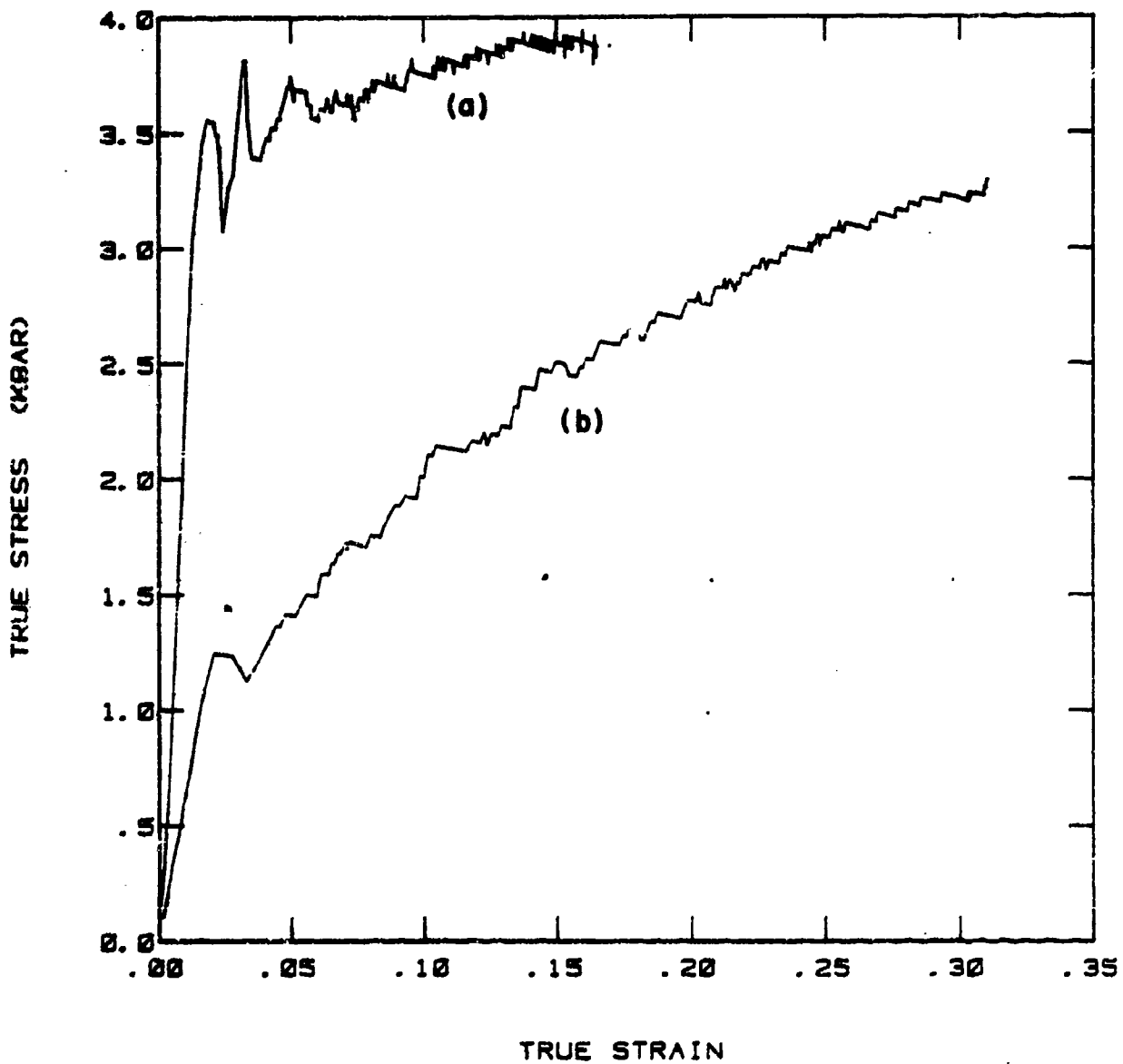


Figure 62. Stress-strain Curves for Unannealed (a) and Annealed (b) WAAM Liner Materials.

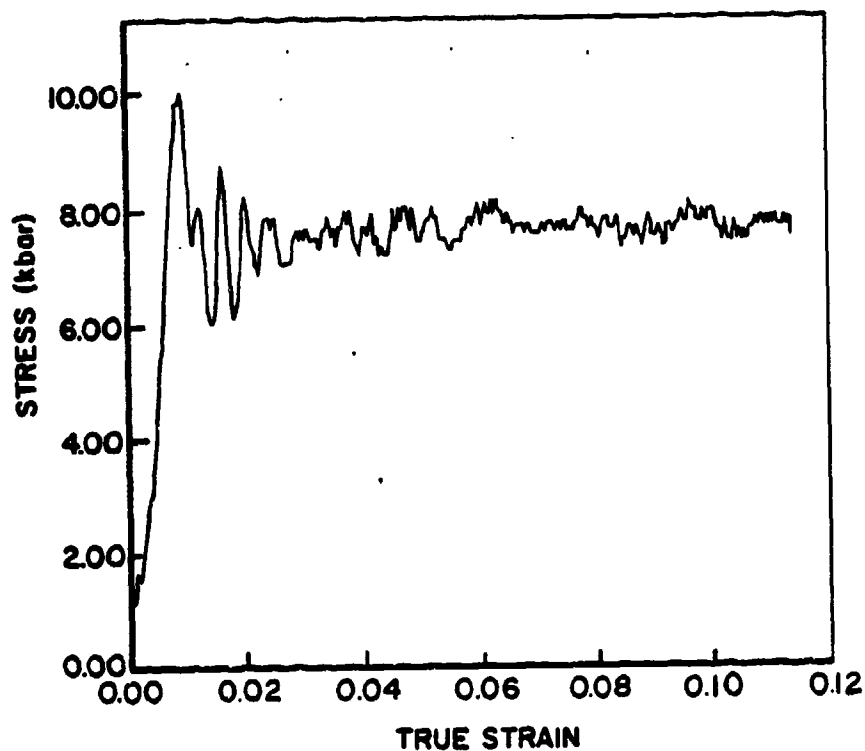


Figure 63. True Stress-True Strain Measurement for 1020 Steel Specimen.

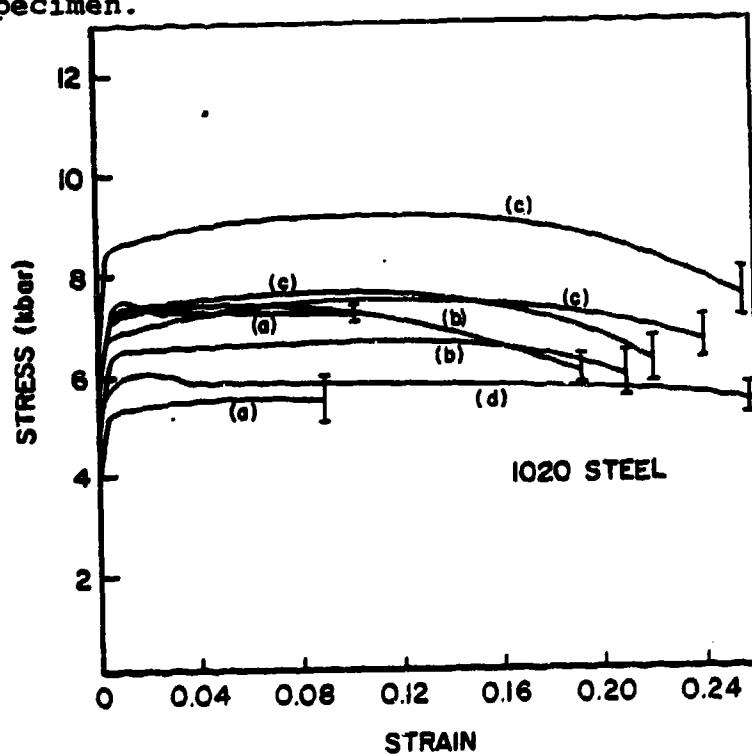


Figure 64. Smoothed Engineering Stress-Strain Behavior for 1020 Steel at Various Strain Rates. (a)  $370 < \dot{\epsilon} < 500$ ; (b)  $500 < \dot{\epsilon} < 750$ ; (c)  $750 < \dot{\epsilon} < 1000$ ; (d)  $\dot{\epsilon} > 1000$

## SECTION IV

### EXPERIMENTS WITH DYNAMICALLY EXPANDED THIN RINGS

Dynamically expanded rings have been used by several investigators to measure dynamic material properties. Most interest has focused on determination of fracture properties; see References 14, 15, 16, 17, and 18 for pioneering work. The ring development reported here has been carried out to supplement experiments with the split Hopkinson bar (SHB) (see preceding section). Interpretation of SHB data is clouded by several uncertainties: (1) the initial portion of the tensile pulse is consumed in removing slack in the grips, (2) some precompression of the specimen is unavoidable, (3) localized necking of the specimen may terminate the usefulness of the stress-strain data well before ultimate failure, and (4) calculation of strain requires assumptions about effective gauge length.

The ring experiments provide a valuable redundant technique for the SHB. In addition, the ring technique potentially features three advantages over the SHB: (1) data analysis is free from travelling wave effects and uncertain boundary conditions, (2) higher strain rates can be achieved, and (3) larger strains can be produced.

#### 1. EXPERIMENTAL TECHNIQUE

In our experiments, rings were prepared so as to fit tightly on driver cylinders. Aluminum driver cylinders were 50 mm high, and polyethylene drivers were 60 mm high. Inside cylinder diameters were 11 mm. Ring thicknesses were less than one-tenth the diameters, and ring widths and thicknesses were nearly equal. The driver cylinders contained 11 mm spherical lead azide charges of 1.6 g mass. The charges were detonated with axial bridgewires. The detonations expanded the drivers,

accelerating the rings. The driver cylinders were designed to not rupture so that the rings were launched into free expansion. The rings were decelerated by internal hoop-stresses. The constitutive parameters of the rings were computed from the equations:

$$\epsilon = \ln r/r_0 \quad (17)$$

$$\sigma_\theta = \rho r \ddot{r} \quad (18)$$

$$\dot{\epsilon} = \dot{r}/r \quad (19)$$

where  $\epsilon$  is strain,  $r_0$ ,  $r$ , and  $\ddot{r}$  are initial radius, current radius, and radial deceleration, and  $\sigma_\theta$  is the azimuthal stress. During expansion  $\sigma_z = \sigma_r = 0$ , so the stress state is analogous to a simple tensile test.

Strain rates of over  $10^4 \text{ s}^{-1}$  can be obtained with an expanding ring; high rates are achieved by reducing  $r_0$ . The maximum strain depends upon the strain energy to failure, not the duration of a loading pulse (as with the SHB). Thus, in materials of sufficiently low flow stress, extremely large plastic strains can be produced in expanding rings.

Diagnostics for the expanding ring tests consisted of a 70 mm streak camera and a VISAR. (Figure 65 shows typical results.) The flashlamp duration for the streak camera was limited to 40  $\mu\text{s}$ . The fringe constant of the VISAR was 50 m/s. The streak camera measured the motion of the ring silhouette 90 degrees away from the spot on which the VISAR was focussed. In most tests, only a portion of the  $r(t)$  curve was well defined, due to the limited flashlamp duration and loss of VISAR fringe contrast. Usually maximum velocity was read from the streak data, and deceleration from the VISAR data.

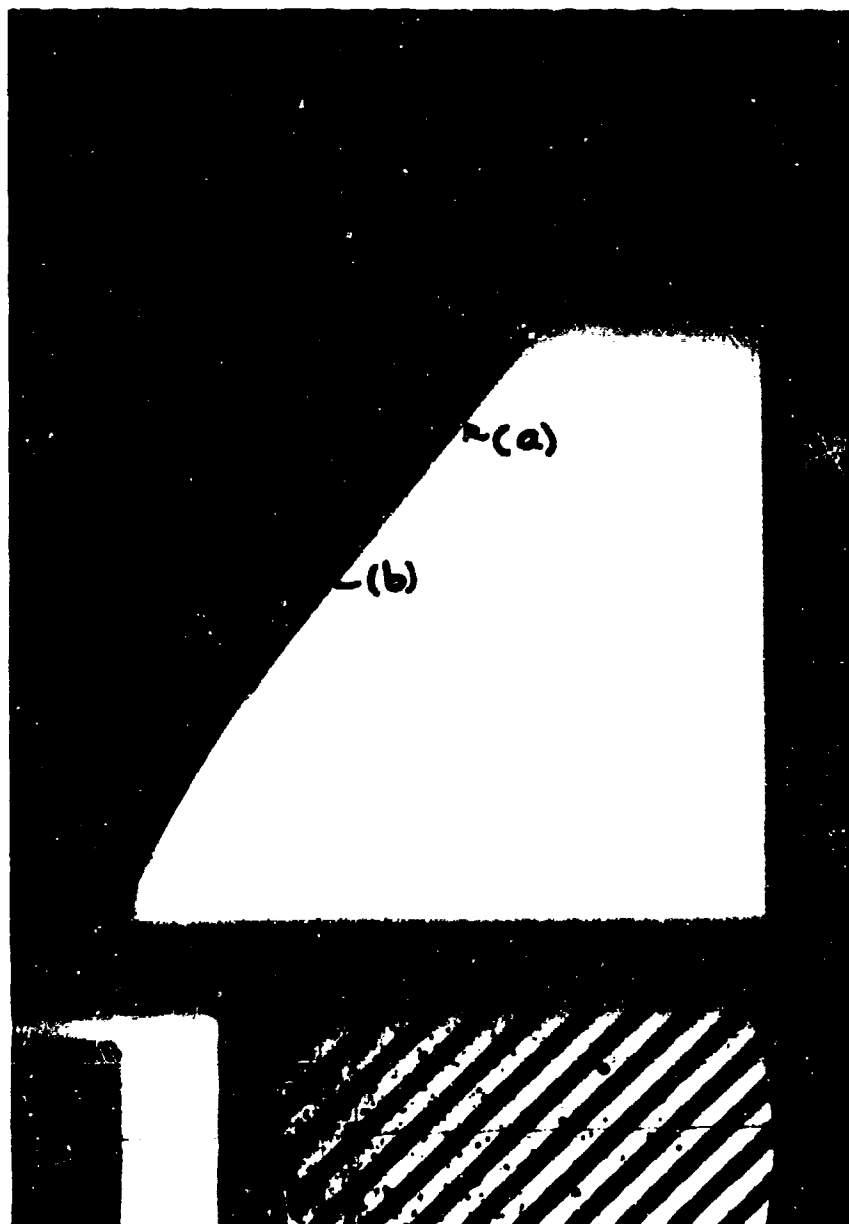


Figure 65. Sample Streak Record from Expanding Rings Launched by Polyethylene Cylinders (a) 1100 Aluminum, (b) OFHC Copper.

## 2. EXPERIMENTAL RESULTS

A large number of tests were conducted with bare driver cylinders fitted with less precise rings in order to determine the minimum size drivers that could be used without rupture. It was found that 25 mm diameter 6061-T6 aluminum drivers could launch 1.32 mm thick copper rings to 110 m/s without rupture. Annealed OFHC copper expanded to 37 percent strain from those drivers, at an average strain rate of  $4,000 \text{ s}^{-1}$ . Polyethylene drivers has to exceed 47 mm diameter to prevent rupture. Such drivers launched 1.86 mm thick copper rings at 75 m/s to obtain final strains of 12 percent, at average strain rates of  $2,000 \text{ s}^{-1}$ . Annealed 1100 aluminum rings 1.6 mm thick were launched by 43 mm diameter drivers to 135 m/s. The aluminum rings ruptured at 38 percent strain. The average value of  $\dot{\epsilon}$  was  $3,000 \text{ s}^{-1}$ .

Measurement of expansion velocity showed that any rupture of the driver cylinder invalidates the  $\sigma_a$  measurements. When polyethylene drivers of 43 mm were used to expand copper rings, rupture occurred over about 30 percent of the median section. Figure 66 compares the streak record from this test with another in which the driver did not rupture.

Six tests were conducted with aluminum drivers and five were conducted with polyethylene drivers in order to obtain data for fully annealed OFHC copper and 1100 aluminum rings. A typical velocity profile is shown in Figure 67. The uncertainty in flow stress computed from deceleration data was typically  $\pm 10$  percent.

Analysis of the acceleration phase of the ring launchers showed a definite advantage to using polyethylene driver cylinders. The acceleration stress (which corresponds to a dynamic precompression) was 5 kbar for polyethylene drivers, but three to four times higher than this for aluminum drivers. However, the value of strain at which copper rings were released



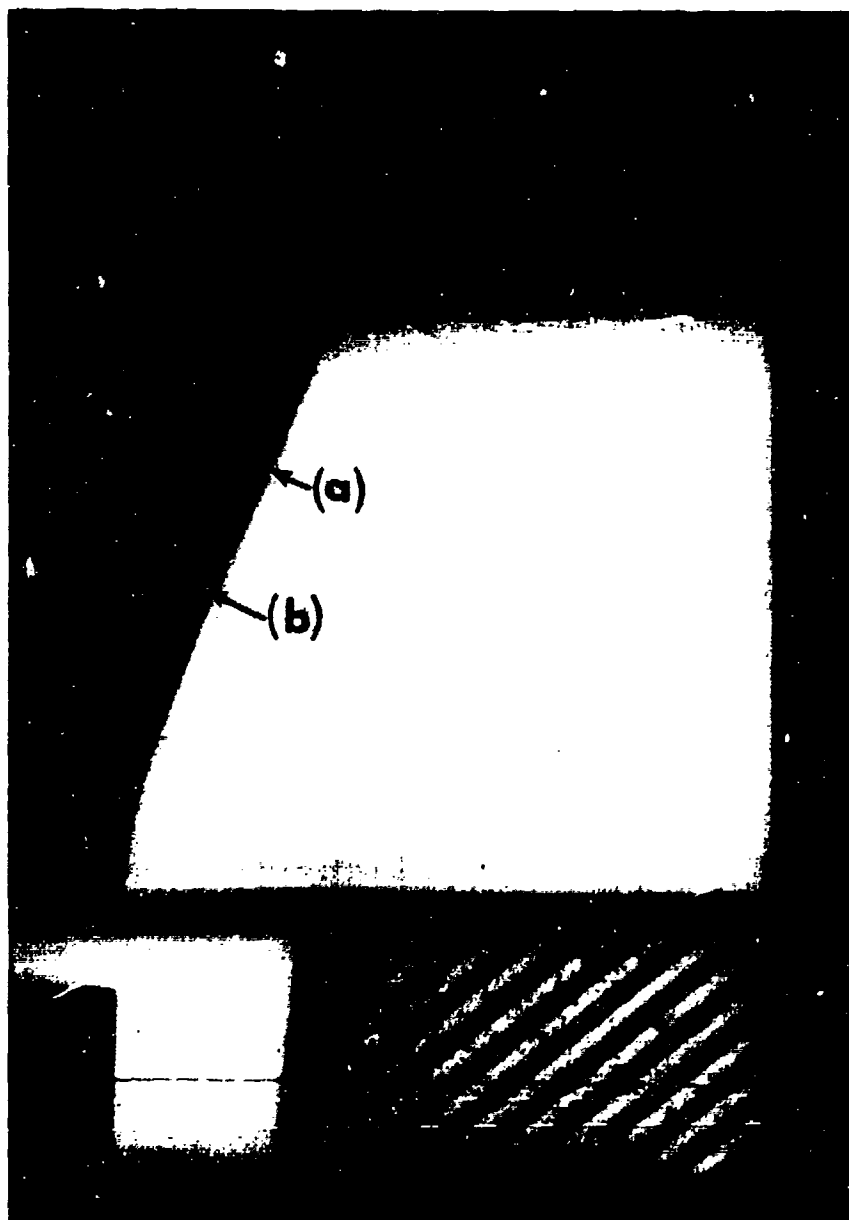


Figure 66. Effect of Rupture of Polyethylene Driver on  $R'$  Expansion (a) Driver Intact, (b) Driver Rupture.

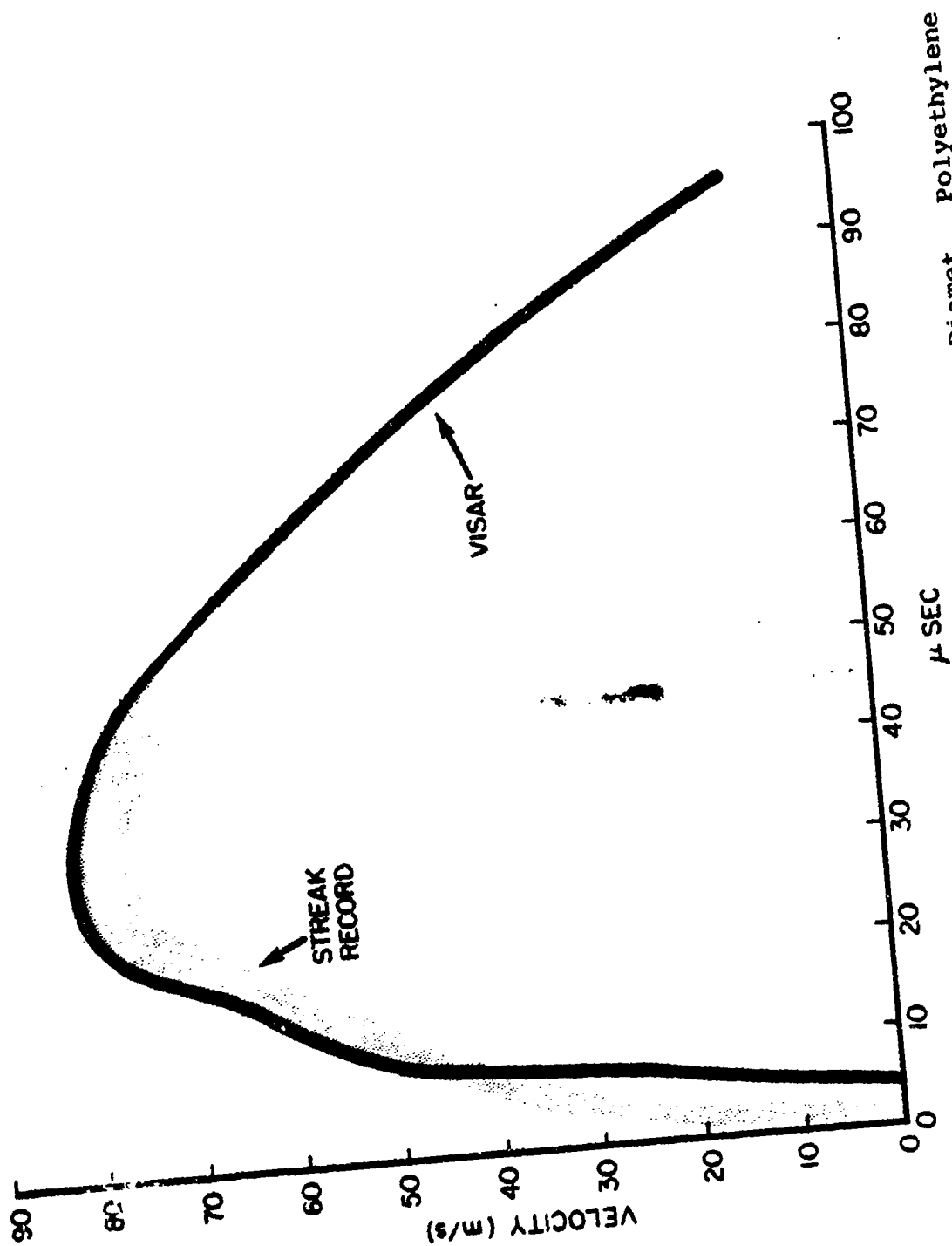


Figure 67. Velocity History for Copper Ring Launched by 47 mm Diamet polyethylene Driver Cylinder.

was greater for polyethylene drivers, ~9 percent, versus ~5 percent for aluminum drivers. The highest strain rate obtained with polyethylene drivers was only  $3,000 \text{ s}^{-1}$ , versus almost  $10,000 \text{ s}^{-1}$  for aluminum drivers.

In Figure 68, flow stress data for OFHC rings are compared with other data. The ring results derive from six tests, of which five were with aluminum driver cylinders. Hoop stresses were obtained by directly estimating  $\ddot{r}$  from  $r(t)$  curves. This was only carried out for regions of the curves that were both relatively smooth and well defined. Usually VISAR data were used, but in some cases (those with large uncertainty brackets), the streak records were also used. Dotted lines connect points read from adjacent regions of the same record. Curves 1 and 2 were obtained with split Hopkinson bar tests on the same copper as used in the rings; those samples failed during the first loading cycle, and the stress-strain curves show the influence of necking. The Hopkinson bar strain rates were  $500$  to  $800 \text{ s}^{-1}$ . Curve 3 was obtained from split Hopkinson bar tests on a different batch of OFHC copper. Curve 4 is extrapolated from high and low strain rate compression data for annealed OFHC copper.

The data displayed in Figure 68 leads to the following conclusions: (1) The flow stress for OFHC copper is very sensitive to prestrain. This accounts for the batch to batch and test to test variations. In the preceding section, imperfect SHB alignment was shown to result in some pre-strain during the compressive pulse passage, as well as during assembly. The radial acceleration phase of the ring test may also precondition the ring material. For these reasons, it is not valid to quantitatively compare initial portions of loading curves from different tests. (2) The highest (obtained at launch for relatively low strain) and lowest (obtained near arrest) strain rate data from rings contain so much scatter that they are probably unreliable. (3) Data from the mid-range of ring

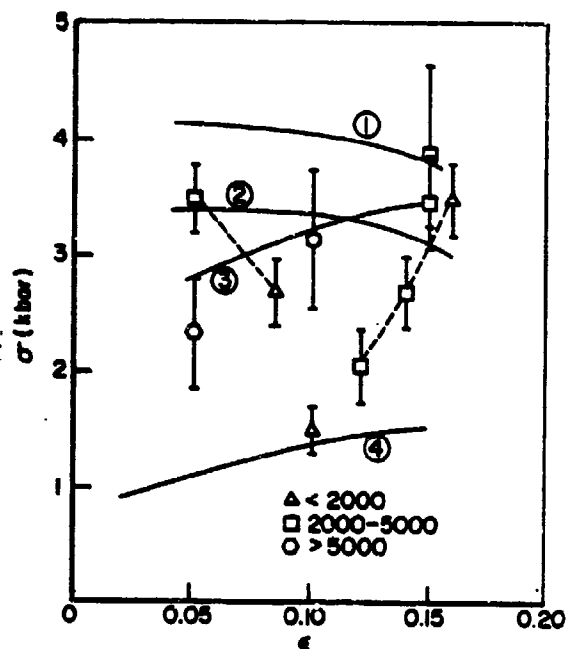


Figure 68. Yield Stress Data for Copper from Various Tests.

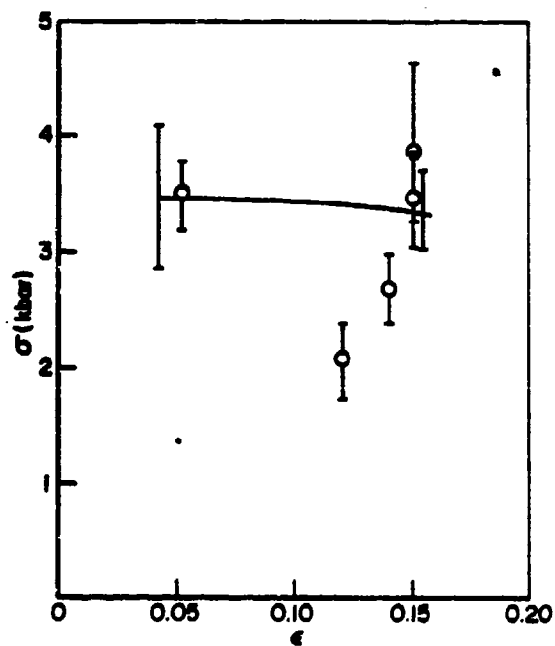


Figure 69. Comparison of Midrange Expanding Ring Data with SHB Data (shown as a line); OFHC Copper.

expansion are consistent with the Hopkinson bar results. This is shown in Figure 69. However, specimen to specimen variability is so great that many more tests would be needed before 10 percent differences in flow stress could be resolved.

Two experiments produced flow stress data for 1100 annealed aluminum. Both used polyethylene drivers. Acceleration of the rings was relatively slow; acceleration did not cease until almost 15  $\mu$ s, corresponding to a strain of almost 10 percent. However, the rings did not begin to clearly decelerate until 30  $\mu$ s, or  $\epsilon \sim 17$  percent. The delay may indicate that the aluminum rings more nearly tracked the motion of the driver cylinders than did the copper rings since the copper rings have more inertia and higher yield stress. An interval with essentially constant deceleration occurred between about 30 and 50  $\mu$ s. In one test,  $\sigma_0 = 0.05 \pm 0.06$  kbars, and in the other  $\sigma_0 = 1.11 \pm 0.11$  kbar. Strain rates and strains were similar. At  $t = 50 \mu$ s,  $\epsilon = 28$  percent strain causing the deceleration data to become erratic.

We have no explanation for the essentially constant velocity expansion in the first test. The yield stress measured from the second test also did not agree well with data from SHB tests. Those tests could only be carried to 20 percent strain without localized deformation. Flow stress was initially between 1.7 and 2.0 kbar, and work hardened slightly at 20 percent strain. At 30 percent average strain, the specimens still had not ruptured.

### 3. SUMMARY

We conclude from these experiments that the expanding ring test is a useful technique to measure yield stress and ultimate strain at high strain rates. However, the measurements are less precise than conventional techniques so that replications are necessary to support statistical treatments. The agreement between yield stress measured with rings and in split Hopkinson bar

tests is satisfactory for copper. However, for 1100 aluminum, the yield stresses measure in the ring experiments were significantly lower than measured with the Hopkinson bar.

It is recommended that tests be conducted with materials that are relatively less sensitive to prestrain. A less expensive launch technique should be developed using electrically exploded wires or bridgewire meshes. The radius of the driver cylinders should be increased so that split-Hopkinson bar strain rates can be reproduced. Hopkinson bar experiments should be conducted on precompressed materials in order to investigate the effects of radial prestrain.

## REFERENCES

1. S.J. Bless, T.C. Challita, A.M. Rajendran, "Dynamic Tensile Test Results for Several Metals," AFWAL-TR-82-4026, April 1982.
2. S.J. Bless, "Spall Criteria for Several Metals," AFWAL-TR-81-4040, June 1981.
3. T. Nicholas, "Dynamic Tensile Testing of Structural Materials Using a Split Hopkinson Bar," AFWAL-TR-80-4053, October 1980.
4. J.A. Zukas, T. Nicholas, H.F. Swift, L.G. Greszczuk, and D.R. Curran, Impact Dynamics, Wiley & Sons, pp. 277-332, 1982.
5. P.W. Bridgeman, "Studies in Large Plastic Flow and Fracture," McGraw-Hill, 1st Ed., 1952, Chapter 1.
6. H. Neuber and Z. Angew, *Mattr. Mech.*, 13, 439-442, 1933.
7. D.M. Norris, B. Moran, J.K. Scudder, and D.F. Quinones, "A Computer Simulation of the Tension Test," J. Mech. Phys. Solids, Vol. 26, pp. 1-19, 1978.
8. H.W. Hancock and A.C. MacKenzie, "On the Mechanisms of Ductile Failure in High Strength Steels Subject to . Multiaxial States of Stress," J. Mech. Phys.-Solids 14, 2/3, 107 (1976).
9. J.I. Bluhm and R.J. Morrissey, "Fracture in a Tensile Specimen," *Proceedings of the 1st International Conf. on Fracture* Vol. 3, pp. 1739-1780, (1965).
10. D.R. Curran, "Failure Due to Microcrack and Void Arrays, Overview" in "Dynamic Fracture Modeling and Quantitative Analysis," Workshop by BRL, ARRADCOM, ARO, May 17-19, 1982.
11. W.H. Chen, *Int. J. Solids Struct.* 7, 685, 1971.
12. J.W. Hutchinson and K.W. Neale, Acta Metall. 25, 839, 1977.
13. D.P. Bauer and S.J. Bless, "Strain Rate Effects on Ultimate Strain of Copper," AFML-TR-79-4021, November 1978.
14. M.J. Forrestal, B.W. Duggin, and R.I. Butler, "An Explosive Loading Technique for the Uniform Expansion of 304 Stainless Steel Rings at High Strain Rates," J. Appl. Mech., 47, 17-20, 1980.

15. R.H. Warnes, et al., "An Improved Technique for Determining Dynamic Material Properties Using the Expanding Ring," in Shock Waves and High-Strain-Rate Phenomena in Metals, ed. M.A. Meyers and L.E. Murr, Plenum Press, 1981.



# LIST OF SYMBOLS

$c_l$	longitudinal wave speed
$c_o$	bulk wave speed
$c$	wave speed
$d$	flyer plate thickness
$D$	target thickness
$t$	time
$T$	temperature
$x$	distance measured perpendicular from impact plane
$W$	flyer plate width
$u_o$	impact velocity
$v$	free surface velocity
$\epsilon$	strain
$\phi$	flyer plate tilt
$\sigma$	stress
$\sigma_o$	stress when damage first occurs
$\sigma_{eff}$	effective stress
$\sigma_{eng}$	engineering stress
$\sigma_r$	residual stress on spall plane
$\sigma_s$	spall stress (50% or greater damage)
$\sigma'_s$	apparent spall stress (equation 4)
$\sigma_T$	true stress
$\theta$	shock tilt